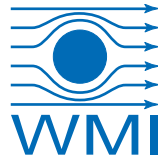




TECHNISCHE  
UNIVERSITÄT  
MÜNCHEN



WALTHER-MEISSNER-  
INSTITUT FÜR TIEF-  
TEMPERATURFORSCHUNG



BAYERISCHE  
AKADEMIE DER  
WISSENSCHAFTEN

# Inductive switchable cavity electromechanics

Master's Thesis  
Philip E. Schmidt, B.Sc.

Supervisor: Prof. Dr. Rudolf Gross  
Munich, May 2015



# Contents

<b>Abstract</b>	<b>1</b>
<b>1 Introduction</b>	<b>3</b>
<b>2 Theoretical description</b>	<b>5</b>
2.1 Mechanics of a doubly clamped nanomechanical beam . . . . .	5
2.2 Introduction to Josephson physics . . . . .	13
2.3 Flux tunable resonators . . . . .	18
2.4 Integration of a mechanically tunable SQUID into a MW CPW resonator	20
<b>3 Methods and Techniques</b>	<b>25</b>
3.1 Sample fabrication . . . . .	25
3.2 Experimental setups . . . . .	35
<b>4 Characterization of inductively coupled nano-electromechanical devices</b>	<b>43</b>
4.1 Mechanical resonators . . . . .	43
4.2 SQUIDs on silicon nitride . . . . .	51
4.3 Superconducting microwave resonators . . . . .	56
4.4 Flux tunable microwave resonators . . . . .	65
4.5 Swinging SQUIDs . . . . .	77
4.6 Coupling strengths in inductively tunable cavity optomechanics . . . . .	79
<b>5 Summary and Outlook</b>	<b>83</b>
<b>A Standard fabrication procedures</b>	<b>87</b>
A.1 Optical lithography . . . . .	87
A.2 Reactive ion etching . . . . .	88
A.3 Double layer spin coating . . . . .	88
<b>B Further experimental observations</b>	<b>89</b>
<b>Bibliography</b>	<b>93</b>

**Acknowledgment** **97**

**C Acknowledgment** **99**

# Abstract

Cavity optomechanics allows to study the light-matter interaction with micro-, meso-, and macroscopic objects offering the possibility to access the quantum mechanical regime in the literal sense [1]. Transferring this approach to the microwave domain gives rise to the field of cavity electromechanics. Typical electromechanical systems consist of a micro- or nanomechanical resonator coupled capacitively to a superconducting microwave resonator.

Here, we present the approach of an inductively coupled electromechanical system. To this end, we implement a dc-SQUID with a vibrational element at the current antinode of a  $\lambda/4$  microwave resonator. Hereby, the eigenfrequency of the microwave resonator becomes flux-tunable. As the vibration of the nano-string changes the SQUID loop area, we expect that the electromechanical coupling becomes flux-tunable. We present first experimental results and compare it with our theoretical model. These results indicate an expected tunability of the electromechanical coupling rate from 0 to 13 kHz.



# Chapter 1

## Introduction

It has been fifty years in which the exponential growth of computing complexity has proven Gordon Moore's famous prediction [2, 3]. Smart information processing has become a key technology for economic growth. Nowadays 'Big Data' is no longer only collected by intelligence agencies but also helps commercial companies improving our daily life. Insight in this field of technology can be achieved when asking: What is information? Information is physical. It may have many forms, like ink on a paper or a single electron spin. But it is linked to a physical, in particular thermodynamical property [4, 5]. Though it can be transformed from one form to another.

For example one way of converting electrical information to a mechanical one and vice versa is the so called radiation pressure of electromagnetic waves. By Newton's first law such a mechanical information can be interpreted as force, mass or acceleration.

Typically, the interaction between electromagnetic waves and matter is rather weak. To enhance this coupling, one approach is to confine the electromagnetic wave in a cavity with one of the end mirrors free to move or vibrate. Hereby, the position of the moveable end mirror in turn affects the resonance frequency of the optical cavity or in other words, if the light in the cavity pushes the mirror the resonance frequency changes and thus the light amplitude is reduced as the cavity resonance frequency becomes of resonant with the drive. This interplay between the mechanical degree of freedom (position) and the electromagnetic wave is the so-called field of optomechanics [6–8].

Additionally, optomechanics is one of the key technologies for precision metrology, by displacement sensing or sensing of minuscule forces of masses [9–11]. A review on such systems is given in Refs. [7, 9]. A mass sensitivity of  $1.3 \times 10^{-25}$  kg/Hz<sup>-1/2</sup>, equivalent to 0.40 gold atoms per Hz<sup>-1/2</sup>, has already been realized [12]. Proposals for gravitational wave detectors [13] and single molecule spectroscopy [14] have been made.

Even the quantum mechanical regime can be reached by sideband cooling to the quantum mechanical ground state [15–17]. Using this scheme, fundamental questions on quantum mechanics can be investigated, especially on large, macroscopic scale.

Focusing on superconducting MW coplanar waveguide (CPW) resonators in combination with nanomechanical objects allows to combine the field of circuit quantum electrodynamics (cQED) with nano-electromechanics, as the two fields share the same technological platform.

As the nano-mechanical elements can be produced with extremely high mechanical quality factors or long lifetimes, they are one candidate for quantum information storage. With recent developments in quantum error correction this becomes interesting for applications [18, 19]. For an efficient transfer of excitations between the mechanical, the microwave system, and the qubit, a highly tunable nano-electromechanical system is desirable. In this thesis, we investigate a hybrid system which is highly tunable in frequency and coupling rate based on a superconducting microwave resonator, superconducting interference device (SQUID), and a doubly clamped nano-mechanical beam. In contrast to capacitively coupled systems [20, 21], the inductive coupling can be tuned additionally with an externally applied magnetic field. The inductive coupling is further expected to exceed the capacitive counterpart by roughly two orders of magnitude.

The aim of this thesis was to establish a fabrication scheme for this hybrid device, investigate the device performance experimentally, and compare the theoretical estimations, e.g. for the coupling, with the experiment. Thus we start in Chapter 2 by a theoretical introduction to nanomechanical beams and Josephson physics. In addition a flux tunable microwave resonator is discussed. We combine these in a model describing an inductively coupled electromechanical hybrid system. In Chapter 3 we start with a brief explanation of the fabrication techniques used for fabricating Josephson junctions. Further the process flow for the whole hybrid device is sketched step by step. Additionally, the experimental spectroscopy setups are introduced. The fourth chapter summarizes the experimental results starting with a characterization of the nanomechanical beams at room temperature employing the optical interferometer designed and build during this thesis. Next, experiments on the dc-SQUIDs, superconducting microwave resonators and the combination of both are presented. This includes the results on the flux tunable resonators. The results are compared to the theoretical models introduced in Chapter 2. The pre-characterization was successful in determining all information necessary to estimate the vacuum coupling strength of first generation devices. The thesis ends with a short summary and outlook, where the latter highlights the coming steps to finally build such hybrid systems.

# Chapter 2

## Theoretical description

In this thesis, unconventional electromechanical couplings are investigated. In particular, we discuss the implementation of an inductive electromechanical coupling mediated using a dc-SQUID (superconducting quantum interference device) with an embedded nano-mechanical element located at the current anti-node of a microwave resonator. In this chapter, we discuss on theoretical grounds how such an electromechanical system can be realized. In this configuration the dc-SQUID acts as a tunable inductance which allows to control the resonance frequency of the microwave (MW) resonator. This can be implemented using a flux tuning of the SQUID loop. Additionally, we consider that one of the sides of the SQUID layed out in form of a nano-mechanical freely suspended element. Thus, its displacement will alter the SQUID loop area and hereby the microwave resonance frequency.

In this capter, we will consider the nanomechanical motions as well as Josephson physics, and the total effect on the MW resonator. For the theoretical description we start with the mechanical element (Sec. 2.1), turn then to the Josephson physics and derive the inductance as well as the optimal parameters of the SQUID (Sec. 2.2) and how this element affects the properties of the MW resonator (Sec. 2.3). Finally a coupling is developed (Sec. 2.4).

### 2.1 Mechanics of a doubly clamped nanomechanical beam

In the following we analyze the mechanical behavior of a nanometer sized doubly-clamped beam. To this end, we start with the vibrational properties like resonance frequency and the damping. As we implement the mechanical element in form of a double layer system (SiN / Al)<sup>1</sup>, we also consider the influence of this two layer configuration on the mechanical properties. Additionally, as the materials used for the double layer setup differ in their thermal expansion coefficients, those are taken into account to predict the resonance frequency of the system. Next a phase-delayed driven oscillator and the

---

<sup>1</sup>SiN: Silicon nitride, Si<sub>3</sub>N<sub>4</sub>, Al: Aluminum

nonlinear behavior for high drive power is discussed. In the last part we will investigate the measurement setup for any influence on the signal shape.

### 2.1.1 Doubly-clamped nanomechanical beams

The theoretical description of the vibrational properties of a doubly-clamped nanomechanical beam has been discussed in literature, see Refs. [22–24]. For a doubly-clamped nanobeam of one material, the eigenfrequency of the  $n$ -th vibrational mode  $\Omega_{m,n}$  is given by [25]:

$$\Omega_{m,n} = \frac{n\pi^2}{l^2} \sqrt{\frac{E_Y I}{\rho_0 A_B}} \sqrt{1 + \frac{\sigma_0 A_B l^2}{n^2 E_Y I \pi^2}} \approx \frac{n}{2l} \sqrt{\frac{\sigma_0}{\rho_0}} \quad (2.1)$$

the  $m$  marks that we consider a mechanical mode. For a beam of length  $l$ , cross section  $A_B$ , Young modulus  $E_Y$ , moment inertia  $I$ , and stress  $\sigma_0$ . Under high tensile stress ( $\sigma_0 A_B l^2 / (n^2 E_Y I \pi^2) \gg 1$ ), (2.1) can be well approximated with the expression on the right hand side of the equation. As we will see later in the experimental part of the thesis, we use a double layer system to experimentally realize the nanobeam. In particular we use the high tensile stress of silicon nitride and deposit a superconducting aluminium layer to create a swinging nano-beam (c.f. Fig 2.1). To account for the double layer geometry

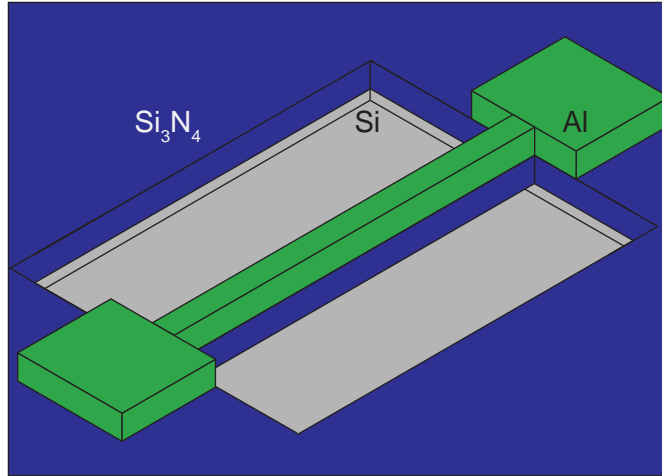


**Figure 2.1:** Schematic of a nanomechanical double layer beam, consisting of aluminum (Al) and silicon nitride (SiN) fabricated on a silicon (Si) substrate. The beam is fixed with two clamps.

with two different material systems, the typical approach is to continue the description of the system with Eq. (2.1) by introducing effective material constants  $\sigma_{\text{eff}}$  and  $\rho_{\text{eff}}$  [25, 26]. For our particular case we replace:

$$\sigma_0 \rightarrow \sigma_{\text{eff}} = \frac{t_{\text{SiN}} \sigma_{\text{SiN}} + t_{\text{Al}} \sigma_{\text{Al}}}{t_{\text{SiN}} + t_{\text{Al}}} \quad \text{and} \quad \rho_0 \rightarrow \rho_{\text{eff}} = \frac{t_{\text{SiN}} \rho_{\text{SiN}} + t_{\text{Al}} \rho_{\text{Al}}}{t_{\text{SiN}} + t_{\text{Al}}}. \quad (2.2)$$

Here, we use thicknesses  $t_i$  of the single layers  $i$  ( $i = \text{Al}, \text{SiN}$ ) as well as the respective stress  $\sigma_i$  and densities  $\rho_i$ . This treatment works particularly well for the high stress case, but can be extended by the introduction of a  $E_{Y, \text{eff}}$  to the general case. Due to the choice of our experimental configuration, we will stick to the high stress limit. So the first harmonic of our nanomechanical system is predicted as

$$\Omega_m = \frac{\pi}{l} \sqrt{\frac{\sigma_{\text{eff}}}{\rho_{\text{eff}}}}. \quad (2.3)$$

For our cryogenic experiments we have to keep in mind that the parameters in Eq. (2.3) are temperature dependent and so the frequency will be shifted between our room temperature and millikelvin temperature experiments. This is what is analyzed next.

### 2.1.2 Thermal stress

In general an object of material  $m$  changes its length  $l$  according to thermal expansion by [27]:

$$\Delta l_m = l' - l = l \alpha_m \Delta T \quad (2.4)$$

with the new length  $l'$ , the thermal expansion coefficient  $\alpha_m$  and the temperature change  $\Delta T$ . As shown in Fig. 2.1 one has to consider three materials: the silicon nitride (SiN) and aluminum (Al) in our beam as well as the silicon (Si) substrate. The silicon nitride and aluminum films share an interface and the length of the beam is determined by the position of the two clamping supports given by the substrate. Further the substrate itself contracts compensating parts of the changes being the dominant contraction. So the effectively induced tension in SiN and Al films is reduced by the silicon contraction [27]

$$\Delta \sigma_i = E_i \epsilon_i = E_i \Delta T (\alpha_i - \alpha_{\text{Si}}), \quad (2.5)$$

where  $E_i$  is the Young modulus of material  $i$  ( $i = \text{SiN}, \text{Al}$ ) and  $\epsilon_i$  is the strain induced along the beam axis. Here, we treat the two layers at first individually. As shown in Ref. [28] we can employ this approach, as the clamping positions remain the same for both layers. Then the change in total stress is given by the effective stress similar to equation (2.2), details in [28]:

$$\Delta \sigma_{\text{eff}} = \frac{t_{\text{SiN}} \Delta \sigma_{\text{SiN}} + t_{\text{Al}} \Delta \sigma_{\text{Al}}}{t_{\text{SiN}} + t_{\text{Al}}}. \quad (2.6)$$

From equation (2.3) one can see that the change of length and stress influences the beam's eigenfrequency so the new angular frequency  $\Omega'_m$  becomes:

$$\Omega'_m = \frac{\pi}{l'} \sqrt{\frac{\sigma_{\text{eff}} + \Delta \sigma_{\text{eff}}}{\rho_{\text{eff}}}} \approx \frac{\pi}{l} \sqrt{\frac{\sigma_{\text{eff}}}{\rho_{\text{eff}}}} \sqrt{1 + \frac{\Delta \sigma_{\text{eff}}}{\sigma_{\text{eff}}}} = \Omega_m \sqrt{1 + \frac{\Delta \sigma_{\text{eff}}}{\sigma_{\text{eff}}}}. \quad (2.7)$$

We further assume that the relative length change is small<sup>2</sup>. In Sec. 4.1 we will use this relation together with Eqs. (2.5) and (2.6) to estimate the low temperature resonance frequency of a nanobeam which we have characterized at room temperature.

### 2.1.3 Driven, phase-delayed harmonic oscillator with static force

For the later understanding of the dynamical response of the nano-mechanical resonator driven with an external force as well as a probe light (radiation pressure force), we consider the equation of motion of a prototypical harmonic oscillator including damping and a driving term.

We start with the effective mass of our system, which is approximately [25, 28]:

$$m_{\text{eff}} = \frac{m}{2} = \frac{\rho_{\text{eff}} l w_{\text{B}} (t_{\text{SiN}} + t_{\text{Al}})}{2} \quad (2.8)$$

The equation of motion is given by:

$$m_{\text{eff}} \frac{\partial^2 v_{\text{D}}}{\partial t^2} + m_{\text{eff}} \Gamma_{\text{m}} \frac{\partial v_{\text{D}}}{\partial t} + m_{\text{eff}} \Omega_{\text{m}}^2 v_{\text{D}} = F_0 \exp(i(\omega t + \varphi_{\text{D}})) + F_1. \quad (2.9)$$

Here  $v_{\text{D}}$  denotes the displacement of the driven beam,  $\Gamma_{\text{m}}$  the mechanical damping rate,  $\Omega_{\text{m}}/(2\pi)$  the eigenfrequency of the beam. Further  $F_0$  is the driving force with a phase  $\varphi_{\text{D}}$ ,  $F_1$  is the radiation pressure force. To solve Eq. (2.9) we use the ansatz  $v_{\text{D}} = a_0 \exp(i(\omega t + \varphi_{\text{D}})) + C_{\text{D}}$ . Thus, Eq. (2.9) becomes:

$$m_{\text{eff}} \left[ (-a_0 \omega^2 + i \Gamma_{\text{m}} a_0 \omega + \Omega_{\text{m}}^2 a_0) \exp(i\omega t) + \Omega_{\text{m}}^2 C_{\text{D}} \right] = F_0 \exp(i(\omega t + \varphi_{\text{D}})) + F_1 \quad (2.10)$$

which is valid for all times, especially for  $\omega t = 0$  and  $\omega t = \pi$  so

$$m_{\text{eff}} \left[ -a_0 \omega^2 + i \Gamma_{\text{m}} a_0 \omega + \Omega_{\text{m}}^2 a_0 + \Omega_{\text{m}}^2 C_{\text{D}} \right] = F_0 \exp(i\varphi_{\text{D}}) + F_1 \quad (2.11)$$

$$m_{\text{eff}} \left[ a_0 \omega^2 - i \Gamma_{\text{m}} a_0 \omega - \omega_0^2 a_0 + \Omega_{\text{m}}^2 C_{\text{D}} \right] = -F_0 \exp(i\varphi_{\text{D}}) + F_1 \quad (2.12)$$

Adding Eqs. (2.11) and (2.12) yields  $C_{\text{D}} = F_1/(m_{\text{eff}} \Omega_{\text{m}}^2)$ . In combination with Eq. (2.12) the complex amplitude of the oscillator becomes:

$$a_0 = \frac{F_0}{m_{\text{eff}}} \frac{\exp(i\varphi_{\text{D}})}{\Omega_{\text{m}}^2 - \omega^2 + i \Gamma_{\text{m}} \omega}. \quad (2.13)$$

Looking at the absolute amplitude of the beam's motion  $A_{\text{a}}$  the phase delay vanishes since

$$A_{\text{a}} = |a_0| \approx A_0 \left| \frac{\Gamma_{\text{m}}}{i(\Omega_{\text{m}} - \omega) + \frac{\Gamma_{\text{m}}}{2}} \right| \quad (2.14)$$

<sup>2</sup>here  $\Delta l/l \approx 10^{-3}$  in comparison to  $\Delta \sigma_{\text{eff}}/\sigma_{\text{eff}} \approx 1$  justifies this assumption.

with  $A_0 = F_0/(2m_{\text{eff}}\Gamma_m\Omega_m)$ . Plotting the imaginary part of  $a_0$  over real part forms a circle tangential to 0 with diameter  $1/(\Omega_m\Gamma_m)$ , which can be rotated around the origin by the angle  $\varphi_D$ . Nevertheless, plotting the absolute value  $A_a$  over frequency is independent of the phase  $\phi_D$ . This is expected since only the phase is shifted not having influence on the magnitude.

### 2.1.4 Nonlinear behavior of strongly driven nanobeams

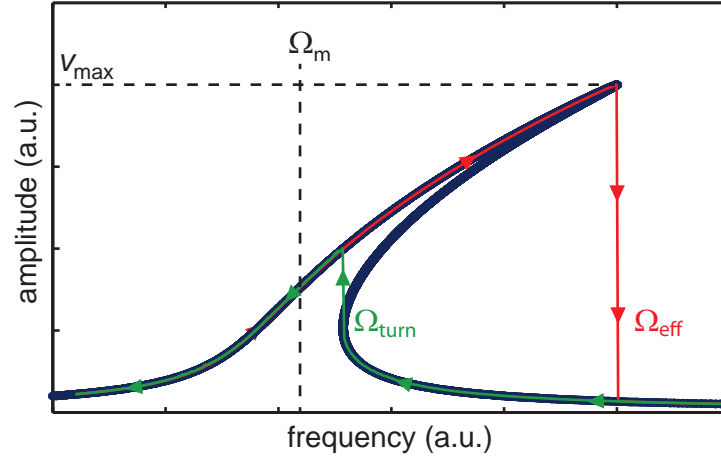


**Figure 2.2:** Nonlinear behavior of Duffing oscillator at high drive powers. In blue the solutions of Eq. (2.16). Between the frequencies  $\Omega_{\text{turn}}$  and  $\Omega_{\text{eff}}$  a bifurcation occurs with three solutions. In experiments only the two stable ones are observable depending on the sweep direction. These solutions are shown in red for up and green for downsweeps. Here the case  $\alpha > 0$  is shown, since  $\Omega_{\text{turn}}$  and  $\Omega_{\text{eff}}$  are at higher frequencies than the resonance frequency  $\Omega_m$ . In a mechanical pictures this corresponds to a stiffer spring constant for higher drive powers.

In experiments one can observe the oscillators become nonlinear, when excited by large driving forces. This behavior is described by the Duffing equation of motion adding the Duffing parameter  $\alpha$  appearing in the equation of motion in third order of the displacement [29]:

$$m_{\text{eff}} \frac{\partial^2 v_{D,n}}{\partial t^2} + m_{\text{eff}} \Gamma_m \frac{\partial v_{D,n}}{\partial t} + m_{\text{eff}} \Omega_m^2 v_{D,n} + \alpha v_{D,n}^3 = F_0 \exp(i\omega t) \quad (2.15)$$

Here, we neglect phase delays. The relation between displacement  $v_{D,n}$  and drive frequency  $\omega$  is given by [29]:

$$\left[ \Gamma_m^2 + 4 \left( \omega - \Omega_m - \frac{3}{8} \frac{\alpha v_{D,n}^2}{\Omega_m m_{\text{eff}}} \right)^2 \right] v_{D,n}^2 = \frac{F_0^2}{m_{\text{eff}}^2 \Omega_m^2}. \quad (2.16)$$

We have illustrated this behavior in Fig. 2.2 for  $\alpha > 0$  which corresponds to a stiffer spring constant. Note, that due to the nonlinearity the maximum frequency  $\Omega_{\text{eff}}$  is shifted

to higher frequencies with respect to the bare resonance frequency  $\Omega_m$ . In experiment one can only observe stable solutions as indicated with red and green lines in Fig. 2.2. In particular, depending on the drive directions one sees discrete steps in the amplitude response at  $\omega = \Omega_{\text{eff}}$  or  $\Omega_{\text{turn}}$ . Next, we want to predict those frequencies. Therefore, we solve Eq. (2.16) for  $\omega - \Omega_m$  [25]:

$$\omega - \Omega_m = \frac{3}{8} \frac{\alpha v_{D,n}}{\Omega_m m_{\text{eff}}} \pm \sqrt{\frac{F_0^2}{4m_{\text{eff}}^2 \Omega_m^2 v_{D,n}^2} - \frac{\Gamma_m}{4}} \quad (2.17)$$

Sweeping up the jump is reached at  $\Omega_{\text{eff}}$  when the square root vanishes. This gives us:

$$v_{\text{max}}^2 = \frac{8}{3} \frac{\Omega_m m_{\text{eff}}}{\alpha} (\Omega_{\text{eff}} - \Omega_m) \quad (2.18)$$

so plotting  $v_{\text{max}}$  over  $\Omega_{\text{eff}}$  allows to determine  $\alpha$ . For  $\Omega_{\text{turn}}$  we have to look for the point of vanishing slope in equation (2.17) resulting in an elliptic equation:

$$0 \stackrel{!}{=} 9m_{\text{eff}}\alpha\Omega_m\Gamma_m^2\tilde{v}^4 - 9F_0^2\alpha\tilde{v}^3 - 2F_0^2 \quad (2.19)$$

with  $\tilde{v} = v_{D,n}^2$ . Here,  $\Omega_{\text{turn}}$  depends on the nonlinearity parameter  $\alpha$  in combination with the driving force  $F_0$ . Thus, when using  $\alpha$  from Eq. (2.18) this spectral feature allows for the determination of the driving force. Further  $\alpha$  is directly related to the mechanical properties via [30]:

$$\alpha = \alpha_{\text{double}} = m_{\text{eff}}\pi^4 \frac{E_{\text{eff}} + \frac{3}{2}\sigma_{\text{eff}}}{4l^4\sigma_{\text{eff}}}. \quad (2.20)$$

This allows us to either compare the material parameters of our beam to the expected values from literature or to calibrate the amplitude spectrum if a calibration by thermal activation (see Eq. (2.1)) is not possible.

## 2.1.5 Correction of parasitic MW or optical paths via phase rotation

Due to the design of the microwave or optical setups we have to take into account parasitic paths like the direct transmission in a MW resonator or in optical experiments the reflection of the sample itself - not the beam. Those two cases are shown in figure 2.3.

In panel a) for experiments with MW resonators. We find two transmission paths which are later detected - one stemming from the feedline (black) and a second one, which is frequency dependent originating from the resonator. As we will detect always both contributions, we consider a superposition of the two transmission signals, which we model as a complex background to the Lorentzian response of the microwave resonator. Megrant *et. al.* [31] developed an elegant solution:

When plotting real and imaginary part of the linear S-parameter  $|S_{21}|^2 = P_{\text{in}}/P_{\text{out}}$ , which is proportional to the beam amplitude  $a_0$ , on a complex plot (see Fig. 2.4 a)), the

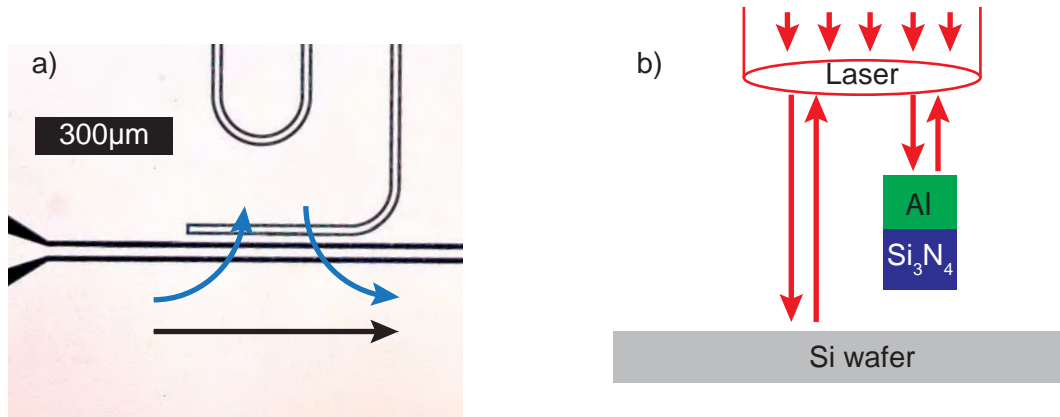


**Figure 2.3:** a) Microscope image of a superconducting MW resonator and paths of the signal. Resonator path in blue, parasitic in black. b) Schematic of parasitic optical paths in optical interferometer setups used to characterize nanomechanical beams. The parasitic effect comes from the non-vanishing spot size of the laser beam.

transmission response forms a circle, rotated by an angle  $\varphi$  which is determined by the impedance mismatch of the waveguides. By analyzing this angle, one can determine the contributions of the feedline and extract the pure resonator transmission response.

In optical reflection, see b), we also have a secondary path, independent of the drive frequency - the reflection at the substrate itself. Here the approach from Megrant *et. al.* [31] is not valid since we measure reflectivity not transmission. Here, we use a different approach:

If we look at the response of  $1 - a_0$  from Eq. (2.13) we find that the corresponding transmission and phase start changing into each other as depicted in Fig. 2.4, e.g. at a phase of  $\pi/2$  the transmission shows a dip-peak feature, while the phase appears with a Lorentzian dip. At a phase of  $\pi$  the transmission appears as Lorentzian dip and the phase as peak-dip feature and so on.

For Duffing analysis we recorded real and imaginary part in units of the input/output ratio. Then we analyze the resonance circles at low drive power for  $1 - a_0$  and determine the rotation angle. With this angle we were able to correct our data by rotating it back by  $-\phi$ . This is depicted in Fig. 2.5 a). Hereby, we cancel out the parasitic path and obtain a pure Lorentzian shape for  $\text{Arg}[a_0]$  (see Fig. 2.5 b)). As this phase is solely attributed to the geometry of the experiment it is independent of the driving force. Thus, for analyzing the nonlinear, Duffing like response, we correct the complex dataset using the phase information extracted at weak excitation force strengths. Hereby, we are able

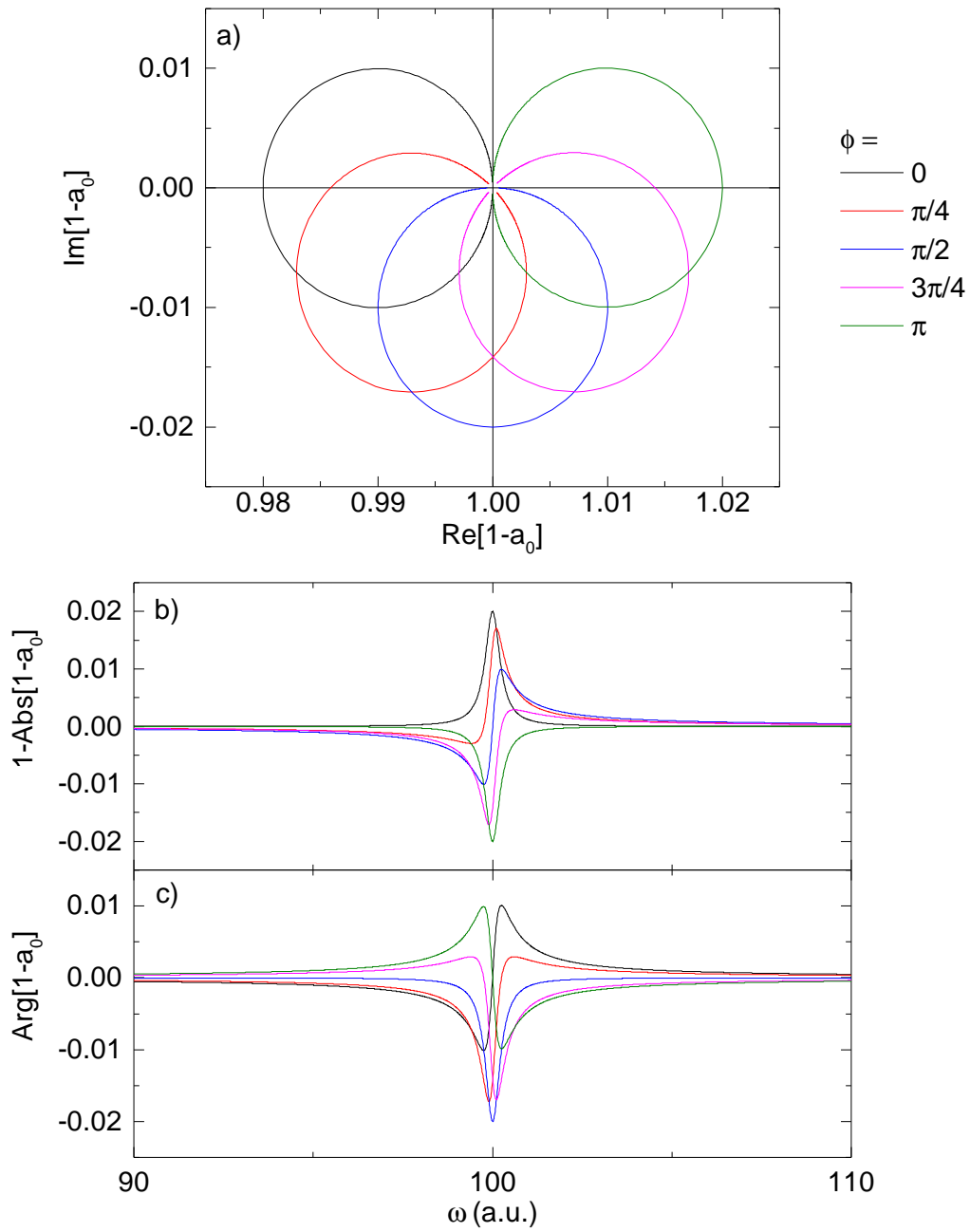


**Figure 2.4:** Peak phase (top left), peak transmission (bottom left) and peak in the complex plane (right) of a typical transmission resonance.

to reconstruct the expected sharkfin response for a Duffing oscillator.

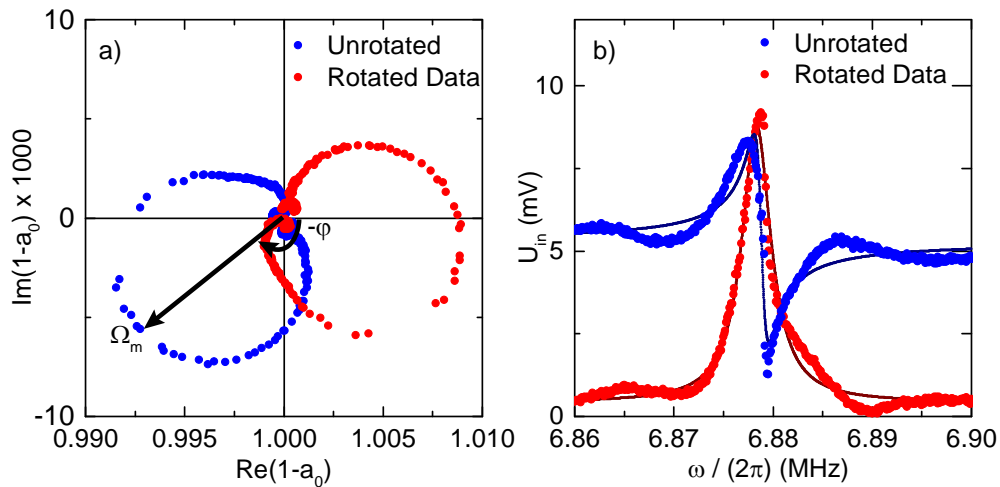


**Figure 2.5:** Unrotated (blue) and rotated (red) reflectance data of a nanomechanical beam. Panel a) shows the real and imaginary part of  $1 - a_0$ . The unrotated circle in blue is measured and by fitting the inverse of Eq. (4.9) the resonance frequency  $\Omega_m$  as well as the rotation angle  $\varphi$  is obtained as indicated by black arrows. Next the data is rotated by  $-\varphi$ , leading to a Lorentzian peak feature for the absolute value of  $a_0$ . Panel b) shows rotated and unrotated magnitude of  $a_0$  inclusive corresponding fits in dark and fine lines: Lorentzian for rotated data and Lorentzian with complex background. Looking at the graph one sees that for such high parasitic effects the model with complex background is insufficient. The fitted peak appears too narrow. In contrast the rotated data is fitted well with the pure Lorentzian model.

## 2.2 Introduction to Josephson physics

Superconductivity is best understood when we do not consider a wavefunction ( $\Psi$ ) constructed from all electrons in the solid but treat the system as macroscopic quantum mechanical wavefunction  $\Psi_s = \sqrt{n_s} \cdot \exp(i\varphi_s)$  [32]. In the following we want to introduce briefly the basics of Josephson physics, i.e. that describes the situation of two superconducting areas weakly coupled by an insulating layer. A more detailed treatment is found in [33]. In this section, we will focus on the main results and stick to this notation so consulting the reference is simplified. Additionally, we note that Cooper pair properties are labeled with a star and that we label the macroscopic wave function with the index  $s$ .

### 2.2.1 A single Josephson junction

Let us consider a quantum mechanical barrier as insulating Josephson junction with thickness  $d$  and step height  $V_0$  as depicted in Fig. 2.6. Furthermore the size is small

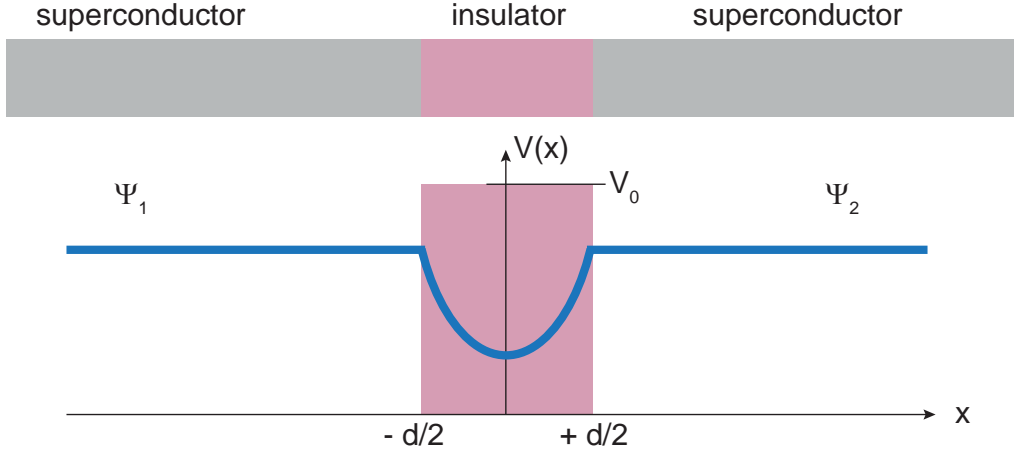


**Figure 2.6:** Schematic overview of a single Josephson Junction. Grey shows the superconducting regime while the insulator is shown in purple. Below the macroscopic wavefunctions  $\Psi_{1,2}$  are plotted in blue. In the superconducting area they are constant, while in the insulator they drop down exponentially.

enough so the Josephson current density stays constant. In addition, we will only consider elastic processes. Under those assumptions we obtain a time independent case, described by the stationary Schrödinger equation:

$$-\frac{\hbar^2}{2m^*}\nabla^2\Psi_s = (E - V_0)\Psi_s. \quad (2.21)$$

Here,  $m^*$  corresponds to the Cooper pair mass. Equation 2.21 has to be solved for all regions and the wavefunction has to be continuously matched at the boundaries  $x = \pm d/2$ . As the super-current density is given by  $\mathbf{J}_s = q^*/m^* \cdot \text{Re}\{\bar{\Psi}_s(-i\hbar\nabla)\Psi_s\}$ , where  $q^*$  stands for the charge of a Cooper pair, it can be derived that:

$$\mathbf{J}_s = I_c \sin(\theta_2 - \theta_1) \quad (2.22)$$

with the wavefunctions  $\Psi_{1,2} = \sqrt{n_{A,B}} \exp(i\theta_{1,2})$  on each side of the barrier. Here  $n_{A,B}$  describes the density of Cooper pairs at each side of the junction and  $\theta_{1,2}$  the superconducting phase. Furthermore, we define the critical current of the Josephson junction:

$$I_c = -\frac{q^*\hbar\kappa}{m^*} \frac{\sqrt{n_A n_B}}{\sinh(2\kappa d)}, \quad (2.23)$$

with the characteristic decay constant  $\kappa = \sqrt{2m^*(V_0 - E)}/\hbar$ . Bringing Eq. (2.22) onto a macroscopic level one has to transform the Cooper pair parameters:  $q^* \rightarrow 2e$ ;  $m^* \rightarrow 2m_e$ ;  $n_{A,B} \rightarrow n_e/2$  with the specific parameters of a single electron. Furthermore, we

introduce the gauge invariant phase difference  $\varphi$  via [33]:

$$\varphi = \theta_2 - \theta_1 - \frac{2\pi}{\Phi_0} \int_1^2 \mathbf{A} d\mathbf{l}. \quad (2.24)$$

This results in the so called first Josephson equation describing the current flow across the junction:

$$I = I_c \sin \varphi. \quad (2.25)$$

The second Josephson equation is obtained by investigating the time derivative of Eq. (2.24) and the superconducting energy-phase relation [33]:

$$\hbar \frac{\partial \theta}{\partial t} = \frac{1}{2n^*} \Lambda \mathbf{J}_s^2 + q^* \phi \quad (2.26)$$

where  $\Lambda = m^*/(n_s^* q^{*2})$  is the London coefficient and  $\phi$  the electric potential. Assuming a continuous superconducting current density leads to the second Josephson equation:

$$\frac{\partial \varphi}{\partial t} = \frac{2\pi}{\Phi_0} V \quad (2.27)$$

From the two Josephson equations we can derive the Josephson inductance  $L_J$ , capacity and energy of the junction [33]:

$$\frac{dI}{dt} = I_c \cos(\varphi) \frac{2\pi}{\Phi_0} V \rightarrow L_J = \frac{\Phi_0}{2\pi I_c \cos(\varphi)}. \quad (2.28)$$

Additionally, a Josephson junction consists of two metal plates separated by an insulator forming a capacitor with capacitance:

$$C = \frac{e^2}{2E_C} \quad (2.29)$$

with the charging energy of the junction  $E_C$ . The energy stored in the system  $\tilde{E}$  is given by

$$\tilde{E} = \int_0^t IV dt = \frac{\Phi_0}{2\pi} I_c \int_0^\varphi \sin(\tilde{\varphi}) d\tilde{\varphi} = E_{J,0} (1 - \cos(\varphi)) \quad (2.30)$$

with  $E_{J,0} = \Phi_0 I_c / (2\pi)$ . A thermodynamic analysis of the Gibbs energy [33] shows that the potential energy is given by:

$$E_{\text{pot}} = E_{J,0} \left[ 1 - \cos(\varphi) - \frac{I}{I_c} \varphi \right] + \tilde{c} \quad (2.31)$$

where formally potential energy contains an offset  $\tilde{c}$ , which won't be of significance for the further discussion as only energy differences will play a role. The shape of Eq. (2.31) is similar to a tilted washboard which gives it this name as shown in Fig. 2.7 b). To

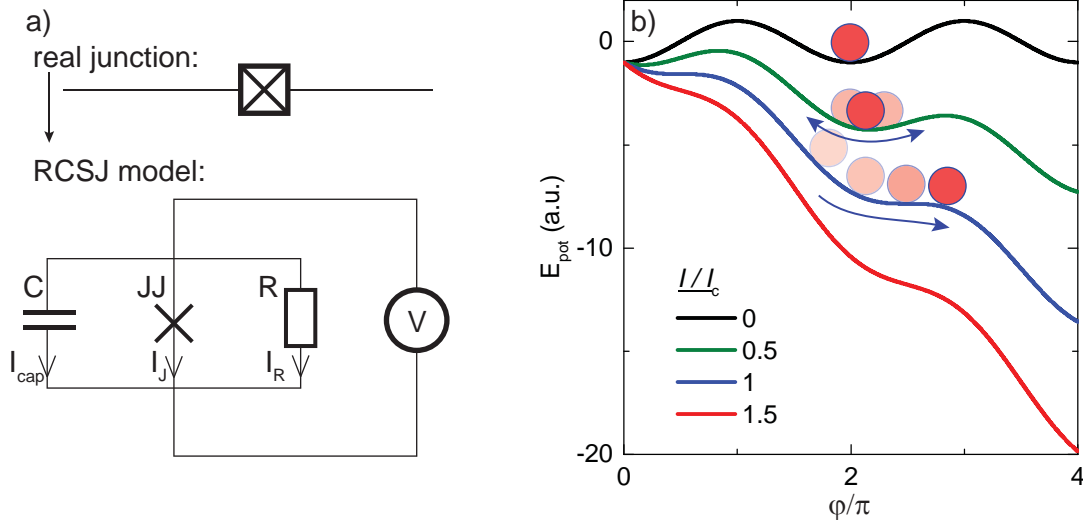


**Figure 2.7:** a) RCSJ model b) Potential energy of a Josephson Junction due to Eq. (2.31). The superconducting phase can be seen as a particle with mass in this potential as indicated. Depending on the damping hysteretic behavior can be observed.

discuss the behavior of the phase difference in such a potential, we image it as a particle with certain mass and damping. This image shows that it is trapped for vanishing applied currents. By increasing the current the washboard potential becomes tilted. When the current exceeds  $I_c$  the barrier confining the motion of the particle is effectively removed and the phase particle starts effectively moving in a continuous fashion resulting in a voltage drop (2. Josephson equation). Since the phase difference obeys quantum mechanic laws, tunneling can appear if the bias current is close to the critical current [33]. Decreasing the current allows to recapture the particle in a well of the washboard potential. Note, that there can be a hysteresis in this process since it depends on the damping whether the phase is trapped right at  $I_c$  or if its remaining kinetic energy can overcome the potential barriers. This damping is described by the Steward McCumber parameter

$$\beta_c = Q^2 = \frac{2e}{\hbar} I_c R_n^2 C \quad (2.32)$$

which is the square of the quality factor  $Q = RC/\sqrt{LC}$  of the effective LC circuit modeling the Josephson junction. As we have already seen, such a junction has a specific inductance, a capacity and if the current exceeds the critical current a normal resistivity. If we further add a noise source, we end up with the so-called resistively and capacitively shunted junction model (RCSJ), where a Josephson Junction is described by a parallel circuit of those four elements, see figure 2.7 a). Using this simple model one is able to interpret a hugh variety of phenomenona by SIS junctions. In the following, we want to analyze two

junctions connected to a superconducting loop, the so called dc-SQUID.

## 2.2.2 Superconducting Quantum Interference Devices

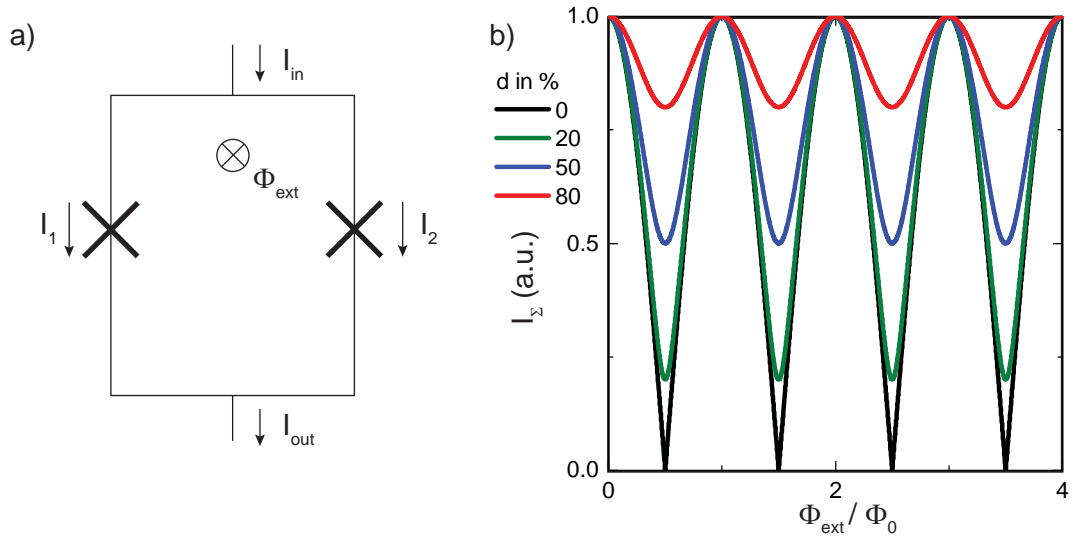


**Figure 2.8:** a) Electric scheme of a dc-SQUID b) Maximum supercurrent for SQUIDs with asymmetric junctions, described by an asymmetric factor  $d$ . Current function was modeled by Eq. (2.36) in a SQUID over  $\Phi_{\text{ext}}/\Phi_0$  for selected  $d$  values.

Next, we consider an electrical circuit with two Josephson junctions operated in a parallel configuration. The geometry of the circuit shall be in a loop fashion as depicted in Fig. 2.8 a). This circuit design is called a dc-SQUID. Initially, we will assume that both junctions have the same critical current  $I_c$ . Via Kirchhoff's law we find for the total current:

$$I_s = I_c \sin \varphi_1 + I_c \sin \varphi_2 = 2I_c \cos \left( \frac{\varphi_1 - \varphi_2}{2} \right) \sin \left( \frac{\varphi_1 + \varphi_2}{2} \right) \quad (2.33)$$

with the phase drop  $\varphi_{1,2}$  over junction 1 resp. 2. To obtain the gauge invariant phase difference one has to integrate the phase along the superconducting ring and finds [33]

$$\varphi_2 - \varphi_1 = \frac{2\pi\Phi}{\Phi_0}. \quad (2.34)$$

If we assume in a simple model, that the flux threading the loop is equal to the external applied flux, so  $\Phi = \Phi_{\text{ext}}$ , then the combination of Eqs. (2.33) and (2.34) results in the maximal supercurrent

$$I_s^m = 2I_c \left| \cos \left( \pi \frac{\Phi_{\text{ext}}}{\Phi_0} \right) \right| \quad (2.35)$$

In reality the junctions of a SQUID may differ slightly in their critical currents. This effect changes the minimal critical current. This decreases the slope of  $I(\Phi)$ . The behavior of two non-identical junctions is described by adding a correction term to Eq. (2.35):

$$I_{s,\text{eff}}^m = I_{c,\Sigma} \left| \cos \left( \pi \frac{\Phi_{\text{ext}}}{\Phi_0} \right) \right| \sqrt{1 + d^2 \tan^2 \left( \pi \frac{\Phi_{\text{ext}}}{\Phi_0} \right)} \quad (2.36)$$

where  $I_{c,\Sigma} = I_{c,1} + I_{c,2}$  and  $d = (I_{c,1} - I_{c,2})/I_{c,\Sigma}$ . So  $d$  can be seen as a ratio of the junction asymmetry. The influence of this factor is depicted in Fig. 2.8 b). Here, we observe that the maximum critical current is reached for all values of  $d$ , but the modulation depth is reduced when  $d$  is increased. Further theoretical descriptions concerning self induction effects or asymmetric loop designs can be found in e.g. in Ref. [34]. We note, that the dc-SQUIDs used in this thesis are designed to have a minimal self inductance and thus corrections due to self inductance will be neglected throughout this thesis.

To obtain the Josephson inductance  $L_J$  one has to substitute the supercurrent in the SQUID from Eq. (2.35) in Eq. (2.28) and gets [33]:

$$L_J = \frac{\Phi_0}{2\pi I_{\Sigma} \left| \cos \left( \pi \frac{\Phi_{\text{ext}}}{\Phi_0} \right) \right|}. \quad (2.37)$$

As we can see this inductance is periodical in  $\Phi_{\text{ext}}/\Phi_0$  and becomes infinitely large in the case  $\Phi_{\text{ext}} \rightarrow \Phi_0$ .

## 2.3 Flux tunable resonators

In general the eigenfrequency of an electrical resonant circuit is

$$\omega_0 = \frac{1}{\sqrt{L_R C_R}} \quad (2.38)$$

with the standard inductance  $L_R$  and capacity  $C_R$  of the circuit. We have further seen that the inductance of a SQUID is flux tunable. So adding it as an additional inductance to a resonant circuit, as shown in Fig. 2.9 a), the inductance of the circuit transforms like  $L \rightarrow L_R + 2L_J(\Phi_{\text{ext}})$ . The factor 2 in front of the Josephson inductance corrects that the SQUID is placed at the current anti-node hence it has a higher impact to the total inductance. So the resonance frequency becomes:

$$\omega_0(\Phi_{\text{ext}}) = \frac{\omega_R}{\sqrt{1 + 2 \frac{L_J(\Phi_{\text{ext}})}{L_R}}} \quad \text{with } \omega_R = \frac{1}{\sqrt{L_R C_R}}. \quad (2.39)$$

As we have seen in the previous chapter the Josephson inductance can become infinitely large for respective flux ratios. This will increase the denominator and so tunes the

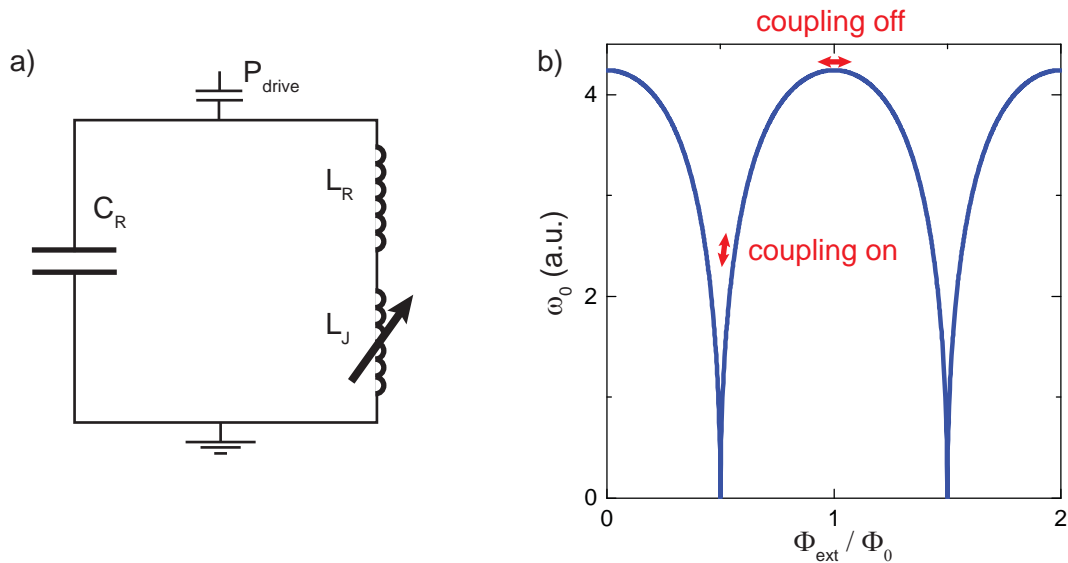


**Figure 2.9:** a) Electric scheme of a MW resonator with SQUID at the current anti-node. In addition to the regular capacity and inductance the SQUID adds a tunable inductance the Josephson inductance to the resonance circuit. b) Resonance frequency  $\Omega_m$  of a flux tunable resonator over  $\Phi_{\text{ext}}/\Phi_0$  due to Eq. (2.39). The resonance is periodically tuning down when the Josephson inductance is becoming infinity. In red we have depicted the idea of a inductive coupled optomechanical system: the MW resonators frequency is depending on the flux, which is the product of applied magnetic field and area of the SQUID loop. Having released one arm of the SQUID it can change the area and so the flux. When this is done at the highest frequency where the slope is vanishing the MW resonance is not changing. Hence the coupling is switched off. Though when done at a high slope the resonance is changing and so an inductive switchable coupling is realized.

frequency to lower values. For a quantitative analysis we insert Eq. (2.37) into (2.39). We have plotted this in Fig. 2.9 b) where we see indeed that the resonance frequency has an upper limit and then decreases to zero for an increasing Josephson inductance.

We obtain a first impression on inductive coupling looking at the MW resonance characteristic. It depends on the flux ratio which is the product of applied magnetic field and the area of the SQUID loop. For an electro-mechanical interaction, we consider that one arm of this SQUID loop is freely suspended and free to move. Hereby, the loop area depends on the displacement of the arm from its resting position and in turn the flux through the loop is modified (depicted in Fig. 2.10 b)). As the flux change caused by the motion is small compared to the total flux threading the loop, we can naively assume a linearized picture. Thus we expect that the frequency change in the microwave resonator will crucially depend on the flux bias. In particular, we will find regimes with a large transfer ratio as well as negligible frequency responses by the microwave resonator as indicated by the red arrows in Fig. 2.9 b). At the top frequency with vanishing slope of

the curve we have no change in the MW frequency, so the coupling is switched off. In contrast at high slope the MW frequency indeed is influenced by the mechanical beam. As we see from this gedankenexperiment the inductive coupling depends on the slope of the MW frequency, in other words no slope, no coupling, high slope high coupling. The slope is given by:

$$\frac{\partial\omega}{\partial\Phi} = \frac{\omega_R}{L_R \sqrt{1 + 2\frac{L_J(\Phi)}{L_R}}} \frac{\partial L_J(\Phi)}{\partial\Phi} \quad (2.40)$$

with the flux derivative of the Josephson inductance:

$$\frac{\partial L_J}{\partial\Phi} = \frac{\Phi_0}{2\pi I_\Sigma} \tan\left(\pi \frac{\Phi}{\Phi_0}\right) \sec\left(\pi \frac{\Phi}{\Phi_0}\right). \quad (2.41)$$

An interesting point arises when adding the Josephson inductance, since it is nonlinear as a series expansion in the range from  $-\pi/2 < \varphi < \pi/2$  shows [35]:

$$L_J = \frac{\Phi_0}{2\pi I_c \cos(\varphi)} = \frac{\Phi_0}{2\pi I_c} \left(1 + \frac{\varphi^2}{2!} + \frac{5\varphi^4}{4!} + \dots\right) \quad (2.42)$$

or current biased [35]:

$$L_J = \frac{\Phi_0}{2\pi I_c} \left(1 - \frac{I^2}{I_c^2}\right)^{-1/2} = \frac{\Phi_0}{2\pi I_c} \left(1 + \frac{I^2}{2I_c^2} + \frac{3I^4}{8I_c^4} + \dots\right) \quad (2.43)$$

The behavior of nonlinear oscillators has been studied for mechanical resonators in Sec. 2.1.4 via adding a Duffing term (third order perturbation) to the equation of motion. An analogue approach can be done here. The Lagrangian of such a SQUID-MW resonator system is derived in [36]. Starting from this Lagrangian applying the Euler-Lagrange-formalism the equation of motion is obtained. The nonlinearity is treated as perturbation and so a Duffing equation can be obtained.

Finally we can plug all together and calculate the coupling in our hybrid system in the next section.

## 2.4 Integration of a mechanically tunable SQUID into a MW CPW resonator

In the following, we consider an experimentally feasible realization of an electro-mechanical device based on a flux tunable resonator containing a dc-SQUID, where the latter includes an nano-mechanical element realizing the inductive coupling. To this end, Fig. 2.10 a) shows a  $\lambda/4$  coplanar microwave resonator which is terminated at one end with a geometric capacitance and shorted on the other end to ground using a dc-SQUID. Again,

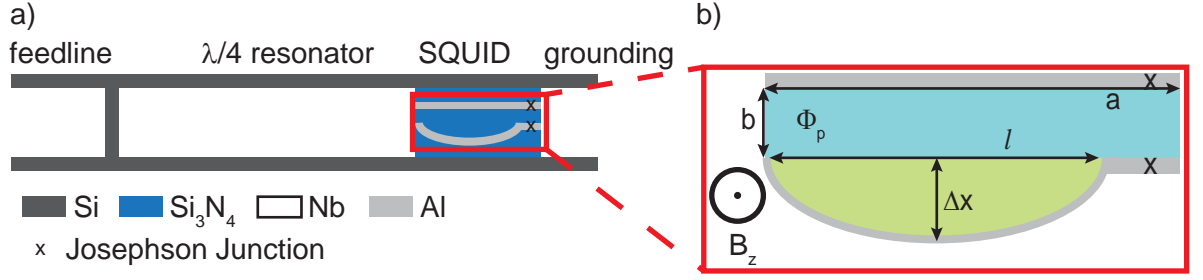


**Figure 2.10:** a) Overview scheme of a CPW MW resonator inductive coupled via SQUID to a nanomechanical oscillator. b) Details on the SQUID with total length  $a$  and width  $b$ . The applied magnetic field  $B_z$  causes a flux  $\Phi_p = abB_z$  (blue), the tunable flux (green) comes from the beam motion  $\Delta x$  and length of the beam  $l$ . Both drawings not to scale.

this SQUID shall contain a nanobeam, modulating the flux through the SQUID loop and thus the microwave resonator frequency.

In detail, at the SQUID (see Fig. 2.10 b)) when applying a magnetic induction  $B_z$  perpendicular to the loop the total flux is split in two parts, a part independent of the beam's motion ( $\Phi_p$ , turquoise) and the area modulated by the beam (bright green). One is set by the area given by length  $a$  and width  $b$  of the SQUID, the penetrating flux  $\Phi_p = abB_z$  (blue); The other one, the tunable flux, caused by the in-plane displacement of the nanomechanical beam  $\Delta x$  and its length  $l$ . In total,

$$\Phi = abB_z + l\Delta x B_z = \Phi_p + l\Delta x B_z. \quad (2.44)$$

To derive the coupling, we introduce the Hamiltonian of the system [37]:

$$H = \hbar\omega_0(\Phi) \left( a^\dagger a + \frac{1}{2} \right) + \hbar\Omega_m \left( b^\dagger b + \frac{1}{2} \right). \quad (2.45)$$

The first term on the right hand side describes the microwave resonator including the flux dependent eigenfrequency. The second term describes the nanomechanical oscillator. We further introduce the quantum mechanical annihilation (creation) operators of the microwave and mechanical resonator  $a(a^\dagger)$  resp.  $b(b^\dagger)$ . Note that for the mechanical resonance a capital  $\Omega_m$  is used for clarity.

The flux tunable MW resonance frequency is given by Eq. (2.39). Since the displacement  $\Delta x$  causes small flux changes compared to  $\Phi_p$  (Eq. (2.44)) the MW resonance frequency

is expanded in a Taylor series to first order [38]:

$$\begin{aligned}\omega(\Phi) &\approx \omega(\Phi)|_{\Phi=\Phi_p} + \left. \frac{\partial\omega}{\partial\Phi} \right|_{\Phi=\Phi_p} \left. \frac{\partial\Phi}{\partial\Delta x} \right|_{\Delta x=0} \Delta x \\ &= \omega(\Phi_p) + \frac{\partial\omega(\Phi_p)}{\partial\Phi} \cdot lB_z x_{zpf}(b^\dagger + b)\end{aligned}\quad (2.46)$$

Here the zero point fluctuation of the nanomechanical beam was introduced:

$$x_{zpf} = \sqrt{\frac{\hbar}{2m_{\text{eff}}\Omega_m}}. \quad (2.47)$$

We thus can rewrite the Hamiltonian of the hybrid system in the form:

$$H = \hbar\omega_0(\Phi_p) \left( a^\dagger a + \frac{1}{2} \right) + \hbar\Omega_m \left( b^\dagger b + \frac{1}{2} \right) + g_0 \left( a^\dagger a + \frac{1}{2} \right) (b^\dagger + b) \quad (2.48)$$

with the vacuum coupling strength:

$$g_0 = \frac{\partial\omega_0(\Phi_p)}{\partial\Phi} l x_{zpf} B_z = \frac{\omega_R l x_{zpf} B_z}{L_R \sqrt{1 + \Phi_0/\pi L_R I_\Sigma \cos\left(\pi \frac{\Phi_p}{\Phi_0}\right)}} \frac{\Phi_0}{2\pi I_\Sigma} \tan\left(\pi \frac{\Phi_p}{\Phi_0}\right) \sec\left(\pi \frac{\Phi_p}{\Phi_0}\right) \quad (2.49)$$

where the right side is valid for an externally applied flux  $\Phi$  in the range of  $\pm 1/2\Phi_0$  only. Further analysis shows that higher order coupling are negligible, so we already have a well description of the system.

Figure 2.9 b) already introduced idea of inductive coupling and we have already noted that the slope of the MW resonator can be tuned. From Eq. (2.49) we see that the coupling becomes zero at a flux bias of  $\Phi = n/(2\Phi_0)$  and (theoretically) maximal for  $\Phi = n\Phi_0$ . Long beams, high magnetic fields and zero point fluctuations will further increase the coupling. This observation leads to summarize the competing design criteria envisaged for the device:

- Nanomechanical beam: In the mechanical oscillator the length and zero point fluctuation has to be large. Recent experiments with MW resonators capacitively coupled MW resonators to doubly clamped nanobeams reported  $l = 60 \mu\text{m}$  and  $x_{zpf} = 30 \text{ fm}$  [39]. The beam's length can be increased but this decreases the resonance frequency of the beam  $\Omega_m$ . For the intended experiments we also aim for the resolved sideband regime, that is:

$$\Omega_m > \Gamma. \quad (2.50)$$

Where  $\Gamma$  denotes the linewidth of the MW resonator. So,  $\Omega_m(l)$  and  $\Gamma$  have to be

investigated so best results can be achieved.

- Flux tunable resonator: For large coupling a high resonance frequency is desirable. On the other side the cold amplifiers in the cryostat are limited by microwave frequencies of 8 GHz. Above we will not be able to follow the resonator curve which sets an upper limit.

The SQUIDs have to be long for high coupling as mentioned before. This leads to a high sensitivity to magnetic field noise. To decrease the noise sensitivity, the squid loop area should be minimized. Thus, the loop has to be narrow, width of  $2\ \mu\text{m}$  seam feasible with current lithography techniques. Furthermore, the SQUID shall be designed symmetrical to avoid influences from induced currents and obtain a full frequency modulation depth ( $d = 0$ ).

Since the SQUID sits at the current anti-node, high currents cross the Josephson junctions. So large  $I_c$  are required to be able to sustain a high number of photons in the resonator. Otherwise the superconductivity would break down or to avoid this the applied magnetic field has to be lowered leading to a decreased coupling strength.

- Magnetic field: For fabricating the SQUIDs aluminum is shadow evaporated. The critical field of it will set the limit for highest applied magnetic fields. Aluminum has a critical field of about 10 mT in bulk. Thin films, internal stress, impurities or local field enhancement due to shape factors lead to even lower fields [37]. To get an insight this has to be measured in experiments at mK temperatures.

Additional the magnetic field will be applied by a superconducting coil and a current source. The SQUID has a size of about  $65 \times 2\ \mu\text{m}^2 = 130\ \mu\text{m}^2$  so one flux quantum corresponds to  $15\ \mu\text{T}$ . Since a stable in control in the  $m\Phi_0$  range is desirable this means the shielding and current source have to be sufficient to guarantee for about  $10^{-8}\ \text{T}$  stability, while about  $10^{-3}\ \text{T}$  are applied.

This experimental requirements are demanding, but have been established individually before. The challenge is to combine all of them together.

For a first approximation on possible coupling strength we calculate with the following parameter:  $l = 60\ \mu\text{m}$ ;  $x_{\text{zpf}} = 20\ \text{fm}$ ;  $B_z = 1\ \text{mT}$ ;  $I_c = 1\ \mu\text{A}$ ;  $\omega_R/(2\pi) = 7\ \text{GHz}$ ;  $Z_0 = 50\ \Omega$ . The MW resonators impedance  $Z_0$  is used to calculate the inductance:

$$L_R = \frac{Z_0}{\omega_R} = 1.14\ \text{nH} \quad (2.51)$$

To calculate the final coupling strength the last remaining unknown parameter is the slope of MW resonator. It is determined by the design parameters mentioned above and calculated via Eqs. (2.40) and (2.41) at the penetrating flux ratio  $\Phi_p/\Phi_0$ . As seen from Fig. 2.9 b) the lower we tune it, the higher it gets. Though below 3.3 GHz the cold amplifiers in our cryogenic setup stop working. Hence with the design parameters

given above we find this limit to be reached at  $0.473 \text{ m}\Phi_0$ , setting the working point of the penetrating flux. So one can conclude an expected coupling of:

$$\frac{g_0}{2\pi} = 2.33 \text{ kHz} \quad (2.52)$$

In comparison in capacitively coupled doubly clamped nanobeams to CPW MW resonators a vacuum coupling strength of 1.2 Hz was found [21]. With three dimensional nanomechanical structures a coupling of 201 Hz has been realized [16].

# Chapter 3

## Methods and Techniques

In this chapter we discuss the fabrication of the electromechanical hybrid system consisting of a coplanar superconducting microwave resonator terminated by a dc-SQUID with one freely suspended arm. Additionally, we highlight the utilized spectroscopy techniques.

### 3.1 Sample fabrication

The fabrication of Josephson junctions is an established process and well optimized [40, 41] at the WMI. The key process for the successful fabrication of a Josephson junction is form an oxide of controlled thickness between the two superconducting layers. For this, we employ shadow evaporation of aluminum (c.f. Fig. 3.1). Technologically, this is realized using a double layer resist process, where the top layer defines the structures and the bottom layer a support structure with sufficient undercut to allow for two aluminium deposition runs using two different angles of incidence. This process has been optimized for silicon and silicon dioxide substrates. In contrast, for the intended sample, which relies on a silicon nitride supported nanobeam design junctions have to be fabricated on silicon nitride. When changing the substrate material, challenges like an altered substrate resistance impacting the electron beam lithography process and an altered resist adhesion to the substrate's surface might arise and thus define one major part of the project.

Since the most critical part in this work was a proper and reproducible SQUID fabrication as we have seen, we start by a short introduction how to fabricate them and discuss possible alternative strategies. Later the fabrication process is detailed in chronological order.

#### 3.1.1 The shadow evaporation process

The shadow evaporation technique uses two layers separated by an evaporation mask that are deposited in different angles to produce nanometer-scale overlapping structures. In our case we use two aluminum layers and an oxidation in between to create superconducting tunnel junctions, so called Josephson junctions. When combining two Josephson junctions

in one loop dc-SQUIDs are fabricated [33, 41].

A double layer resist system has to be used to create such structures. In particular as top layer *PMMA 950k* (*Allresist AR-P 679.02*) is used, spin-coated to 70 nm which is relatively thin. Moreover this resist has a high writing resolution. The bottom layer consists of 650 nm *PMMA/MA 33%*, (*Allresist AR-P 617.08*) with a much lower exposure dose and decreased resolution.

We have depicted the idea behind a shadow evaporation process in Fig. 3.1 a). As seen

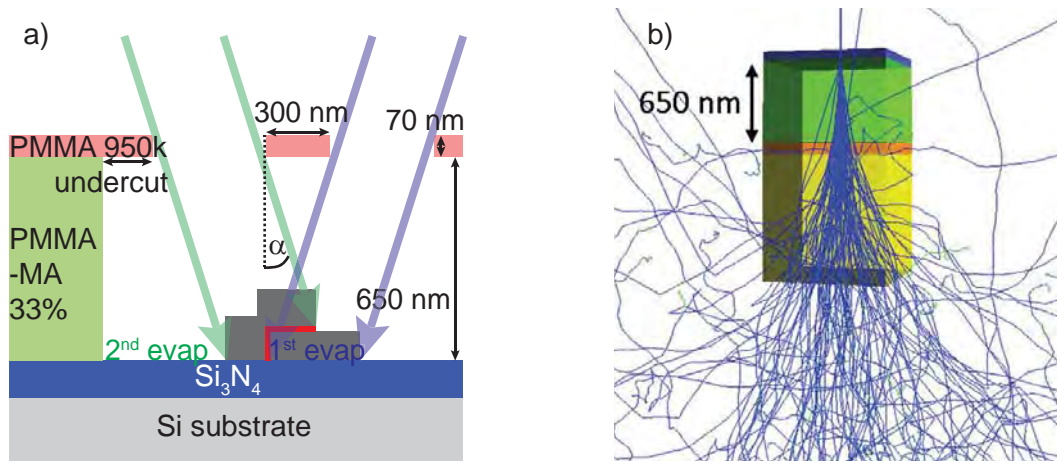


**Figure 3.1:** a) Principle of shadow evaporation as detailed in the text. First under an angle  $-\alpha$  the first aluminum layer is deposited. Next the Al surface is oxidized. In the end a second, thicker evaporation at an angle  $\alpha$  forms the Josephson junction at the overlap area (red). Not to scale. b) Monte Carlo simulation of electron beam structure and scattered electrons, taken from [41]. The focused beam enters from top and spreads out large in the bottom layer (green area) so an undercut is produced.

there the challenge is to write small structures in the top layer, especially the bridge preventing both aluminum layers from shorting. Further large parts from the bottom layer have to be removed, forming the so called undercut. Without or not sufficiently large undercut the evaporation angle becomes to small resulting either in no overlap or an overlap not matching the design.

To create these undercuts one can use two possible methods. First the spreading of the electron beam can be used as shown in Fig. 3.1 b) for the former EBL writing unit at 30 kV acceleration voltage. In the bottom layer (green) the spreading is already large compared to the focused beam coming from top.

Second, increased acceleration voltages like currently 80 kV at the new EBL facility reduce such a spreading drastically. So the beam spot is much sharper in the bottom layer,

allowing to write structures more precisely, hence the so called ghost patterning becomes possible. Here the desired undercut areas are exposed a second time with a lower but sufficiently high dose to exposure the bottom resist.

In principle the undercuts can be further controlled when developing by the temperature and developing time of the bottom layer developer. For the *PMMA/MA 33%* we use isopropanol that can be cooled from room temperature down to 4°C. Though the secondary scattered electrons vary from run to run, so the developing has to be controlled via microscope on large structures. In contrast, the ghost patterning process promises more reproducible results, since it only depends on the dose, which is well controlled.

### 3.1.2 Sample fabrication procedure

This section details the sample fabrication process, illustrated in Fig. 3.2. We start by giving a brief schematic overview of the procedure and discuss each process step individually in the order of the fabrication process.

In the following we focus on the electromechanical hybrid system we finally want to fabricate. Of course for a characterization and controlled fabrication we tested each step and combinations of several, but those deviations from the procedure are explained when presenting the measurement results in the next chapter.

The design itself consists of two contact pads for RF signals, from there the RF-signal is transferred to a transmission line connecting the two rf contacts on opposite sides of the sample. Eight superconducting CPW  $\lambda/4$  resonators with different lengths made of niobium are capacitively coupled to this feedline. At their current anti-node on a silicon nitride patch an aluminum SQUID is placed. One arm of each SQUID is underetched and so has the capability to vibrate.

The fabrication started with a commercial single-crystalline silicon substrate with a 90 nm thick highly tensile-stressed  $\text{Si}_3\text{N}_4$  film on top (Fig. 3.2 a)). First this top layer was removed almost completely except for eight small pads where the nanomechanical elements will be located in the finished device (Fig. 3.2 b)). This was done by optical lithography so optical resist was spin-coated and the structure was exposed directly using a mask-aligner. Process sheet with the specifics of all the process steps will be given in the Appendix A.1. Afterward we transferred the resist pattern to the  $\text{Si}_3\text{N}_4$  layer using reactive ion etching (RIE). Next a 150 nm thick niobium film was sputtered on the chips, which forms the basis of the superconducting CPW resonators. After a lift-off in acetone the niobium was removed from the  $\text{Si}_3\text{N}_4$  patches (Fig. 3.2 c)). Next the MW resonators were patterned via optical lithography (using a direct process on the mask-aligner again) and RIE (Fig. 3.2 d)). Then the SQUIDs are added (Fig. 3.2 e)). For this we used electron beam lithography (EBL) on a double-layer resist system in combination with shadow evaporated aluminum and lift-off. In the end the nanomechanical strings are released (Fig. 3.2 f)).

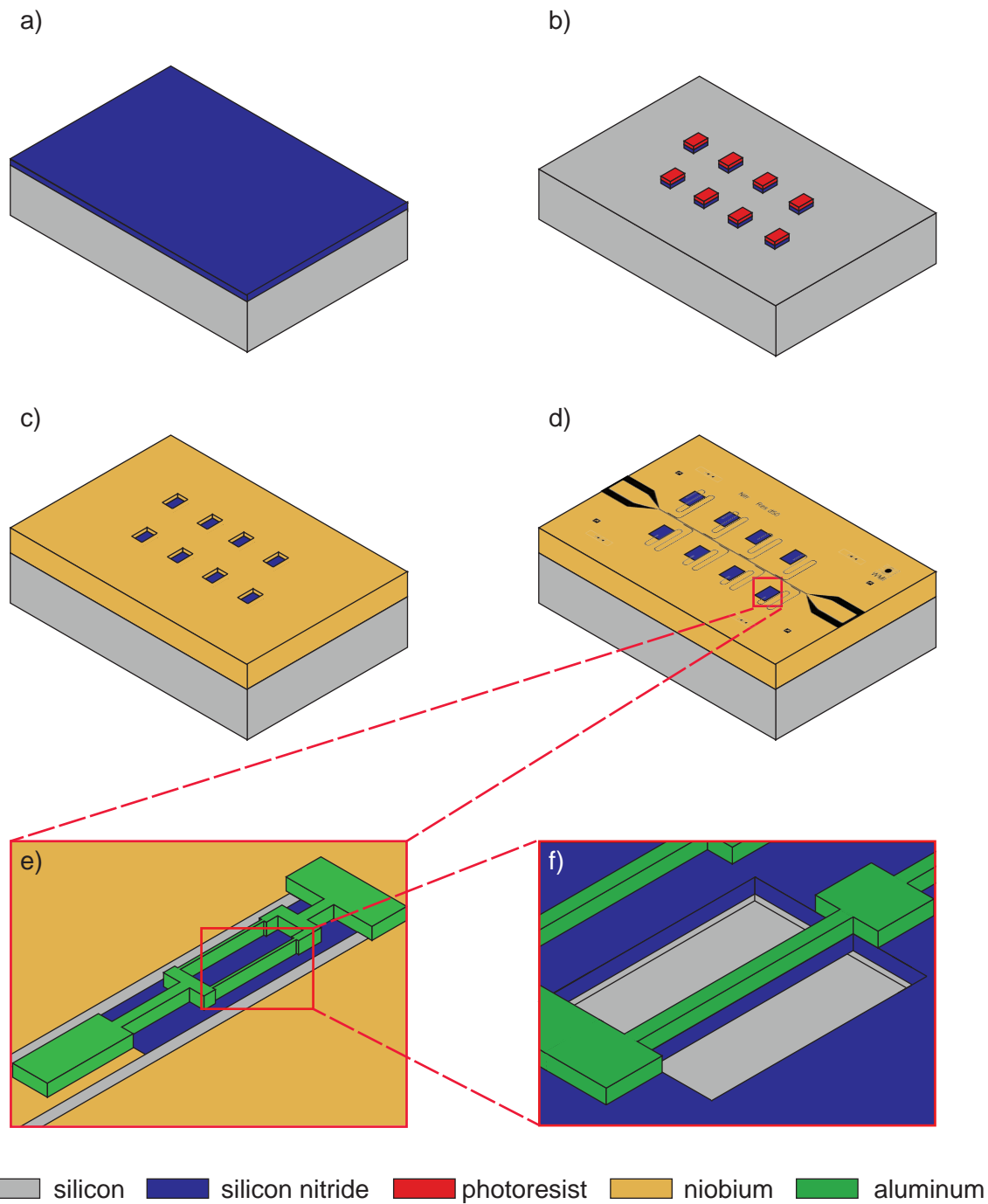


**Figure 3.2:** Schematic overview of fabrication steps. Each step is discussed individually in the text.

To this end we used a resist layer patterned by EBL to protect the rest of the sample and applied anisotropic RIE first, after the underetching was done by isotropic RIE.

An issue in this procedure are the sensitive oxide layers in the SQUIDS, that can easily be destroyed when applying large voltages as we have it here in the final RIE step. Such

details will be discussed below.

Last we like to mention that all figures shown in this section are not in scale because they only have the task to illustrate the process. When possible we moved reoccurring details like the standard direct optical lithography process in the appendix not having to write down same sub steps each time.

### Etching $\text{Si}_3\text{N}_4$ pads for nanomechanical beams

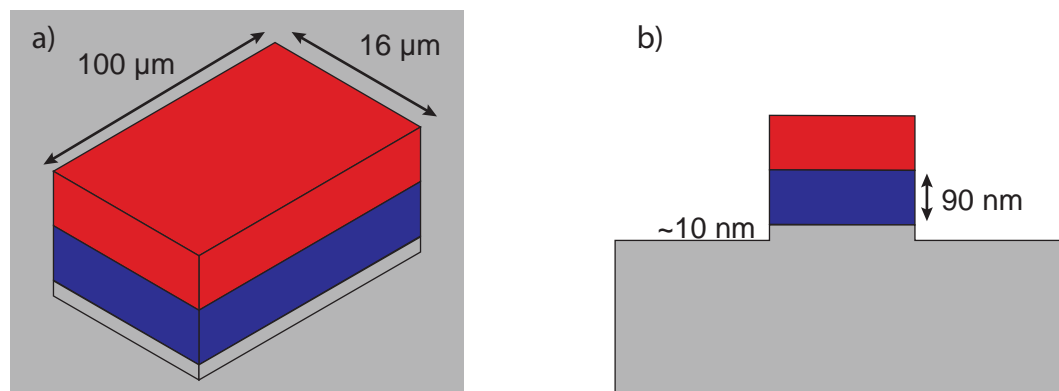


**Figure 3.3:** Details on the silicon nitride patches. a) top view with the  $\text{Si}_3\text{N}_4$  pad sitting on a Si leftover since at least 10 nm was etched into the Si layer. On top optical resist was spin-coated and has to remain for the following step. b) A profile cut through a pad is shown.

The fabrication starts with a commercial single crystalline Si wafer with a 90 nm thin layer of highly tensile-stressed  $\text{Si}_3\text{N}_4$  layer deposited on top. This high stress is very important for our mechanical system since it on the one side increases the resonance frequency so the resolved sideband regime is reached and on the other side reduces the line-width allowing long decoherence times of our electromechanical hybrid system. Such wafers are bought pre-diced in  $6 \times 10 \text{ mm}^2$  rectangular chips coated with a protective resist layer.

Those chips first have to be cleaned using a supersonic bath (*Martin Walther Ultraschall-technik: Powersonic*): 2 minutes in  $20^\circ\text{C}$  at level 9. The chips are put in beakers filled first with technical acetone. After one cleaning the next beaker is filled with acetone and cleaned. Then under a isopropanol flow put into isopropanol (p.a.) and a last time cleaned. Afterward they are blow-dried with nitrogen.

Next we patterned the sample with 8 patches where the  $\text{Si}_3\text{N}_4$  has to remain for our mechanics. Elsewhere it has to be removed since the niobium resonators perform better on Si which might come from its higher dielectric constant. To achieve this we use optical lithography by the direct process on a mask-aligner. This procedure includes spin coating,

baking, exposing and developing. It is detailed in the Appendix A.1. So far there is no structure on the chips so for the alignment one has to make sure to level out pads and sample etches.

After that we use RIE on a *Oxford Instruments Plasmalab 80 Plus*. For anisotropic etching as it is required at this step we use the process *anisotropic etching* as detailed in Appendix A.2. Briefly it starts by pumping down to  $2.7 \cdot 10^{-5}$  mbar before inserting sulfur hexafluoride ( $\text{SF}_6$ ) and argon (Ar) as etching gases. The desired etching depth is at least more than 90 nm, so we make sure all  $\text{Si}_3\text{N}_4$  is removed from exposed areas. Since the etching rate was studied in Ref.[42] we know that 80 s will be sufficient for this.

After the etching, it is important that the photoresist remains on the SiN patches as this resist patches are later used for the lift-off of the niobium. Figure 3.3 displays the state of the samples after this step, where we see the  $\text{Si}_3\text{N}_4$  pad sitting on some Si, since we etched about 10 nm into the Si, on top the optical resist has to remain.

We used optical lithography at this step but it could have been done with electronic beam lithography (EBL) as well.

### Sputtering niobium for superconducting CPW resonators

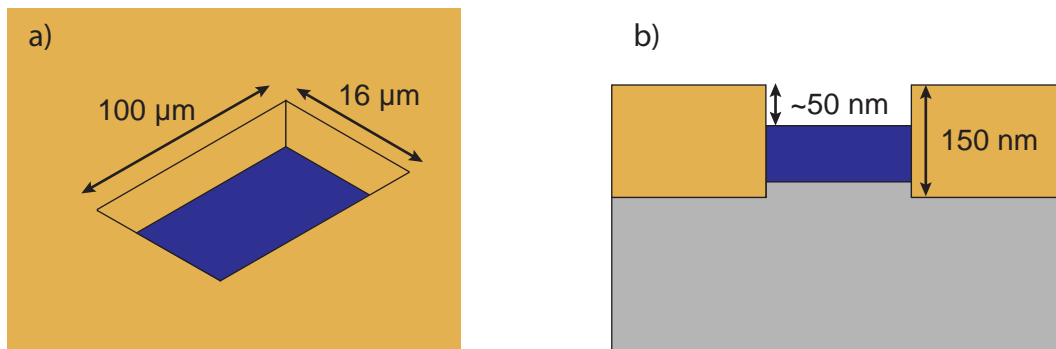


**Figure 3.4:** Details on the niobium sputtering. a) top view indicating the niobium to reach above the silicon nitride. This was chosen so the niobium film is continuous. b) A profile cut through a pad is shown.

For our superconducting MW resonators we have chosen Nb since it has a high critical temperature of 9.2 K [27]. This high temperatures allows us to pre-characterize our resonators simply by cooling it with liquid helium, which simplifies further studies on such MW resonators.

So next the samples were mounted on a carrier to be insert into the thin film cluster at the WMI. Magnetron sputtered niobium was used since this technique is easily accessible and well established in house.

We waited until a pre-pressure of  $2 \cdot 10^{-9}$  mbar were reached and set the magnetrons to a power of 200 W, an argon flow of 20 sccm/min resulting in a process pressure of  $4 \cdot 10^{-3}$  mbar. The power was obtained by a sputter voltage of 275 V and sputter current of 0.736 A.

First 5 minutes of pre-sputtering with closed shutter and then 6 minutes of sputtering was applied leading to a 150 nm thin niobium film. The film is chosen to be thicker than the depth of the previous etching process to ensure a continuous film.

After we applied a lift-off in 70 °C hot acetone (p.a.). This removes the photo resist from the  $\text{Si}_3\text{N}_4$  patches as well as the Nb on top of it. If necessary ultrasound was applied but now not more than level 2 not to destroy the Nb.

The  $\text{Si}_3\text{N}_4$  pads after this step are depicted in Fig. 3.4.

### Producing MW resonators by reactive ion etching

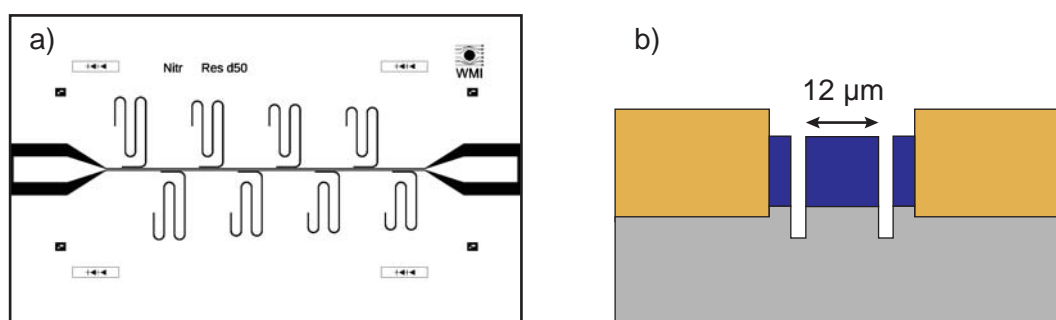


**Figure 3.5:** MW Resonators. a) sample layout: the two RF contact pads are clearly visible. Between them a transmission line is placed across the sample. To this line eight MW resonators meander on the chip being capacitively coupled to it. b) profile cut of the  $\text{Si}_3\text{N}_4$  pads after etching the resonator structure. The effective area for the SQUIDs is reduced to 12  $\mu\text{m}$ .

We used the lift-off from the previous part with hot acetone as first step of a proper cleaning of the samples. Next we used acetone and after isopropanol filled beaker in the supersonic bath at 20 °C on level 2 for 2 minutes, where the sample was transferred under a continuous flow of the next chemical to avoid any streaks or other contamination from the environment. Last the sample was blow dried using nitrogen.

Next the direct process at the mask-aligner was executed. This time with a careful alignment. In case the  $\text{Si}_3\text{N}_4$  pads are misaligned we will not be able to install a SQUID later. So we used the maximum magnification at the microscope to ensure it is. Moreover when aligning the chips have to be pushed up completely against the mask otherwise there might be some drift. But moving the sample when pressed against the mask might leave

some resist particles that can prevent the resonator from working properly later. After exposure the chips were developed. We found best results when cleaning the developer beaker with isopropanol (p.a.) after each developing, so resist particles from former samples are removed.

Then we applied an *anisotropic etching* at the RIE for 90s.

In the end the chips were cleaned with acetone, isopropanol and blow drying as in the beginning of this step in a supersonic bath with same parameters. After each chip and resonator had been checked for any indications of broken resonators, like connections to the ground plane or broken structures. Only the best samples were used for further fabrication.

For our pre-characterization we also produced just MW resonators, see Sec. 4.3. These samples were made as mentioned up to here.

We have already explained that these optical steps could be substituted by EBL processes. Especially here where the alignment is time consuming and has the danger of polluting the sample we recommend to replace this for further studies with an EBL procedure on the new electron beam lithography.

### Adding SQUIDs

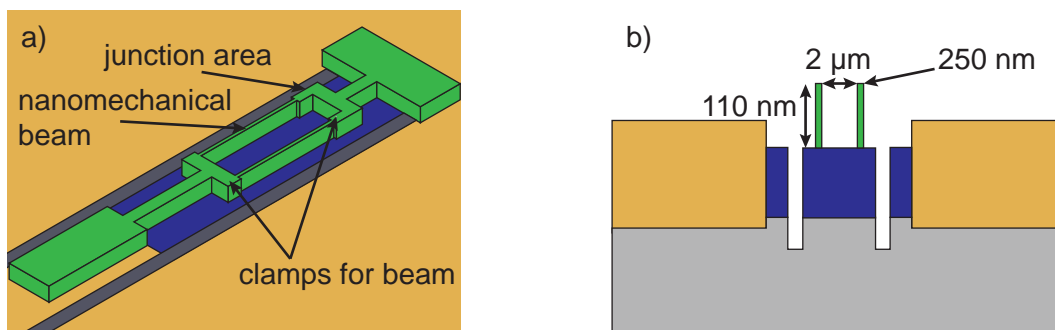


**Figure 3.6:** Adding SQUIDs at the current anti-node of a MW resonator. a) top view with the nanomechanical beam, the clamps and Josephson junctions as indicated b) profile cut through the pad after aluminum evaporation.

Since the chips were cleaned at the end of the last step it can be skipped now when directly proceeding with the fabrication.

Since shadow evaporation is used to produce the SQUIDs first a double layer resist system has to be spin-coated. The idea behind the double layer system is to use a thin layer with high exposure dose and high spatial precision at the top, to write filigree structures into it first. At the bottom a thick layer with a lower exposure dose and low spatial

resolution follows. The lower dose allows to exposure larger areas in it, without influencing the top layer, which ends in undercuts as illustrated in Fig. 3.1 a). We use the resists *PMMA/MA 33%* for the bottom and *PMMA 950k* for the top layer. The spin coating process is detailed in Appendix A.3.

Next the structures are written on a *Philips XL 30 SFEG* scanning electron micrograph system with a *Raith* writing extension. As established at the WMI backscattered electrons are used to produce an undercut. The challenge then is that this process depends crucially on the amount of back-scattered which in turn depend on the machine settings which fluctuates from run to run. To overcome this when developing, the undercut of a large object was verified via microscope [41]. Since silicon nitride appears much darker than silicon it is not possible to judge the undercut by optical inspection. Thus one main challenge in this project was the production of junctions with this technique.

The new EBL facility *nB5 (Nanobeam Ltd.)* has a higher acceleration voltage of 80 kV instead of 30 kV and in contrast to the Philips XL30 it is not a SEM with writing extension where secondary scattered electrons are not disturbing (as long as they are not detected). This reduces secondary scattering electrons drastically and so we use here another technique: the so called ghost pattern via a second exposure with much lower dose. This produces a continuous undercut instead of a cut at the junction. We have depicted this in Fig. 3.7 a) for a broke junction due to not enough undercut which was written on the old EBL. Panel b) with the ghost patterning on the new machine where the undercut was continuous along the aluminum stripe leading to a proper working Josephson junction.

As mentioned the developing time had to be adjusted. We used *Allresist AR 600-56* for 60s and afterward for the undercut isopropanol that we cooled down to about 4 °C, but here as mentioned developing time and temperature had to be adjusted depending on the SEM aperture.

Afterward the Al layers were deposited without heating the chips. We used shadow evaporation technique with the first layer 40 nm thick, rate 10 Å/s under an angle of  $-17^\circ$ . Then the layer was oxidized for 800s by opening the oxygen valve to 45% and a flow of 5 sccm resolving in a pressure of  $5 \cdot 10^{-4}$  mbar. The final layer was deposited with the same rate under  $17^\circ$  until 70 nm were reached.

This was followed by a lift-off in 70 °C hot acetone for 30 minutes. To increase the effect we used a pipette to create a turbulent flow carrying loose aluminum parts away. This was repeated in a second beaker to be sure all aluminum was removed. If possible ultrasound cleaning should be avoided since the Nb/Al contacts are very weak due to oxidation of the Nb. So applying ultrasound can destroy those contacts.

The samples can be measured at this stage as shown in Sec. 4.4. The progress up to here is depicted in Fig. 3.6.

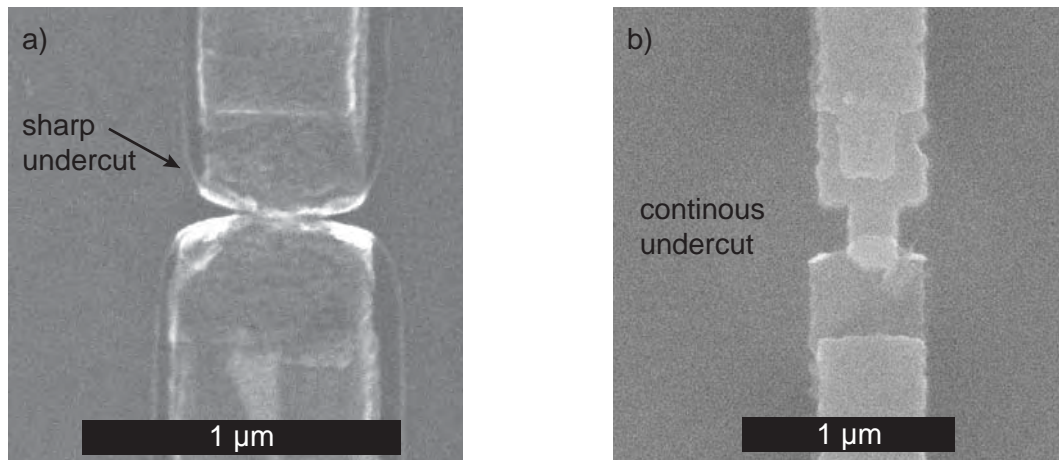


**Figure 3.7:** Overview undercut fabrication. a) junction made by secondary scattering electrons. Undercut vanishes at the junction so does the Al. Junction is not working. b) via ghost-patterning at the new EBL. A continuous undercut is produced at all edges. Junction works properly.

### Release of nanomechanical system

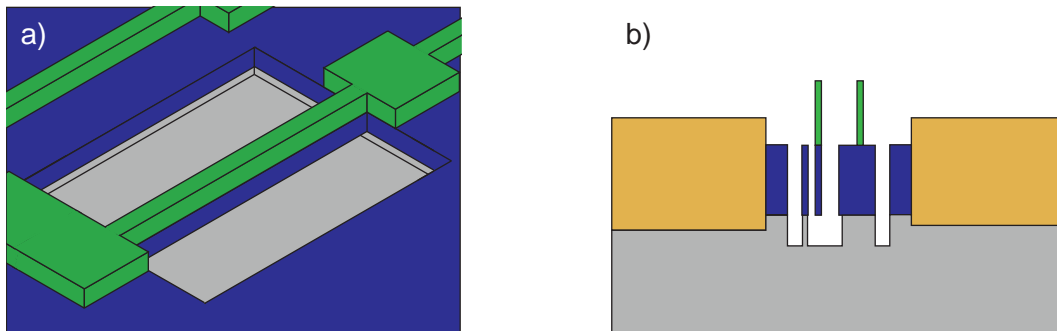


**Figure 3.8:** Releasing the nanomechanical beam. a) top view b) profile

In this final step the aim is to underetch one arm of the SQUID. So first we spin-coated *PMMA/MA 33%* EBL resist. This is the resist also used for the bottom of the double layer system and it is spin-coated exactly as it was done there.

Next we wrote etching windows on the resist via EBL. For alignment we used Al crosses we made in the previous step. This allows very precise positioning of the window to the beam and so very narrow SQUIDs, reducing their sensitivity to magnetic noise.

The resist was developed 30 s in *AR 600-56* and 2 minutes in 8°C isopropanol. Then anisotropic etching via *anisotropic etching* for 2 minutes was applied. On the one side one wants to etch deep so when the resist is removed the surface tension of the acetone does not stick the beam to the substrate. On the other side the resist is not completely etched resistive and sooner or later will start to fail protecting the structure. When etched down the sample can be destroyed. But with the mentioned parameters a compromise was found.

Further the isotropic etching was applied. This was done again using the anisotropic recipe but without argon, an increased SF<sub>6</sub> flow of 50 sccm, a forward power of 5 W, ICP 0 W under a pressure of 50 mTorr for 20 minutes, following the results in [42].

Finally the resist was removed using acetone, isopropanol and nitrogen blow.

In contrast to the steps before we have not applied this one yet to working samples. Results indicate that the SQUIDs tend to be destroyed by this etching process. The idea is to use a protective conductive resist or apply the anisotropic etching first before evaporating the aluminum. But this has to be developed in further investigations.

Though we have released nanomechanical beams in SQUIDs as shown in the colored SEM image in Fig. 3.9, where aluminum parts are colored in green, silicon nitride in blue. a) shows the complete SQUID loop. The two aluminum layers from shadow evaporation are well visible on the vertical connections between the arms. The etching leaves a ridge below the beam coming from the isotropic etching process. Zoom into one Josephson junction (b)) and one clamp (c)) are shown. In b) the coloring was spared to get a higher contrast. It was not possible to remove the resist completely since the SQUIDs are have to be treated carefully. Resist leftovers can be seen in b) as noisy appearing structure. Moreover it reduces the contrast. In c) The right clamp of the arm is shown. Silicon nitride and aluminum layers are indicated. Below the beam the ridge is visible.

## 3.2 Experimental setups

Up to here the idea of an inductive coupling in cavity optomechanics was theoretical described and it was shown how to fabricate such hybrid systems. Next experimental facilities are introduced to characterize all the samples. In particular we start with an interferometer to study the motion of nanometer sized mechanical beams. After three cryostats for experiments on superconducting MW resonators are described with operation temperatures from 1.5 K to 20 mK.

### 3.2.1 Optical interferometry

Optical cavity experiments promise high signal to noise ratio since the detected signal has run through the mirror plates several times. When this thesis was started an interferometer using an optical fiber and a hysteretic piezo stack was established. The working principle

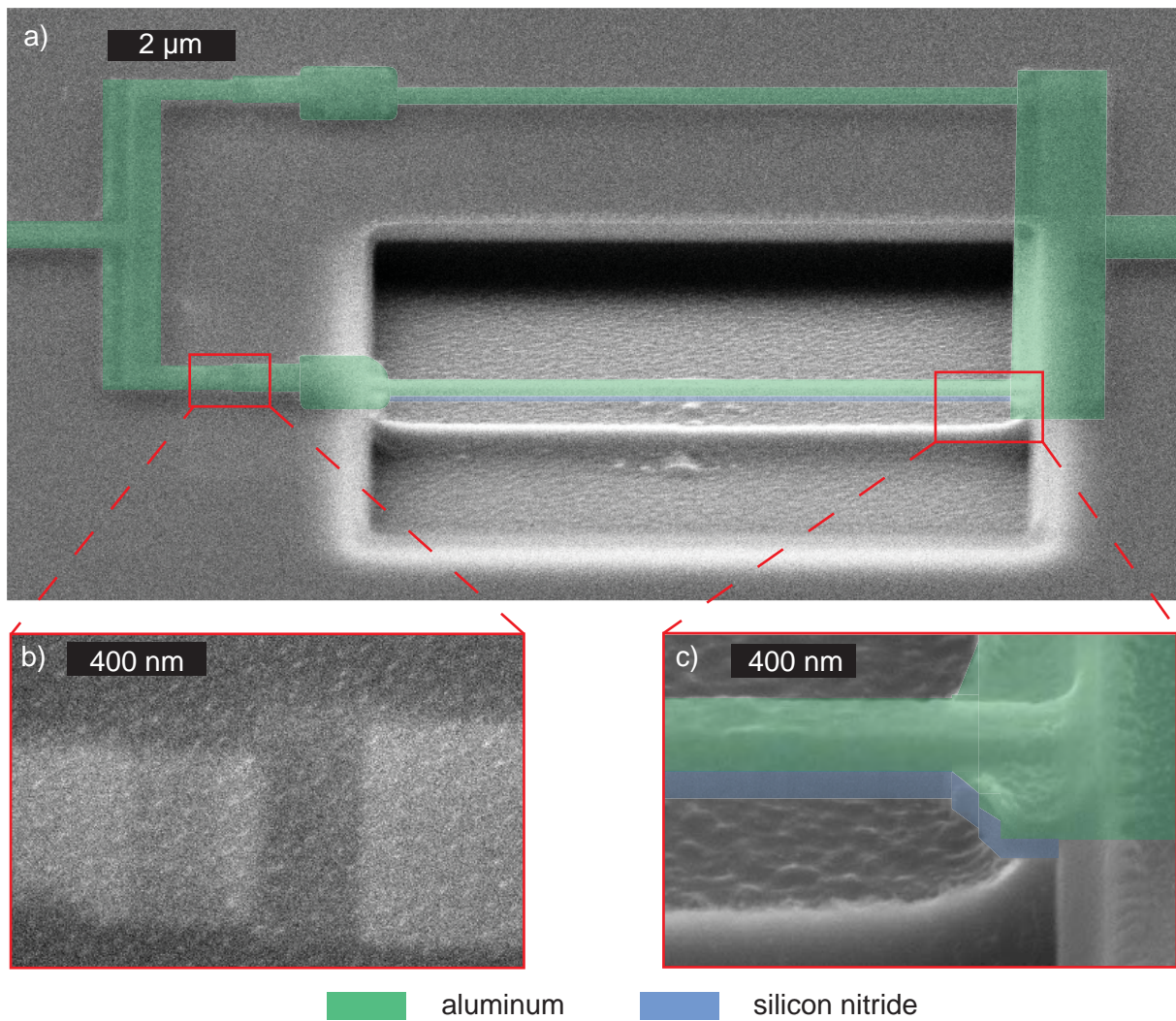


**Figure 3.9:** Colored SEM image of a SQUID with one released arm. a) complete SQUID under an angle of  $60^\circ$ , etched beam in front. b) zoom into one Josephson junction from top view. For a better contrast the coloring was spared. c) Right clamp with underetched beam under an angle of  $60^\circ$ . Further explanation in the text.

is the following:

A red laser beam is focused inside a vacuum chamber by an objective to a nano-beam. The reflected light outside the chamber is focused on a photo detector and transformed in a voltage signal. Sample and objective form an optical cavity, which reflectivity is depending on the position of the nano-beam. In case the beam is swinging in resonance the reflected light is modulated with the same frequency. In our case the mechanical motion is excited via a piezo actuator, on which is the sample is mounted. The vacuum is necessary to suppress damping due to air friction.

In addition to the laser the sample is illuminated with an expanded white light. The

reflected white light is focused on a CCD camera. So a live microscopic image is obtained, allowing to navigate the laser spot relative to the nanomechanical resonator. The sample is mounted on a piezo stack and can be moved in all three directions.

In comparison to a fiber based interferometer such a free beam one has two main advantages:

First the working distance between the optic and the sample is some millimeters large and therefore large enough to avoid contact between the sample and the objective contrary to a fiber based interferometer as discussed in Ref. [43].

Second the additional white light in combination with the CCD allows a quick and easy orientation on the sample. Time consuming rastering on the sample as used in fiber interferometry is not necessary.

To sum up we built this new interferometer during the course of this thesis for characterization of complex cavity electromechanical hybrid samples to get a fast and safe insight on their mechanical attributes.

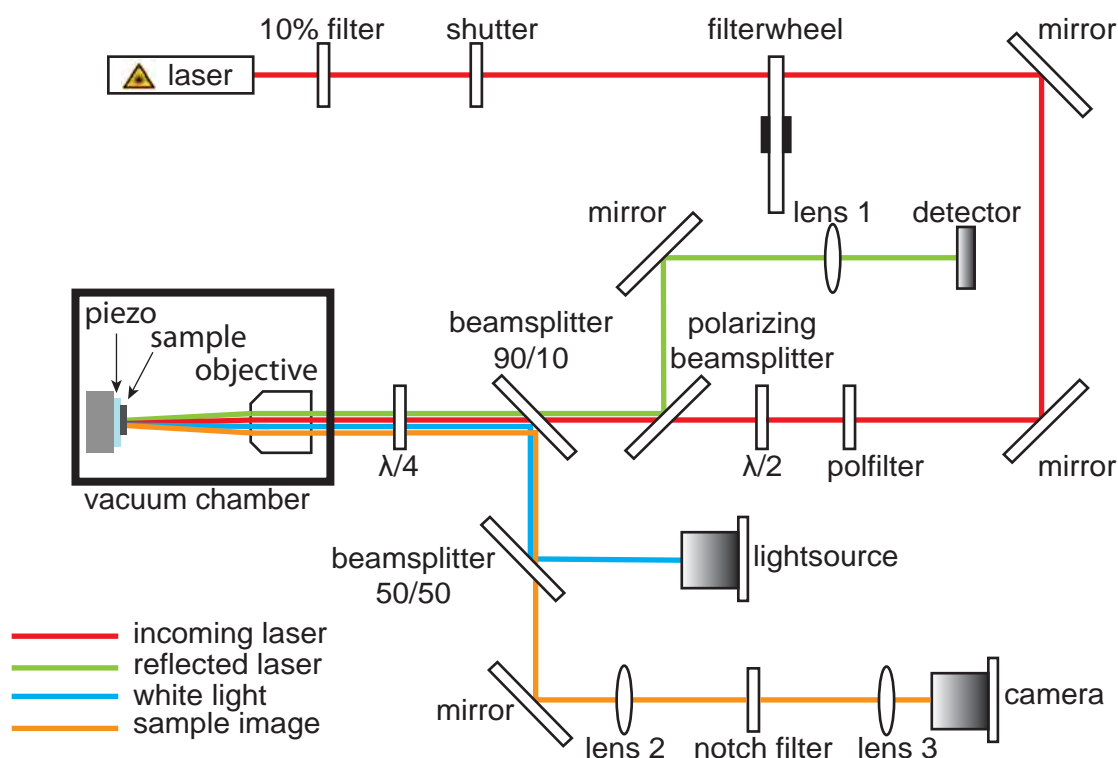


**Figure 3.10:** New free beam interferometer for large distances between nanomechanical beams with in-situ observation. Working principle is explained in the text and a list of parts is attached in the appendix.

The new setup is depicted in figure 3.10.

The laser beam starts at the laser source, followed by a filtering section where one can adjust the required laser intensity. This is important because large laser intensity can

influence the beam, e.g. by heating, and so falsify the results. After that comes the polarizing section. Here we use a polarizing beam splitter to avoid backscattering into the laser source and so an expensive Faraday filter is not necessary. Therefore we have to set the right polarization angle by a  $\lambda/2$  retarder. Past the polarizing beam splitter the laser is circular polarized by a  $\lambda/4$  wave plate. Then it is focused by a microscope objective. After the reflection on the sample the light is polarized again but with a 90 degree phase shift thus completely reflected by the beamsplitter and focused by a lens on the detector. The high level of reflection also allows lower powers on the sample compared to non polarizing optics.

The white light is generated by a LED with a scrim. The beam is coupled to the laser with a 90:10 (transmission : reflection) beam splitter. In the vacuum chamber in contrast to the laser it is not focused by the objective thus a large area on the sample is illuminated. The backscattered light returns on the same path and is transmitted through a 50:50 beam splitter where the LED light is coupled in. The beam then goes through a notch filter filtering the laser wavelength to protect the camera. Before the camera we have installed a focusing lens setup to magnify and adjust the focus spot of the sample. The sample position is controlled by a three axis piezo stack and excited by a piezo actuator.

As depicted in Fig. 2.3 b) the detected signal consists of two products [25]:

$$U_{\text{in}} = A_1 E_1 + A_2(v_{\text{ip}}) E_2(v_{\text{oop}}), \quad (3.1)$$

with the cross section of the laser spot without the beam  $A_1$  and the cross section of the nanomechanical beam  $A_2$ , as well as the frequency independent background signal, scattered at the silicon substrate  $E_1$  and the frequency dependent signal from the mechanical resonator itself  $E_2(v_{\text{oop}})$ . The influence of the first factor in Eq. (3.1) has been discussed in Sec. 2.1.5.

When driving the out-of-plane motion of the beam the signal  $E_2$  is detected since the beam changes the distance between objective and beam surface. So the ratio  $A_2/A_1$  has to be optimized when positioning the sample.

The in-plane motion does not change the signal  $E_2$  but the ratio  $A_2(v_{\text{ip}})/A_1$ . This leads to a frequency dependent change in the detection voltage. So for an optimized detection, the beam has to be positioned at the edge of the laser spot.

### 3.2.2 1.5 K Cryostat

At the WMI we use superconducting niobium for circuit quantum electrodynamics (QED) experiments. It has a critical temperature of 9.2 K [27]. Therefore immersing samples in liquid  $^4\text{He}$  is sufficient to observe superconductivity, although internal quality factors of the MW resonators become higher with decreased temperatures due to reduced number

of quasi-particles [44]. When reducing the pressure of the  $^4\text{He}$  it is cooled by evaporation cooling. Due to binding forces only the hottest particles can escape and so the liquid is cooled. Typically temperatures of about 1.3 K are reached [45].

The cryostat consists of an inset with eight MW cables, so up to four samples can be measured with one cool down. A spacious design leaves enough room for further installations like magnetic or MW shields but those were not necessary for our experiments since we focused on MW resonator characterization. Samples were mounted in gold plated copper boxes and connected to MW pins with silver glue. Because of thermal losses like the MW cables temperatures of 1.5 K are reached.

Since the quality of niobium MW resonators at such temperatures is close to the ones at millikelvin temperatures we used this cryostat for quick pre-characterization of niobium resonators.

The reached 1.5 K are not sufficient for characterizing aluminum samples, having a critical temperature of only 1.19 K in bulk [27], thus advanced setups had to be used.

### 3.2.3 500 mK Cryostat

The 500 mK cryostat uses the principle of evaporation cooling twice as indicated in Fig. 3.11: First liquid  $^4\text{He}$  (bright blue) is used in a Joule-Thomson-cooler to reach 1.5K (dark blue) and condense  $^3\text{He}$  in the sample chamber. Second the the liquified  $^3\text{He}$  is used for evaporation cooling to reach 500 mK (green). Thus those setups are single shot cryostats. The higher latent heat of  $^3\text{He}$  produces a larger cooling power and therefore lower temperatures. So we can immerse our sample in 500 mK cold liquid  $^3\text{He}$  typically. This is enough for experiments with superconducting aluminum.

The inset consists of eight twisted pair dc cables. Additionally a coil can be controlled with an external current source. So up to four 4-point measurements can be performed in one cool down.

Samples are mounted via bonding the pads to copper plates of the sample carrier. For magnetic shielding the whole dewar stands in a screening box and the sample itself is surrounded by an additional  $\mu$ -metal shield.

On this cryostat we tested and characterized the SQUID designs we used, so we were able to get those parameters before building them in the MW resonators.

Since no MW cables are installed combined systems of resonator and SQUIDS had to be measured in a dilution cryostat.

### 3.2.4 20 mK Cryostat ("Kermit")

The cooling mechanisms of both cryostats introduced above are based on the evaporation of  $^3\text{He}$  or  $^4\text{He}$  at ambient or reduced pressure. If  $^3\text{He}$  and  $^4\text{He}$  is combined it forms a miscibility gap at low temperatures [45]. Removing  $^3\text{He}$  from the diluted phase pulls  $^3\text{He}$  from the enriched phase across the boundary. This is similar to an evaporation of  $^3\text{He}$

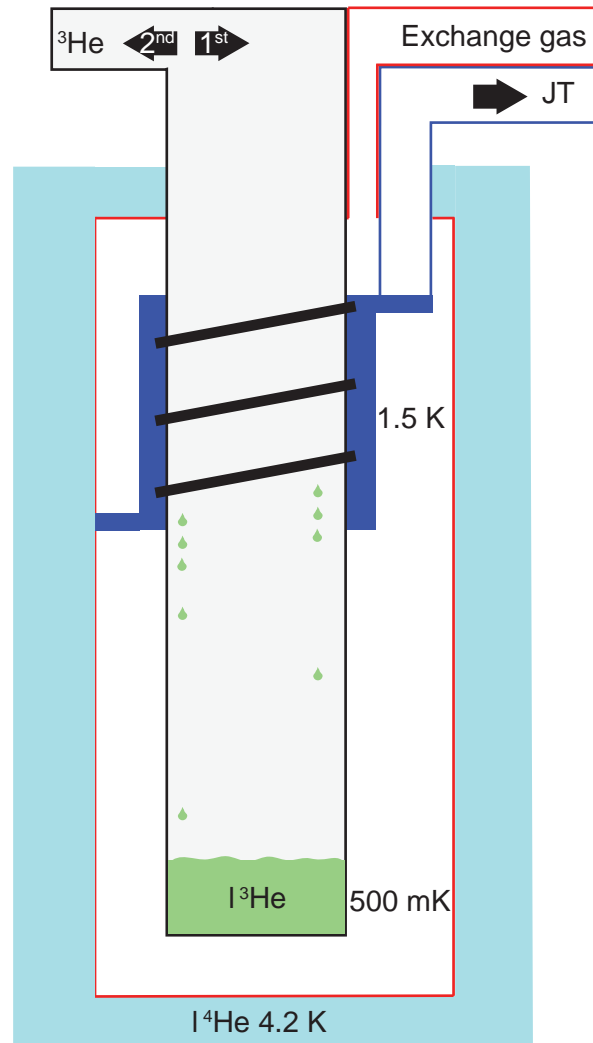


**Figure 3.11:** Scheme of working principle for this  $^3\text{He}$  evaporation cryostat. Not to scale.

from the concentrated phase which cools the systems since latent heat of the evaporation is removed. With this technique temperatures of 1.5 mK can be reached [45]. Due to thermal losses e.g. the microwave cables typically about 20 mK were reached. Moreover in contrast to the single shot evaporation cooling those cryostats run continuously. For our experiments we use the Kermit cryostat shown in Fig. 3.13.

Electric wiring consists of five twisted pair dc twisted pair cables including one superconducting coil. Two MW cables are installed as input and one as an output, so two tone spectroscopy is feasible. The input lines have several attenuators at different temperature stages as seen in figure 3.13 to reduce thermal noise. In total the signal is attenuated by 110 dB. The output line has two circulators to reduce noise from outside and one cold amplifier, adding 40 dB. The innermost shielding is drilled out of 99.5% pure aluminum stick which acts as a superconducting magnetic shielding followed by a copper and brass

shield. In addition the whole 4 K vacuum chamber is surrounded by a  $\mu$ -metal box. The inside of the 4 K vacuum chamber is shown in Fig. 3.13 a).

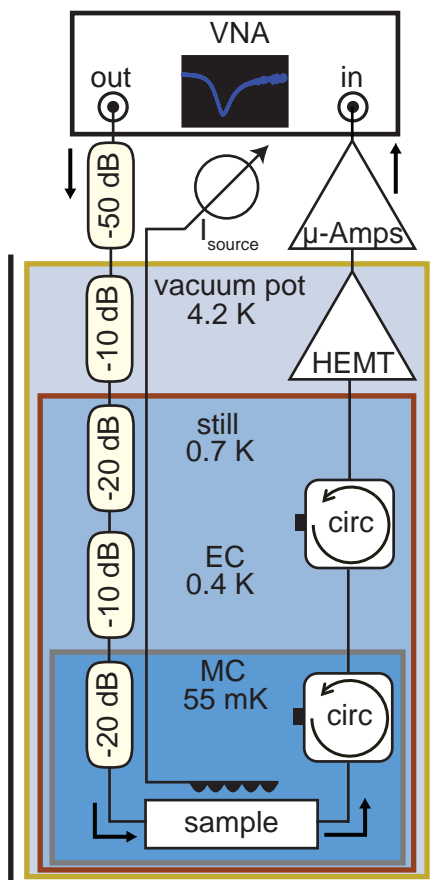


**Figure 3.12:** Scheme of MW wiring and magnetic shielding in this setup. The vacuum pot is surrounded by liquid  $^4\text{He}$  and a  $\mu$ -metal shield (black). It consists of brass (yellow). At the still stage (0.7 K) a copper shield (brown) is used. On that stage also the exchange coil (EC, 0.4 K) is located. After comes the mixing chamber (MC) with the sample. It is surrounded by an aluminum box, acting as perfect diamagnetic shield. In our experiments 55 mK were reached typically. For generation and detection of microwaves a VNA was used. The input lines of the MW are attenuated by 110 dB in total at different temperature stages as indicated. The output line has two circulators to avoid thermal noise on the sample and a cold amplifier (HEMT) at the 4 K stage. In addition a superconducting coil is placed at the sample for magnetic field sweeps.

Samples are mounted in a box and connected with silver glue to MW pins. On top of the lid the superconducting coil can be installed. A picture of this is found in Fig. 3.13 b).

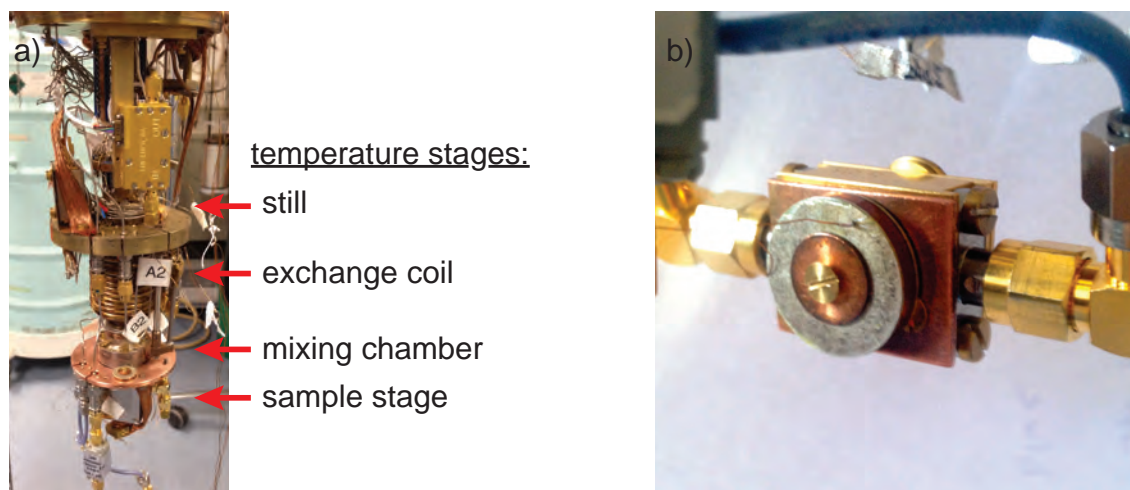


**Figure 3.13:** Panel a) 4 K stage at the "Kermit" cryostat. Temperature stages are indicated. Panel b) Mounted sample box at the sample stage. Sample and superconducting coil are installed, thermocoupling and thermometer not but visible in the background.

# Chapter 4

## Characterization of inductively coupled nano-electromechanical devices

This chapter summarizes the findings obtained on the inductively coupled nano electromechanical devices fabricated through the course of this thesis. This includes measurements on the individual components of the device, like the nanobeam, the dc-SQUID, and the superconducting resonator as well as combinations of the components. In this chapter we find that the current reactive ion etching process employed for suspending parts of dc-SQUID test structures seems to destroy the Josephson junctions and outline suggestions how to overcome this problem.

### 4.1 Mechanical resonators

In Sec. 2.1 we discussed the behavior of nanomechanical  $\text{Si}_3\text{N}_4/\text{Al}$  double layer beams on a theoretical basis and highlighted the fabrications steps in Sec. 3.1.2. In order to investigate their mechanical properties, we setup a new interferometer as detailed in Sec. 3.2.1. We first focus to study the beam properties for different lengths and widths for different drive powers to address the following questions:

- Is the eigenfrequency  $\Omega_0$  for each beam predictable or in other words Eq. (2.3) describes the dependence of the beam length correctly?
- How high are the quality factors? Many applications, such as quantum information storage desire long mechanical lifetimes or low damping. As our systems consist of an Al/SiN double layer, the question arises how the Al thickness affects the quality factor of the nanobeam [46].
- If we analyze the nonlinearity  $\alpha$ , is it consistent with the Duffing theory?
- How about our the pre stress in our aluminum layer? It is not directly accessible but it is desirable to figure it out for future projects with pure aluminum nanobeams [43].

To answer these questions we will focus in the following on the in-plane mode of our mechanical resonator which is required for the electromechanical coupling. Using optical interferometry, we determine the eigenfrequency and quality factor of the nanobeam. Next we investigate the material parameters, e.g. via the Duffing nonlinearity. These parameters can be obtained also via out of plane modes, which is easier to detect, hence allows to collect more data. At the end we summarize our results and derive conclusions about our system.

### 4.1.1 In-plane motion

For analysing the mechanical response of the beam, we use the optical interferometry setup discussed in Sec. 3.2.1. To maximize the mechanical response, we use a vector network analyzer (VNA) to drive the piezo actuator. To detect the mechanical response of the system, we monitor the light intensity at the photodetector (see Fig. 3.10) using the vector network analyzer, as this quantity reflects the amplitude motion of the object. Note, that in principle, the interferometer should detect even the motion of the piezo actuator. Nevertheless, we are mainly interested in the resonant response of the nanobeam, as we focus on its mechanical properties.

In particular, we use the output voltage signal  $U_{\text{drive}}$  of the network analyzer to drive the nanobeam via a piezo actuator. As input we use the photo detection voltage  $U_{\text{in}}$ . Typically, a vector network analyzer records the so-called S-parameter as response. In our case, this scattering parameter is given by  $|S_{21}| = U_{\text{in}}/U_{\text{drive}}$ .

Using  $|S_{21}|$  we calculate the photoresponse by [25]:

$$U_{\text{in}} = |S_{21}| U_{\text{drive}} = |S_{21}| \sqrt{Z P_{\text{drive}}} \quad (4.1)$$

with  $Z = 50 \Omega$  the line impedance and  $P_{\text{drive}} = U_{\text{drive}}^2/Z$  the piezo drive power (i.e. VNA output power) in Watt<sup>1</sup>. The detected motion amplitude  $A_{\text{m}}$  is proportional to the photo voltage  $A_{\text{m}} \propto U_{\text{in}}$  [25].

The sample chip investigated is labelled "SiNRes7". This chip consists of eight beams with lengths varying from 10 to 70  $\mu\text{m}$ , a width of 250 nm as well as thicknesses of 90 nm  $\text{Si}_3\text{N}_4$  and 110 nm Al. Using this test beam pattern, we can experimentally check for the optimal mechanical eigenfrequency of the later used Al/SiN nanobeam.

A typical result for nanomechanical response is shown in Fig. 4.1 for the in-plane mode of the 60  $\mu\text{m}$  long beam. In panel a) we plot the detection voltage  $U_{\text{in}}$  as function of

<sup>1</sup>If  $S_{21}$  is given in dB and the output power in dBm they have to be transformed in linear units with the standard transformation:

$$|S_{21}| = 10^{\frac{1}{20} S_{21}(\text{dB})} ; P_{\text{drive}} = 1 \text{ mW} \cdot 10^{\frac{1}{10} P_{\text{drive}}(\text{dBm})} \quad (4.2)$$

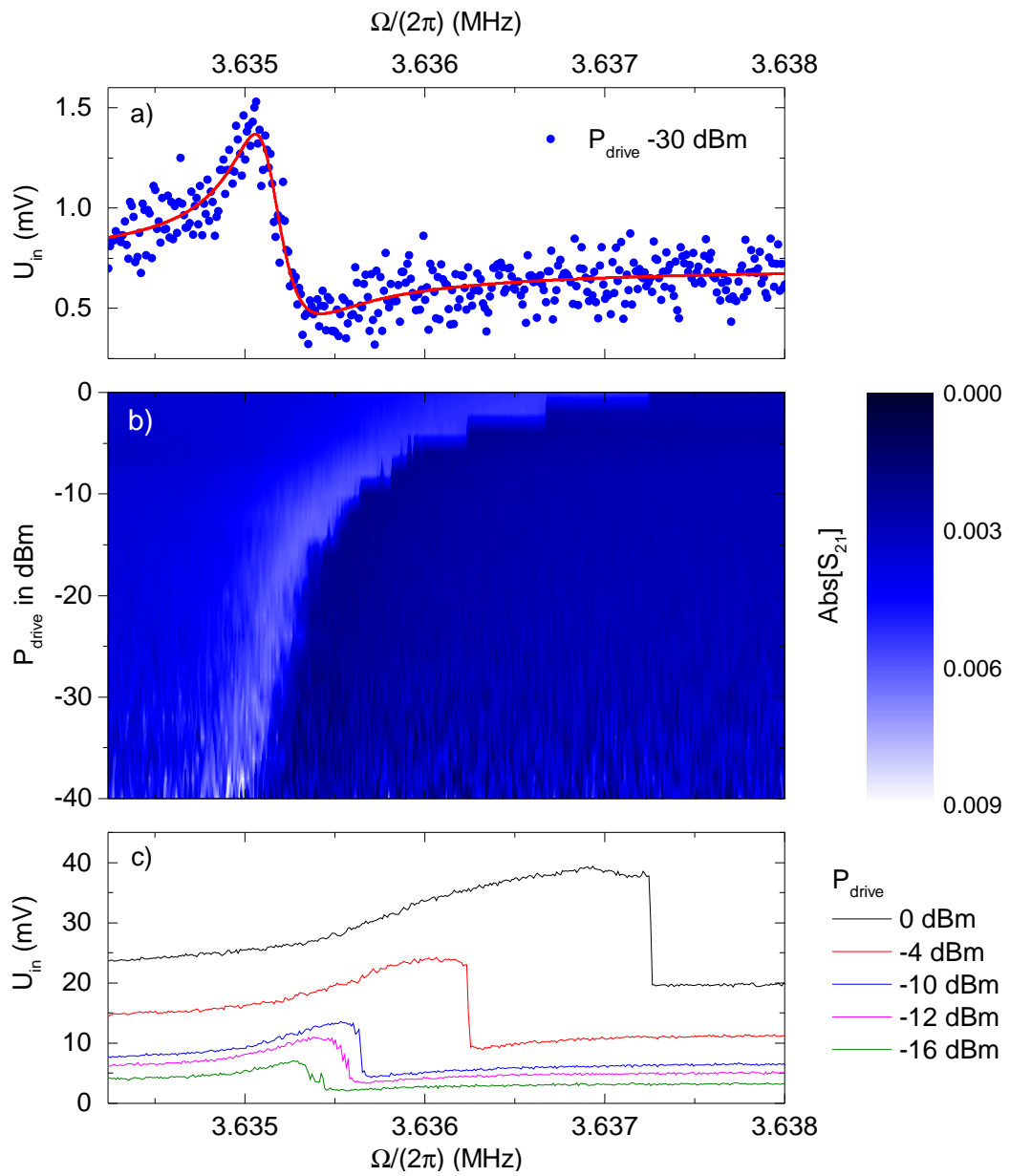


**Figure 4.1:** Example of an in-plane motion for a double clamped,  $60 \mu\text{m}$  long nanomechanical beam with a  $\text{Al-Si}_3\text{N}_4$  double layer from chip SiNRes7. a) Single frequency sweep at  $P_{drive} = -30$  dBm which was used to determine resonance frequency and Q factor of the beam motion. In blue the measured data-points, red shows the corresponding Lorentzian fit with  $\Omega_m/(2\pi) = 3.63512$  MHz and  $\Gamma_m = 277$  Hz. b) Overview for 0 to -40 dBm drive. The Duffing shift to higher frequencies is well visible, indicating a Duffing parameter  $\alpha > 0$  similar to a stiffer spring constant for higher drives. c) Detected photo voltage for selected drive powers between 0 and -16 dBm. At higher values Duffing shape with the typical shark fin cut-off is observable indicating a bifurcation. With lower drive power the shark fin shape transforms to a Lorentzian.

the excitation frequency at a low drive power of  $-30$  dBm as blue dots. We find linear mechanical response with a Lorentzian line-shape including a complex background as derived in Sec. 2.1. We can model this response with

$$U_{\text{in}}(\Omega) = \sqrt{A_p \cdot |C|^2 + b_1} \quad \text{with } C = \frac{\Gamma_m}{i(\Omega - \Omega_m) + \frac{\Gamma_m}{2}} + ib_2. \quad (4.3)$$

Here,  $\Omega$  is the applied drive frequency  $\Omega$ ,  $\Omega_m/(2Pi)$  is the mechanical resonance frequency,  $\Gamma_m/(2\pi)$  the *full linewidth at half maximum* (FWHM),  $A_p$  is a scaling factor, as well as  $b_1$  representing the background offset and  $b_2$  the complex background. The latter was required to account for the fano-like peak-dip feature. As beam linewidth broadens, when the response starts to become nonlinear, we use a drive power of  $-30$  dBm or  $1 \mu\text{W}$  for actuating the chip. As we see later, using this power we are in the linear drive regime and thus are able to extract the mechanical quality factor.

From the fit in panel a) (red line) we determine a resonance frequency of  $\Omega_m/(2\pi) = 3.635$  MHz. Taking into account an effective mass of the beam we are able to calculate the corresponding to a zero-point fluctuation amplitude  $x_{\text{zpf, RT}} = 16.2$  fm at room temperature. With a well optimized fabrication for a  $60 \mu\text{m}$  long beam and  $\text{Si}_3\text{N}_4/\text{Nb}$  double layers  $30$  fm were achieved [47].

Further, we determine a linewidth of  $\Gamma_m/(2\pi) = 277$  Hz, which corresponds to a quality factor of:  $Q_m = \Omega_m/\Gamma_m \approx 13.000$ . Note, that this Q factor is decrease by about a factor of 6 compared to a pure silicon nitride beam of similar geometry. Ref. [46] showed that the quality factor in metalized beams is lower than in pure  $\text{Si}_3\text{N}_4$  based systems. Indeed in pure silicon nitride we have a quality of about 80 thousand at room temperature [25]. Most of this reduced Q factor might be attributed to the typically lower tensile stress in the metallic thin films. Note, this loss mechanisms crucially depend on the temperature and thus SiN as well as metallic nanobeams show a enormous increase in their quality factors as for lowered temperatures [46].

The excitation of the beam at higher drive powers in shown in Fig. 4.1b) and c). The density plot b) shows the linear transmission coefficient  $|S_{21}|$  color encoded as function of the driving frequency  $\Omega$  and the drive power  $P_{\text{drive}}$ . At low powers the quality is not changing, matching to our chosen  $-30$  dBm analysis. At higher drive powers the peak signal broadens and shifts to higher frequencies. The latter indicates a positive Duffing constant  $\alpha$ . For clarity we show the photo voltage for selected drive powers in c), where is broadening becomes more obvious. Here, the shark fin curve is clearly observable for high drive powers. The strong cut-off indicates a bifurcation present in the dynamics.

Up to now, we have looked at an in-plane mode of the nanobeam since this mode is later relevant for the electromechanical coupling. The respective out-of-plane mode is presented in the appendix (Fig. B.3).

In the further analysis we are mostly interested in the material parameters of the double layer beam. For this we investigate the out-of-plane mode as it shows a higher signal.

The theory predicts no frequency difference between those modes in first approximation, see Eq. (2.1).

### 4.1.2 Duffing analyses of out-of-plane modes via lock-in detection

The VNA allows only for an increase of the frequency stimulus. Thus, to analyze the full hysteretic response of the mechanics, we switch it for a high frequency (Zürich Instruments HF) lock in amplifier providing the possibility to ramp the frequency stimulus in both directions.

As sample we use SiNRes10. Here, all beams have a length as the previous sample chip but width is 300 nm and the aluminum layer is again 110 nm on top of the 90 nm SiN. Deviations in frequency compared to the more narrow nanobeams indicate low stress in the material due to Eq. 2.1.

In Sec. 2.1 it was shown that the Duffing parameter  $\alpha$  is determined from the slope obtained by plotting the square of the beam displacement as function of the difference between the cut-off frequency  $\Omega_{\text{eff}}$  and the resonance frequency  $\Omega_{\text{m}}$ . Technically, one challenge is the complex background observed in Fig. 4.1 a), which obscures the beam displacement. To overcome this issue we employ the approach discussed in Sec. 2.1, which is based on rotating the complex valued dataset taking the form of a resonance circle. We then get pure Lorentzian peaks at low drive powers. An example dataset before and after this correction is depicted in Fig. 2.5.

Figure 4.2 a) shows the corrected linear transmission parameter for downsweeps from -39 to 27 dBm for a 30  $\mu\text{m}$  long beam. At low drive power the expected Lorentzian resonance is observed. Increasing the drive power above 10 dBm transforms the line shape to a shark fin response curve with respective cut-off frequency  $\Omega_{\text{eff}}$  higher than  $\Omega_{\text{m}}$ . This indicates a positive  $\alpha$  or in a mechanical picture a stiffer spring constant.

To show the analysis process we have depicted the photo voltage over drive frequency for selected drive powers in both sweep directions in Fig. 4.2 b). Again at lower drive power (10 dBm) a mostly Lorentzian line shape with a slight asymmetry to the right is observed still showing no hysteretic behavior. For higher  $P_{\text{drive}}$  a hysteretic behavior is observed stemming from the bifurcation of our nonlinear system. Thus by recording both frequency ramp directions we are able to measure the bistability of our mechanical oscillators.

For frequency up-sweeps the shark fin cuts off at the effective frequency  $\Omega_{\text{eff}}$ , for downsweeps at the turning frequency  $\Omega_{\text{turn}}$ , as seen in Fig. 4.2 b)  $\Omega_{\text{m}} < \Omega_{\text{turn}} < \Omega_{\text{eff}}$ .

For a quantitative analysis we extract those frequencies and the respective photo voltage  $U_{\text{crit}}$ . The relation between those parameters and  $\alpha$  was derived in Sec. 2.1:

$$v_{\text{max}}^2 = \frac{8}{3} \frac{\Omega_{\text{m}} m_{\text{eff}}}{\alpha} (\Omega_{\text{eff}} - \Omega_{\text{m}}) \quad (4.4)$$

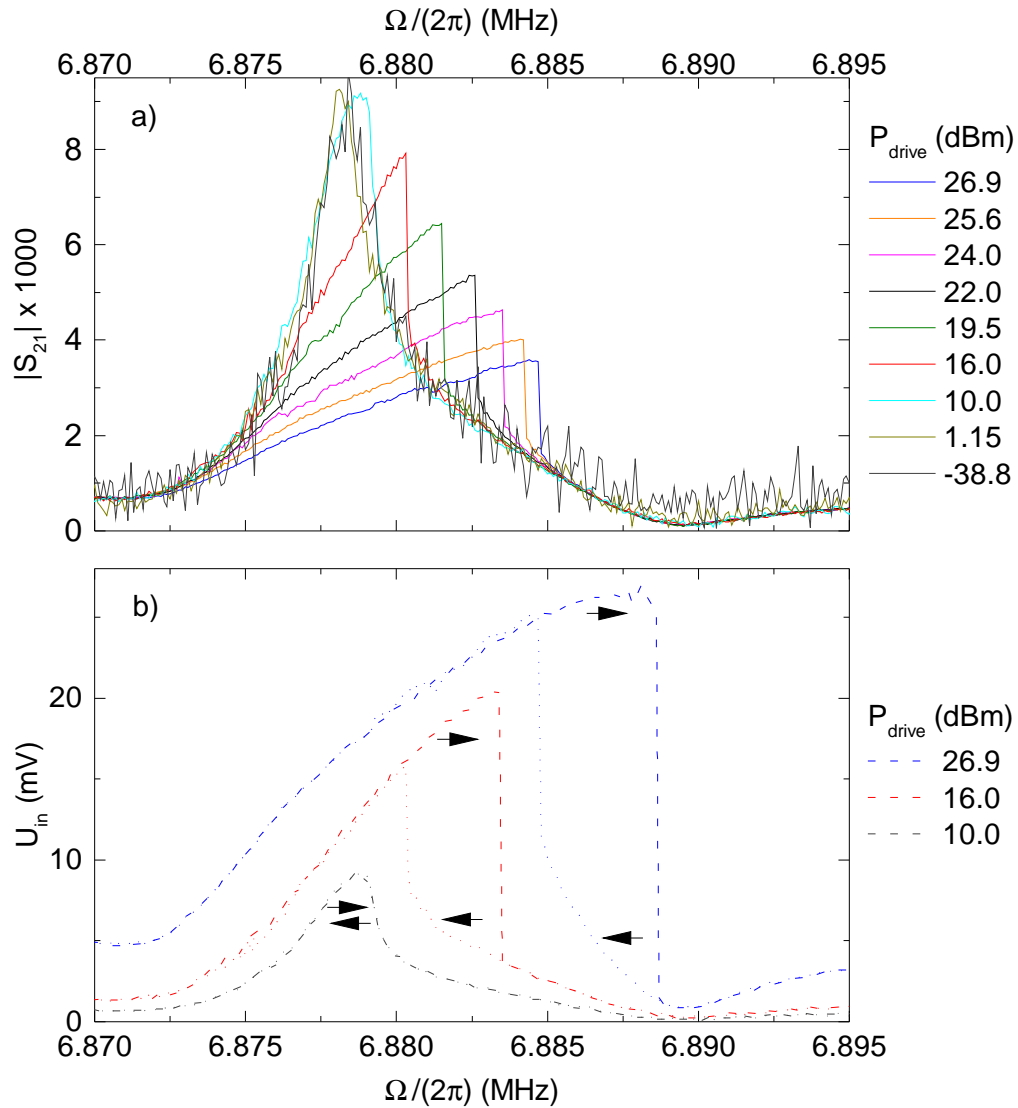


**Figure 4.2:** out-of-plane mode of a 30  $\mu\text{m}$  long beam from sample SiNRes10. a)  $|S_{21}|$  in down sweep direction from -39 to 27 dBm. At low drive powers the shape is Lorentzian. Increasing the drive power broadens and shifts the resonance. Also a sharp cut-off is observed. b) Deflection in the Duffing regime for selected drive powers (10 to 27 dBm) via plotting photo voltage over drive frequency in both sweep directions. An hysteretic behavior is clearly observed for higher drive powers corresponding to a bistability being of interest for future applications.

with the amplitude of the beam displacement  $v_{\text{max}}$  and the effective mass  $m_{\text{eff}}$ . For a quantitative evaluation of the damping parameter  $\alpha$  and henceforth the Young's modulus of the system, a calibration of the transfer function relating the photo voltage  $U_{\text{in}}$  with the displacement  $v$  is required. Nevertheless, calibration was not possible the signal-to-noise ratio was not sufficient to resolve the Brownian noise signature of the beam using the spectrum analyzer function of the lock-in. Note, that the Brownian noise signal resembles

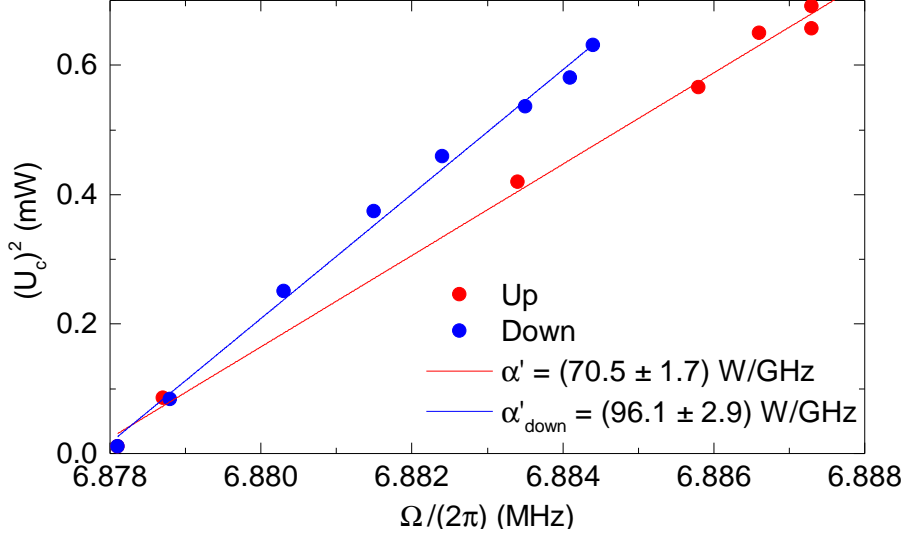


**Figure 4.3:** Critical power over cut-off frequency for both sweep directions with linear fit corresponding to the  $\alpha$  constants. Up-sweep direction is kept red, down-sweep blue. The linear behavior is well reflected.

the calibration gold standard, as it relates average displacement with the temperature, the quality factor and the resonance frequency of the nano-beam. Presently, we think that the reduced average pre-stress of the beam due to the aluminum layer results in an increased damping rate hindering the detection of the Brownian motion. So we can only look at the uncalibrated  $\alpha$  parameter:  $\alpha' \propto \alpha$ .

For that we plotted  $U_{\text{crit}}$  over  $\Omega_{\text{eff}}$  ( $\Omega_{\text{turn}}$ ) to derive  $\alpha'$  ( $\alpha'_{\text{down}}$ ) which is shown in Fig. 4.3. The data-points fit the linear relation well, for which we get  $\alpha' = 70.5 \pm 1.7 \text{ W/GHz}$  and  $\alpha'_{\text{down}} = 69.1 \pm 2.9 \text{ W/GHz}$ . Solving equation (2.19) leads to an equation linking  $\alpha$  and  $\alpha'_{\text{down}}$  by calculating the driving force of the sample  $F_0$ .

Both  $\alpha$ s are positive as expected from the deflection graphs. Further analysis is challenging though since our data is not calibrated.

In the future we recommend to study this with lower damped samples that can be calibrated. Then this new method allows to investigate the forces at the beam and so directly measure the beams sensitivity instead of the theoretical determining via the zero-point fluctuations.

### 4.1.3 Material analysis of our mechanical systems

We have fabricated two nanobeam test chips (SiNRes 7 + 10) containing beams of different lengths and widths. Up to now we only showed one in-plane mode of SiNRes7 and one out-of-plane from SiNRes10. Next, we like to summarize all data on the mechanical

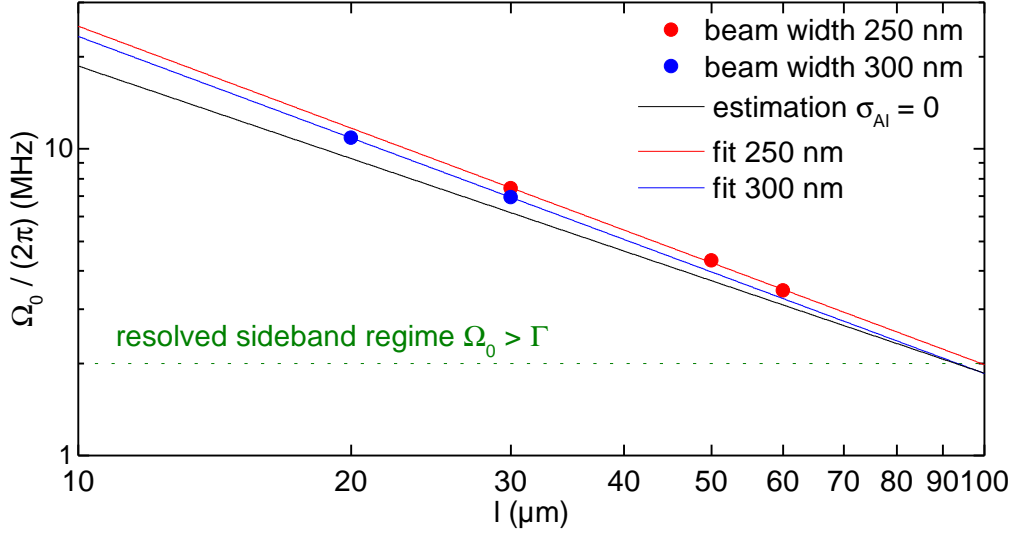


**Figure 4.4:** Resonance frequency as a function of beam length. 250 (red, sample SiNRes7) and 300 (blue, sample SiNRes10) nm beam widths are shown, where the broader ones have lower frequencies. Estimated resonance frequencies are shown with a black line using Eq. (2.3) under the assumption of no stress in the aluminum layer. Measured frequencies are all above this estimation. Slope of the resonance frequencies was -1.1, slightly different than theory proposing -1.

properties and compare it with theory, which predicts

$$\Omega_0 = \frac{\pi}{l} \sqrt{\frac{\sigma_{\text{eff}}}{\rho_{\text{eff}}}}. \quad (4.5)$$

Figure 4.4 shows all resonance frequencies measured for the various beams as function of the length of the beam  $l$ . Here, we find resonance frequencies ranging from 3 to 12 MHz for beam lengths between 20 to 60  $\mu\text{m}$  following the expected  $1/l$  trend.

Further, we added the predicted behavior by Eq. (4.5) using the material parameters  $\rho_{\text{eff}} = 2918 \text{ kg / m}^3$  composed of  $\rho_{\text{SiN}} = 3184 \text{ kg / m}^3$  [48] and  $\rho_{\text{Al}} = 2700 \text{ kg / m}^3$  [49] with the respective film thicknesses. Additionally  $\sigma_{\text{eff}} = 374 \text{ MPa}$  using  $\sigma_{\text{SiN}} = 830 \text{ MPa}$  [50] and assuming  $\sigma_{\text{Al}} = 0 \text{ MPa}$ , since we expect the stress in the aluminum layer to be small compared to silicon nitride.

Though our measured frequencies are all higher, up to 20.5%. This indicates that the stress was not as small as expected, so  $\sigma_{\text{Al}} > 0$ .

To determine  $\sigma_{\text{Al}}$  we first averaged our data-points per resonator length and modeled it with the standard equation of a  $\lambda/2$  resonator:  $\Omega_m = \pi/l \cdot v_{\text{phase}}$ . So a phase velocity of  $431 \pm 3 \text{ m/s}$  was determined. This corresponds to  $(\sigma_{\text{eff}}/\rho_{\text{eff}})^{1/2}$ . In combination with Eq.

(2.2) we get:

$$\sigma_{\text{Al}} = \frac{v_{\text{phase}}^2 \rho_{\text{eff}} (t_{\text{SiN}} + t_{\text{Al}}) - \sigma_{\text{SiN}} t_{\text{SiN}}}{t_{\text{Al}}} = 306 \text{ MPa.} \quad (4.6)$$

Additionally, we find two more interesting phenomena. First, broader beams have a lower resonance frequency than more narrow ones. In theory the width of the beam was assumed to be neglectable. Second fitting the data with  $\Omega_{\text{m}} = a \cdot l^x + \text{Offset}$  returns  $x = -1.1$  instead of -1 for both beam widths.

These two observations show that the stress in our double-layer system is not large enough to fully satisfy the approximation of a highly pre-stressed one. To explain this we have to look at the energies in the beam, where we find an elongation, torsion and bending one [26]. Equation (4.5) assumes the last two of them to be small compared to the elongation energy. But if this is not the case the beam profile is deviating especially at the clamps. So short beams differ more than longer ones from the predicted theoretical model, which is exactly what we observe in Fig. 4.4. The low pre-stress can only be obtained by  $\sigma_{\text{Al}} < \sigma_{\text{SiN}}$  and indeed we determined above:

$$0 < \sigma_{\text{Al}} = 306 \text{ MPa} < \sigma_{\text{SiN}} = 830 \text{ MPa} \quad (4.7)$$

In Fig. 4.4 we have indicated the resolved sideband regime which is the case if  $\Omega_{\text{m}} > \Gamma$  with  $\Gamma = 2\pi \cdot \text{FWHM}$  of the MW resonator. We will show that later that  $\Gamma/(2\pi)$  is about 2 MHz. Since all mechanical resonance frequencies are above this value beam lengths almost up to 100  $\mu\text{m}$  are possible, leading to high coupling strength<sup>2</sup>.

## 4.2 SQUIDS on silicon nitride

The complete inductively coupled optomechanical system is comprised of a  $\lambda/4$  CPW resonator with a SQUID located at the anti-node where one arm of it is layed of in form of a nanomechanical beam. As we have seen in the previous section to obtain high mechanical quality factors we employ the high tensile stress of the silicon nitride substrate. Hence, the dc-SQUID has to be fabricated on this substrate material. In this regard the section on dc-SQUIDS on silicon nitride focuses on the following points:

- Is it technically possible to fabricate dc-SQUIDS on silicon nitride as substrate material ?
- How do the SQUIDS perform compared to the identical SQUID layout on a  $\text{SiO}_2$  surface?

---

<sup>2</sup>As shown in Sec. 2.1, the resonance frequency of the nanobeam depends on temperature due to the different thermal expansion coefficients of Si,  $\text{Si}_3\text{N}_4$ , Al. Using  $\alpha_{\text{Si}} = 2.5 \cdot 10^{-6} \text{ K}^{-1}$  [51],  $\alpha_{\text{SiN}} = 3.2 \cdot 10^{-6} \text{ K}^{-1}$  [52] and  $\alpha_{\text{Al}} = 23.1 \cdot 10^{-6} \text{ K}^{-1}$  [53] we expect a relative frequency increase of 30% when cooling the sample down to mK temperatures, see Eq. (2.7). For a rough approximation of the resolved sideband limit, we neglect this resonance frequency change.

After optimizing the EBL exposure dose for writing on a Si/SiN substrate, we fabricated dc-SQUIDs onto the SiN layer. An example of such dc-SQUIDs is shown in Fig. 4.5 where panel a) shows a photograph of the sample SiNSquid 3, b) a microscope picture from a single SQUID and c) an SEM image of one of the Josephson junctions in detail. Next, we measured their performance using the 500 mK cryostat described in Chap. 3.2.3.

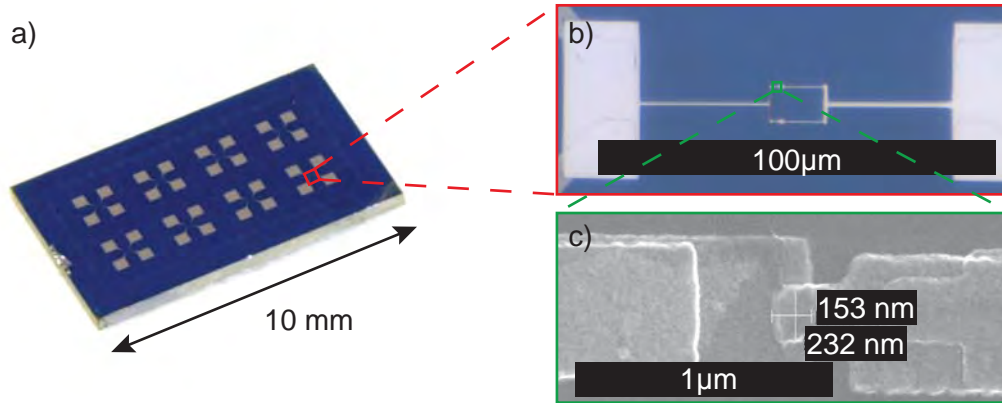


**Figure 4.5:** Fabricated SQUID in several enlargement steps. a) Photo of sample SiNSquid3, whole sample is shown with dimensions of  $10 \times 6 \text{ mm}^2$ . Each SQUID has 4 contact pads pointing to the middle b) Microscope image of one of the SQUIDs. Two of each contact pads are shorted by aluminum for 4-point-measurements later. c) SEM image of a single junction. Both evaporation layers from the shadow evaporation are visible. Typical distance between them is about 400 nm. Josephson Junction dimensions are displayed.

More precisely, we measured U-I curves to determine the gap voltage  $V_g$  and the normal resistance  $R_n$ . Furthermore, the critical current  $I_c$  is derived from measuring the maximal critical current as function of the magnetic field (see Fig. 4.6 b)). To gain better insight in the differences between Si and  $\text{Si}_3\text{N}_4$  substrates we produced two chips with completely identical fabrication parameters one for each substrate and compared their performances.

### 4.2.1 U-I characteristics:

The standard way to characterize a dc-SQUID is to measure its current-voltage characteristics as function of the applied magnetic field with normal incidence to the SQUID loop. A typical current-voltage curve is displayed in Fig. 4.6 a).

This typical dataset is measuring current bias. When ramping up the current, initially, the dc-SQUID remains in the superconducting state, at about  $I_{\text{bias}} = 1 \mu\text{A}$  the dc-SQUID switches to the normal state, resulting in a detectable voltage drop of  $V_g \approx 350 \text{ mV}$ . We call this the switching current  $I_s$ . When further increasing the current, we observe a linear

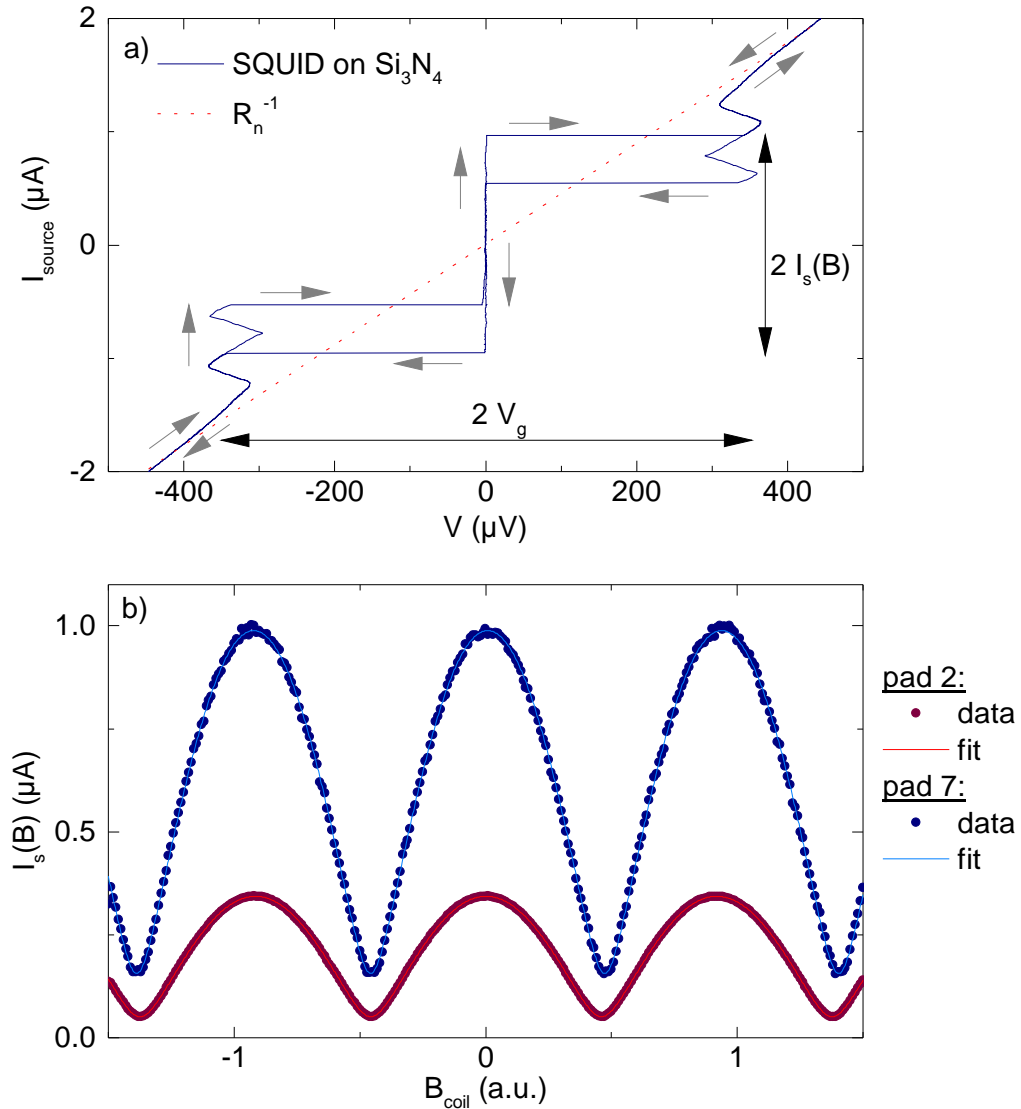


**Figure 4.6:** Typical results measured on the chip SiNSquid8. a) U-I characteristics of SQUID #6. From the abrupt change in the detected voltage across the SQUID we determine the switching current  $I_s$  to be  $1 \mu\text{A}$ . Above this current levels, find a linear current-voltage characteristics resembling the series resistance of the setup. Furthermore, we observe a hysteretic behavior as indicated by gray arrows. Panel b) displays the switching current  $I_s$  of the SQUID for pad 2 and 7 as function of the externally applied magnetic field. Measured data is shown as dark points, fitting curves are indicated in blue for pad 7 and red for pad 2 using Eq. (2.36). The designed junction size was  $0.18$  (pad 7) and  $0.09 \mu\text{m}^2$  (pad 2) per junction, so a current density of  $2.8$  (pad 7) and  $3.1$  (pad 2)  $\mu\text{A}/\mu\text{m}^2$  was reached.

current voltage characteristics indicating an ohmic behavior which is attributed to the serial resistor of  $230 \Omega$ . In addition we find a hysteresis when ramping the bias current down again, indicating our junctions are underdamped. We discussed this theoretically in Sec. 2.2.1. Besides the particular dc-SQUID shown here, we investigated a whole series of SQUIDs with identical design parameter, except half of them with Josephson junctions half the size of the particular dc-SQUID in order to determine critical current per junction size, hence be able to set the desired critical current by designing the junction area. The data of all measured SQUIDs are summarized in Tab. 4.1 and discussed later.

Please note, that it is not possible to extract the critical current of the junction  $I_c$  directly from this current-voltage characteristic. This information can only be deduced from the analysis of the switching current  $I_s(B)$  as function of the magnetic field dependent as discussed in the following.

### 4.2.2 The critical current of dc-SQUIDs

To determine the magnetic field dependence of the critical current we sweep the current source until a voltage drop appears. This switching current is recorded and averaged until a new specific current through a coil, which sets  $B_{\text{coil}}$ , is applied.

For the analysis of the critical current of two selected dc-SQUIDs with differing junction areas we plot the switching current  $I_s$  as function of the externally applied magnetic flux as shown in Fig. 4.6 b). Contrary to the ideally, expected  $|\cos(x)|$  behavior (see Eq. (2.36)) we observe smoothed edges for all  $\Phi_{\text{ext}} = (n + 1/2)\Phi_0$ . This deviation is attributed to asymmetries in the junction area or from the detection setup, since either the cut-off voltage, which is the limit that has to be exceeded to detect the switching current, could have been set wrong or an offset voltage from, e.g. the multimeters and amplifiers used in the setup, was not calibrated out. Large screening factors  $\beta_L$  also lead to a nonvanishing minimum when downtuning the critical current [33]. But here this can be excluded since in that case the edges at the minimum switching currents are sharp, not blurred out [38].

### 4.2.3 Comparison Si vs. $\text{Si}_3\text{N}_4$ substrates

So far we discussed the maximal critical current, the gap voltage and the normal resistivity of the fabricated dc-SQUIDs. For our mechanics,  $\text{Si}_3\text{N}_4$  is used as substrate layer as it provides the high tensile stress required for high Q mechanics. In the previous section we have seen that it is possible to fabricate operating SQUIDs on high stress  $\text{Si}_3\text{N}_4$  layers, next we compare the characteristics of such SQUIDs with SQUIDs fabricated on the standard substrate material silicon.

To this end, we fabricated two chips with SQUIDs including contact lines on the two substrates, Si and  $\text{Si}/\text{Si}_3\text{N}_4$ . We used the fabrication process described in Sec. 3.1 with identical parameters for both samples, in particular oxidation time of 800 s, an  $\text{O}_2$  flow of

Si <sub>3</sub> N <sub>4</sub> pad	$V_g$ ( $\mu$ V)	$R_n$ ( $\Omega$ )	$A_{JJ}$ ( $\mu$ m <sup>2</sup> )	$I_\Sigma$ (nA)	$d$ (%)	A-B-R
2	368	522	0.09	549	13.9	0.99
3	369	682	0.09	373	21.6	0.88
6	365	230	0.18	997	16.5	0.80
7	367	241	0.18	996	28.0	0.83
Si pad						
3	356	176	0.18	1270	11.0	0.80
6	379	548	0.09	474	14.4	0.87
7	355	404	0.09	576	11.0	0.83

**Table 4.1:** Results of SQUID performances on Si and Si<sub>3</sub>N<sub>4</sub> substrates (chips: SiSquid2 and SiNSquid8). Designed Josephson junction size  $A_{JJ}$  was set to either  $0.9 \mu\text{m}^2$  or  $1.8 \mu\text{m}^2$ . Gap voltage  $V_g$  and normal resistivity  $R_n$  were measured by U-I curves, critical current  $I_\Sigma$  and modulation depth lessen factor  $d$  by  $I_s(B)$  curves. Deviations between the substrates are in the size of them in each substrate itself. The desired critical current in the  $\mu\text{A}$  regime was accomplished for large junction areas. A lessen factor of up to 28% was reached. Further we calculated the Ambegaokar-Baratoff relation as described in the text.

5 sccm at a valve position of 45%. Further the aluminum deposited with an evaporation rate of with 1 nm /s under an angle of  $\pm 17^\circ$  with layer thicknesses of 40 and 70 nm. The junction sizes are determined a posteriori using the SEM.

Figure 4.7 compares the measured critical current  $I_c$  as a function of the junction size for several SQUIDs on both chips (SiSquid2 and SiNSquid8).

A linear dependence in the form  $I_c[\mu\text{A}] = (2.56 \pm 0.29) \cdot A_{JJ}[\mu\text{m}^2] + (0.004 \pm 0.043)$  is observed. Note that the expected intersection with the origin is observed within the error margins. The junction area on Si turned out larger than on Si<sub>3</sub>N<sub>4</sub> because the resist exposure dose was optimized for silicon nitride. On silicon this overexposure results in blurry edges thus larger junctions. All in all Fig. 4.7 shows that the fabrication parameters have to be optimized separately for different substrates, nevertheless fabrication of well operating dc-SQUIDs on SiN substrates is achieved, which is an important step in realizing the nano-electromechanical device discussed in this thesis.

A further indication for this is shown in Table 4.1 were we collected our data and calculated the *Ambegaokar-Baratoff relation* (A-B-R)  $4I_\Sigma R_n / (\pi V_g)$  [54], describing how close the SQUIDs have reached the theoretical maximum critical current in a microscopic description based on Cooper pair tunneling processes. The closer this to one, the closer the critical current has reached the theoretical limit. As we can see our SQUIDs are well optimized providing the high critical currents we need. Further it deviates in the same range on both substrates, so we conclude no correlation between the A-B-R factor and the substrates.

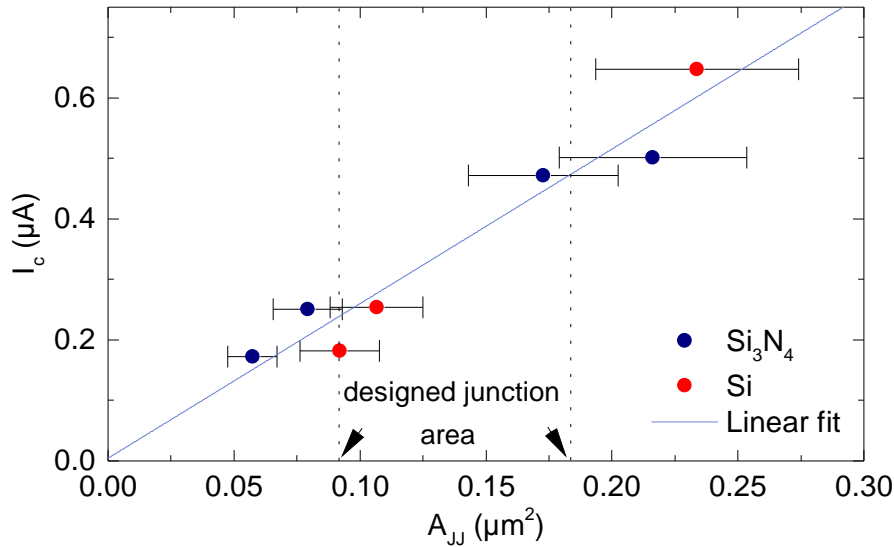


**Figure 4.7:** Comparison of SQUIDS on silicon (red, SiSquid 2) and silicon nitride (dark blue, SiNSquid 8) substrates. Both chips were fabricated with same parameters. Critical current and junction area are directly proportional within the measurement uncertainties (bright blue line). The uncertainties in the junction area are estimated from the SEM images. The designed junction areas are marked by dotted lines. Deviations from the designed area come from fabrication imperfections. The silicon junctions are larger than designed due to overexposure during the EBL step.

### 4.3 Superconducting microwave resonators

As last constituent of the electro-mechanical device we concentrate on the niobium CPW resonators. Those are the backbones of our system since in the final electromechanical hybrid system every experiment later is based on the transmission characteristics of the MW resonator. So they are very important for our signal strength in the end. The design criteria in this regards are:

- Can we predict the resonance frequencies for a given geometry? First, predicting the correct frequency eases the initial microwave spectroscopy and to identify the corresponding resonator with its location on the chip. Second, for optimal electromechanical coupling, we require a steep transfer function with the applied magnetic flux. As this steep region is located typically at frequencies significantly lower than the maximum frequency of the resonator, we will aim for designing resonators with frequencies as high as possible with respect to the microwave detection circuitry.

- What quality factors can be achieved? For the resolved sideband regime aim for low total linewidths  $\Gamma$ . This linewidth consists of an internal and an external quality factor. For optimized signal extraction from the microwave resonator we will optimize for large coupling capacitances or a good coupling between the microwave resonator and the feedline. In turn, higher capacitive couplings result in a broadening of the linewidth  $\Gamma$ . Thus we need to optimize this capacitive, coupling for maintaining the resolved sideband regime taking also the internal loss mechanisms of the microwave resonator into account.
- How does the  $\text{Si}_3\text{N}_4$  pad influence the resonator? Silicon nitride has a lower dielectric constant compared to silicon. As shown it increases the resonance frequency and quality factor of the mechanical oscillator hence the influence of it to the microwave resonator has to be studied.

For the initial microwave spectroscopy on the microwave resonators we use the 1.5 K cryostat as described in Sec. 3.2.2 in combination with a Hewlett Packard *HP 8772* vector network analyzer.

We fabricated superconducting CPW resonators with niobium on silicon as explained in Sec. 3.1 capacitively coupled to a transmission line. All resonator lines have a width of  $12\ \mu\text{m}$  and a gap of  $6\ \mu\text{m}$  to the ground plane resembling a line impedance of  $Z_0 = 50\ \Omega$ . An overview of a typical chip is shown in Fig. 4.8 a). The chips have  $\lambda/4$  and  $\lambda/2$  resonators on it. Also the coupling capacitance is varied by different distances to the feed-line (see Fig. 4.8 b)).

In particular, we focus on two samples. SiRes18 consists of 4  $\lambda/4$  and 4  $\lambda/2$  resonators. The  $\lambda/2$  were produced by cutting off the connection between the ground plane and the resonator as depicted in Fig. 4.8 c). This transforms the  $\lambda/4$  resonators to  $\lambda/2$  with doubled resonance frequency. The coupling distance on this chip is  $60\ \mu\text{m}$ . In contrast SiNRes4 has 8  $\lambda/4$  resonators with a coupling distance of  $50\ \mu\text{m}$ . Further we placed a SiN pad below the niobium at the anti-node to model the situation with the later included SQUID (see Fig. 4.8 d)).

Figure 4.9 shows transmission data  $S_{21}^2$  of the chips SiRes18 and SiNRes4 as function of the stimulus frequency. Panel a) the transmission  $|S_{21}|$  of sample SiRes18 is depicted as function of the MW frequency. For clarity we divided the frequency of the  $\lambda/2$  resonators by two.

Six of the eight resonators are observed as, sharp dip of typically 3 dB depth in the transmission spectrum. When plotting the data from the  $\lambda/2$  and the  $\lambda/4$  resonators (frequency corrected) in the same datagraph, it turns out that the  $\lambda/2$  resonances are slightly below the  $\lambda/4$  ones as indicated in Fig. 4.9 a) with a black arrow. This is attributed to two effects. First, as we simply cut out some space for the SQUID as depicted in Fig. 4.8 c)

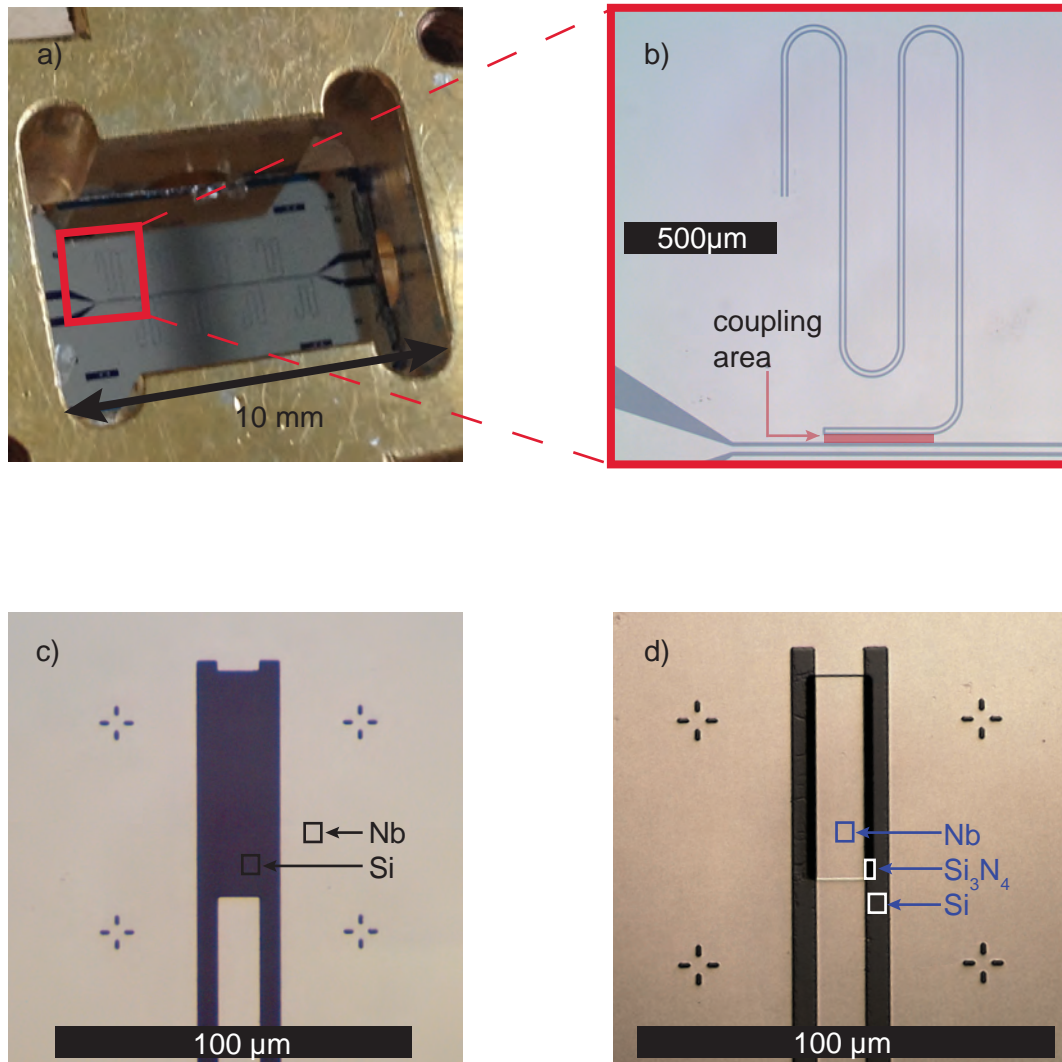


**Figure 4.8:** Fabricated MW resonator chips and details. a) Sample SiRes18 mounted in gold plated copper box. Chip size  $10 \times 6 \text{ mm}^2$ . b) Antenna, feed-line and  $\lambda/4$  resonator in detail. The coupling capacity is given by the length (which was kept the same on all resonator) and the distance between the feed-line (here  $60 \mu\text{m}$ ) c) Anti-node of one of the  $\lambda/2$  resonators of sample SiRes18. The place for the SQUID is cut out, transforming the  $\lambda/4$  to a  $\lambda/2$  resonator with doubled resonance frequency. d) Anti-node of a resonator from sample SiNRes4. Here a  $\text{Si}_3\text{N}_4$  pad was placed below the niobium to study its effects on the resonator.

the two center conductors do not exactly differ by a factor of two. Second the realization of our capacitive coupling of the feedline to the resonator reduces the wavelength to an effective value. The coupling area (colored in red in Fig. 4.8 b)) is spread over a certain

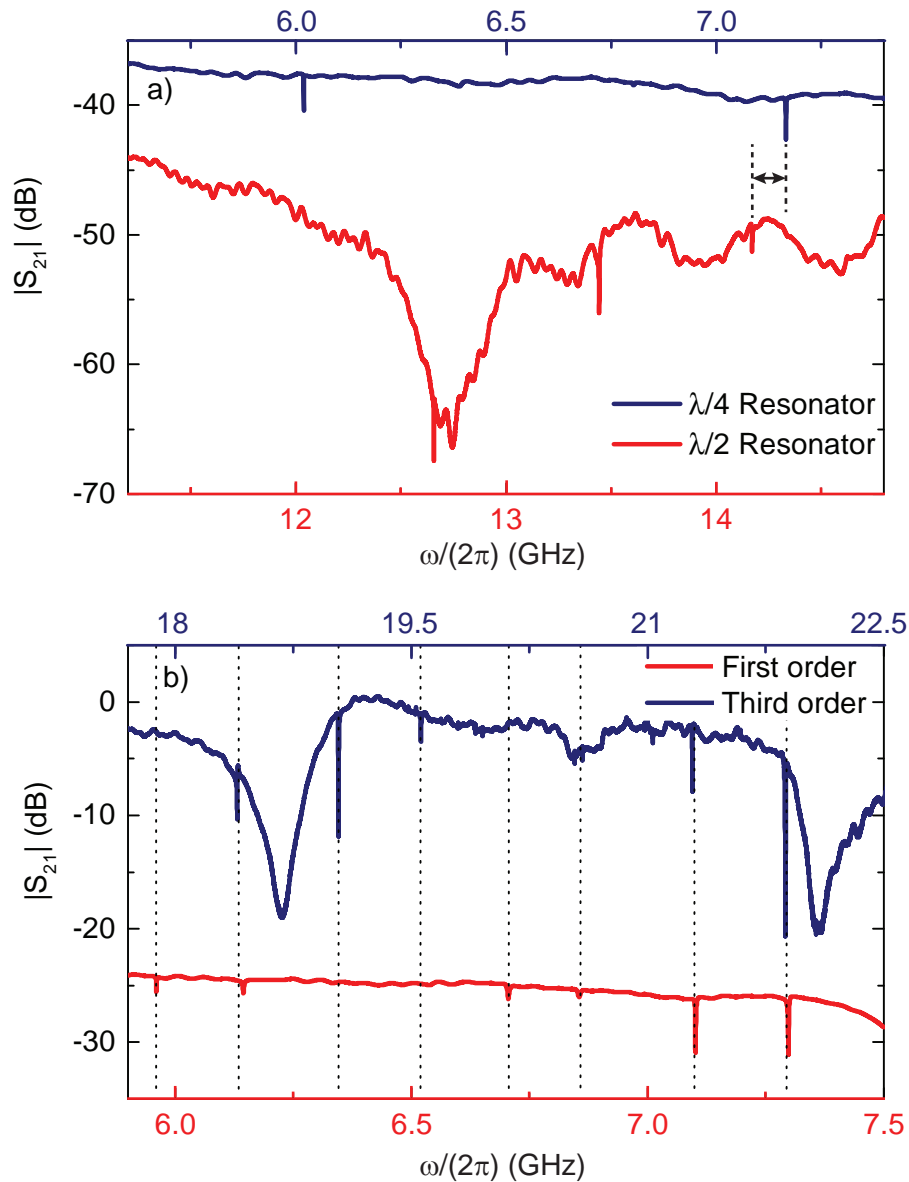


**Figure 4.9:** Uncalibrated microwave transmission of samples SiRes18 and SiNRes4 at 1.5 K. a) Sample SiRes8. Resonance dips with a depth of 3 dB are found at frequencies of 6.02, 6.80, 7.17 GHz for the  $\lambda/4$  and 12.66, 13.44, 14.16 GHz for  $\lambda/2$  resonators. So three of four resonators of each kind are working. While the  $\lambda/4$  resonators do not differ from the designed  $(6.0 + 0.4 \cdot n)$  GHz frequencies, the  $\lambda/2$  resonators appear slightly below these design frequencies. This becomes more obvious when plotting  $\omega/(4\pi)$  as shown in the graph, e.g. looking at the highest resonances 7.17 GHz and 14.16 GHz here corresponding to 7.08 GHz one sees the spacing between of 90 MHz, as indicated. Panel b) Sample SiNRes4, the figure displays the transmission data of the microwave resonators fundamental mode as well as data taken on the third harmonic. The latter are squeezed by a factor of 3 in frequency for easy comparison with the fundamental mode. For clarity, we have shifted the third order by 20 dB. Dip depths of up to 15 dB are observed for the fundamental mode of the resonators. Using the higher harmonics we were able to reconstruct all 8 resonance frequencies, but contrary to the design, the distance between the resonances are not equidistant.

length of the resonator, hence the node of the microwave is somewhere in this area. So the effective wavelength is reduced. Please note, that these systematic deviations are below 2% so the designed resonance frequency matches the measurements quite well. Detailed analysis of this behavior can be done with finite element simulations, but they do not appear necessary here.

Figure 4.8 b) shows the transmission of sample SiNRes4 for the base frequency and the third harmonic frequency corrected by a factor of three and shifted by 20 dB on the vertical axis for clarity.

We were able to determine all resonance frequencies between 6.0 GHz and 7.4 GHz by analyzing ground and third harmonics of the chip. This is indicated by stroked lines in the figure. In contrast to the ones from sample SiRes18 the separation between those resonances is not equidistant as it is expected from the design. This might come from the Nb pad (shown in Fig. 4.8 d)) we placed at the short to the ground plane. We will detailed discuss its influence later.

The next step is to analyze the resonators eigenfrequencies in more detail. Therefore, we take calibrated data resolving the microwave resonator's response in higher resolution. For the data analysis, we compare two models. The first one was derived in Ref. [21], in conclusion the resonance is fitted as a Lorentzian lineshape with a complex background, as we have seen it before, e.g. in Sec. 4.1. The alternative approach follows Ref. [31]. As demonstration we have depicted the resonance at 7.3 GHz of sample SiNRes4 in Fig. 4.10. Panel a) and b) show the transmission and phase of  $S_{21}$  while c) shows imaginary over real part of  $\check{S}_{21}^{-1}$ . Using this representation, the ideal situation is that the transmission of the resonance performs a circle tangential to 1 centered at  $M$ . The diameter of this circle  $D$  is given by  $Q_i/Q_c^*$  with the internal quality factor  $Q_i$ , the rescaled coupling quality factor  $Q_c^* := (Z_0/|Z|)Q_c$ , and the external quality factor  $Q_c$ . We further define the characteristic impedance  $Z_0 = 50 \Omega$ , the magnitude of the complex impedance  $Z = |Z|\exp(i\phi)$  and  $\delta\omega = (\omega - \omega_0)/\omega_0$ . Typically, for a realistic situation, the circle is rotated by an angle  $\phi$  as depicted in Fig. 4.10 c) describing complex background signals as shown in Sec. 2.1.5. Additionally, we can deduce  $\Gamma$  from this plot. It is found at the point where the bisector perpendicular to  $(1, M)$  reaches the circle.

For this fitting procedure, the inverse of the calibrated scattering matrix  $\check{S}_{21}$  is analyzed. To be specific, we take the aquired data

$$\check{S}_{21}(\omega) = \text{Re}[\check{S}_{21}(\omega)] + i \cdot \text{Im}[\check{S}_{21}(\omega)], \quad (4.8)$$

see Fig. 4.10 a and b)) and calculate its inverse. This quantity is plotted in the complex plane, as depicted in Fig. 4.10 c). We then fit to this curve the expression [31]

$$\check{S}_{21}^{-1} = 1 + \frac{Q_i}{Q_c^*} e^{i\phi} \frac{1}{1 + i2Q_i\delta\omega}. \quad (4.9)$$

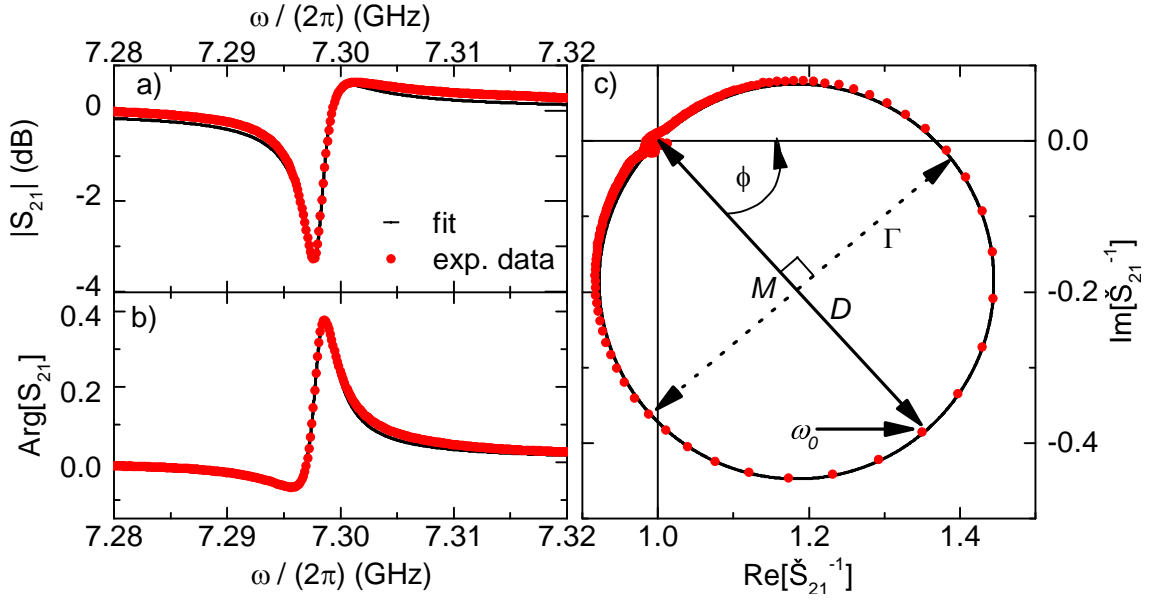


**Figure 4.10:** Resonance 8 from sample SiNRes4 in detail: a) Peak transmission and b) peak phase as well as c) the peak in the complex plane by plotting  $\check{S}_{21}^{-1}$ . Experimental data are shown in red, while the fit with Eq. (4.9) is black. A typical Lorentzian shaped dip of about 4 dB with some complex background is found for the transmission. Instead of a phase change we see a fano-like peak structure. The resonance circle is round and fits the theoretic description.

The respective fit is plotted as black lines in Fig. 4.10. This method has the advantage that both transmission and phase are fit simultaneously, thus we get internal and external quality factors without numerical simulations.

The fit returned a resonance frequency  $\omega_0/(2\pi) = 7.297$  GHz, a rotation angle  $\phi = -0.689$  rad. The total quality factor  $Q_{\text{tot}} = 2.69 \cdot 10^3$  is determined by an internal quality of  $Q_i = 3.88 \cdot 10^3$  and external quality of  $Q_c = 8.78 \cdot 10^3$ . The corresponding Lorentzian fit with complex background returned  $Q_{\text{Lorentz}} = 2.85 \cdot 10^3$ . So both fit procedure differ slightly by 6%. As mentioned above, in the fitting model for  $\check{S}_{21}^{-1}$  both, the resonance dip of about 3 dB in the transmission as well as the fano-like peak curve of the phase are automatically included.

We fitted all resonances in this way. To be able to compare it with the Lorentzian fit with complex background we also fit the data with this method.

We summarized the results of both fitting procedures in table 4.2. To compare the quality factors we plotted the total quality of the complex fit  $Q_{\text{tot}}^{-1} = Q_i^{-1} + Q_c^{-1}$  and the quality factor from the Lorentzian fit  $Q_{\text{Lorentz}}$  over the resonance frequencies in Fig. 4.11 a).

We found quality factors from one to eight thousand. This fits since later with the SQUID similar values are accessible [55].

All in all the with the two methods obtained Q factors give the same results, we underline that the analysis using Eq. 4.9 allows a full extraction of the data

SiNRes4	$\omega_0/(2\pi)$ (GHz)	$Q_i/1000$	$Q_c/1000$	$Q_{tot}/1000$	$\phi$ in rad	$Q_{Lorentz}/1000$
	5.96	4.04	28.4	3.54	0.926	4.05
	6.14	1.64	14.2	1.47	0.562	1.38
	6.70	2.67	19.7	1.87	0.389	1.72
	6.85	1.42	22.8	1.34	0.364	1.39
	7.10	4.34	8.72	2.90	-0.265	3.13
	7.30	3.88	8.78	2.69	-0.689	2.85
<hr/>						
SiRes18						
	6.02	9.47	50.2	7.96	-4.14	11.4
	6.80	1.37	63.2	1.34	-4.53	2.15
	7.17	4.20	23.9	3.57	-3.93	4.94

**Table 4.2:** Comparison of fit procedures. Resonance frequencies from 6 to 7.4 GHz were found. Both fits returned similar eigenfrequencies, here shown are the ones from the complex fit. Next internal, external and total quality factors obtained by the complex method are shown, the total quality ranging from 1000 to 8000 is found. Next the rotation angle in rad is depicted. It shows no general dependency. Last the total quality obtained by Lorentzian fits are collected. In comparison to the ones from the complex fits one notices no big deviations on sample SiNRes4 but on sample SiRes18 it does.

In Sec. 4.1 we saw that the eigenfrequency of a mechanical resonator has a reciprocal dependency to its length. Here for MW resonators we can observe an analogue behavior since [56]:

$$\frac{\omega_0}{2\pi} = \frac{v_{\text{phase}}}{l_{\mu\text{wave}}} = \frac{c}{\sqrt{\epsilon_{\text{eff}}}} \frac{1}{l_{\mu\text{wave}}} \quad (4.10)$$

analog to the mechanical resonators the phase velocity  $v_{\text{phase}}$  and the length of the fundamental mode  $l_{\mu\text{wave}}$  determines the resonance frequency. Here the phase velocity depends on the speed of light in vacuum  $c$  and the effective field constant  $\epsilon_{\text{eff}}$ . So this allows us to study the effective field constant of our samples.

The dielectric constant of silicon is 11.9. Silicon nitride in contrast has 7.5 [57], so by adding the silicon nitride patch we expect a slightly lower  $\epsilon_{\text{eff}}$ . An exact appraisal is not straightforward with this sample design since the ratio of the pad length to the resonator length is not constant per chip since it was designed for investigating coupling strengths in the end. Nevertheless if there is a large influence we should notice a reduction in the effective field constant.

We plotted our experimental results in Fig. 4.11 b). Resonance frequencies from 6.0 to 7.5 GHz are shown over microwave resonator length of 16 to 20 mm. The resonance

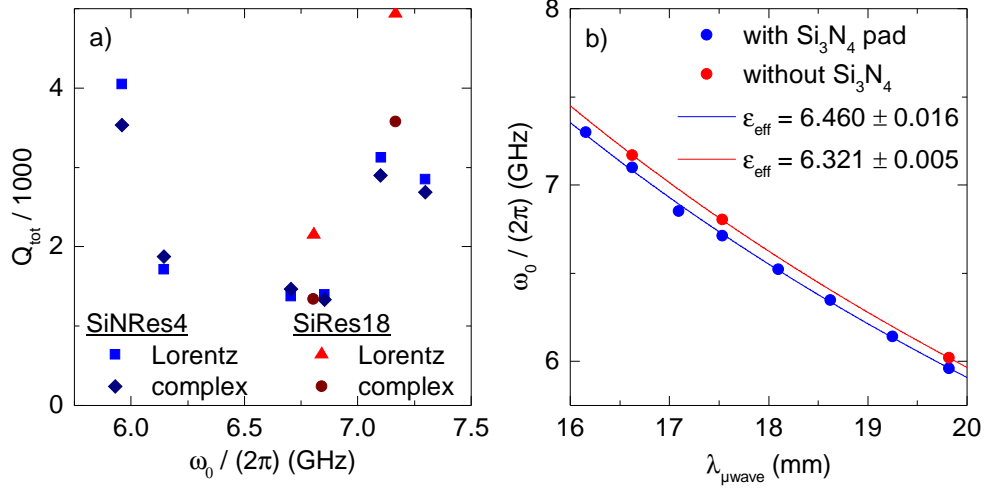


**Figure 4.11:** Details on the fabricated MW resonators. a) Comparison of both fit procedures by plotting the total quality factor  $Q_{\text{tot}}$  for each resonance frequency  $\omega_0$ . Sample SiNRes4 (8  $\lambda/4$  with Si<sub>3</sub>N<sub>4</sub> pads) is shown in blue while SiRes18 (4 $\lambda/4$  on pure Si) is kept red b) Analysis of effective dielectric constants again SiNRes4 with silicon nitride pad (blue dots) and SiRes18 without (red dots) by plotting frequencies from 6.0 to 7.5 GHz over resonator wavelengths of 16 to 20 mm. On pure silicon higher frequencies are observed for all resonator lengths. Fitted reciprocal behavior is shown in lines with respective colors returning  $\epsilon_{\text{eff, w}} = 6.460 \pm 0.016$  and  $\epsilon_{\text{eff, w/o}} = 6.321 \pm 0.005$ . Error bars include statistical uncertainties only.

frequencies of the sample SiNRes4 with silicon nitride patches is shown as blue dots while the resonance frequencies of SiRes18 fabricated on pure silicon are shown as red dots. Fits by Eq. (4.10) are shown as solid lines in respective colors. For all resonator lengths the eigenfrequencies on pure silicon are above those with pad, indicating a slightly lower dielectric constant. The corresponding fits return  $\epsilon_{\text{eff, w}} = 6.460 \pm 0.016$  and  $\epsilon_{\text{eff, w/o}} = 6.321 \pm 0.005$ . The error bars contain only statistical uncertainties. Systematical deviations may come from the coupling to the chip, e.g. by some oxide layers or a bad silver glue contact. All in all this fits the expected dielectric constant for Si-vacuum interface, since [58]:

$$\epsilon_{\text{eff, Si-vac}} = \frac{\epsilon_{\text{eff, Si}} + \epsilon_{\text{eff, vac}}}{2} = 6.45 \quad (4.11)$$

where we used  $\epsilon_{\text{eff, Si}} = 11.9$  [57].

In contrast to the expectation, we observe a higher effective dielectric constant with the silicon nitride patch present. This indicates that the influence of our 100  $\mu\text{m}$  long pad at the voltage node of a millimeter sized MW resonator is vanishing and because of that has a neglectable influence on the resonance eigenfrequency. As the predicted resonance frequencies match the experimentally detected ones well, we will neglect the slight influence of the SiN patch for our models in the future as our prediction accuracy is

within several linewidth of the resonator.

We would propose highly overcoupled resonators, so environment effects become less important.

In conclusion we are now able to predict the resonance frequencies of our CPW resonators and the microwave resonator quality factors are sufficient for reaching the resolved sideband limit in the envisaged optomechanical hybrid system.

## 4.4 Flux tunable microwave resonators

As a next step towards an inductive coupling between a mechanical and a MW resonator we placed SQUIDs at the current anti-nodes of  $\lambda/4$  CPW MW resonators as sketched in Fig. 3.6 a). The resonator is fabricated on a silicon substrate while the SQUID was built on a silicon nitride pad to allow for fabricating a high Q nano-mechanical resonator. The complete chips were mounted in a gold plated oxygen free high conductance (OFHC) copper box with a superconducting coil attached to it. In this section we aim addressing the following points:

- Can we fabricate and characterize  $\lambda/4$  MW resonators shunted to ground with a dc-SQUID? How does the presence of the SQUID influence the MW resonator's frequency and linewidth? One crucial point might be the aluminum niobium contact due to oxide formation at the niobium surface. Is the designed contact area between Al and Nb sufficiently large or in other words is the resistance of this junction sufficiently low to provide the desired shunting ?
- Is the resonance frequency flux-tunable over a the calculated range?
- What electromechanical coupling strengths can we deduce from this flux tunable device? For the coupling require the slope, thus we need to measure  $\omega_0(B)$ . Moreover, the linewidth is an additional very important quantity which we like to monitor in this experiment, since we eventually aim for operating the device in the resolved sideband regime.
- The SQUID adds a nonlinear elements in the form of Josephson inductance to the MW resonator. Is this observable in experiment? As this nonlinearity is flux tuneable, we will analyze this behavior in the following

As the SQUID element is naturally sensitive to flux and flux noise stemming from the outside of the experimental setup, we fabricated a further shielding in form of a cylinder with a bottom plate consisting of 99.5% superconducting Al to decrease the field noise present at the chip. Further  $\lambda/4$  resonators coupled to a transmission line had to be measured, leading to low signal depth in comparison to  $\lambda/2$  ones in reflection. We further use a dilution fridge for these experiments since this setup allows for continuous microwave measurements in a temperature environment below the critical temperature of aluminum. In the following we discuss chip SiNRes 15 containing the two tunable resonators Res 1 and Res 2 with the resonance frequencies of  $\omega_{0,1}/(2\pi) = 7.4$  GHz and  $\omega_{0,2}/(2\pi) = 6.2$  GHz with SQUID loop areas of  $A_1 = 90 \mu\text{m}^2$  and  $A_2 = 150 \mu\text{m}^2$ , respectively. Both SQUIDs were designed for a critical current of  $0.5 \mu\text{A}$ .

As experimental setup we used the dilution refrigerator "Kermit" introduced in Sec. 3.2.4. Electric wiring and shielding is depicted in Fig. 3.13.

### 4.4.1 Spectroscopy of the SQUID microwave resonator hybrids

We now look at the spectroscopy data of the two SQUID shunted microwave resonators which are coupled capacitively to a transmission feedline. Figure 4.12 a) shows the transmission spectroscopy data for the feedline recorded for a microwave power of  $-120$  dBm applied to the sample box. Please note, that panel a) shows a differential transmission, that is we have measured a reference transmission dataset for a magnetic field of  $0$  mT and  $4.42$  mT which is cut together free of resonances and then subtracted the full two-dimensional dataset. Hereby, we obtain a quasi-calibrated dataset highlighting the evolution of the resonance frequencies as function of the applied magnetic fields. Please note that we can identify two microwave resonators in the investigated spectroscopy windows with a maximum resonance frequency of  $5.8$  GHz (Res1) and a second one with a maximum frequency of  $4.7$  GHz (Res 2). They both show the characteristic behavior of a SQUID shunted microwave resonator as discussed in Sec. 4.12. Note that as the two SQUIDS have differing loop areas, the evolution of the resonance frequency shows different periodicity in the magnetic field direction.

The original raw data of this panel a) was initially measured as function of the applied coil current bias. For a quantitative analysis of the inductive electromechanical, we require a calibration of the coils transfer function, as we are finally interested in the impact of the mechanically induced flux change through the SQUID loops. This calibration is obtained by analyzing the periodicity of the microwave resonator response as shown in Fig. 4.12 c). In particular, we start by investigating the frequency window between  $4.82$  and  $4.88$  GHz, here recorded for a coil current from  $-1$  mA to  $+1$  mA. In this window, we find six maxima of the microwave resonators frequency from Res2. So six equidistantly spaced spikes on the bias current axis are found. In the same panel we also find four appearances of the decreasing frequency branch from Res1. We further note, that these periodic repetition of the microwave resonator frequency behavior with the coil's current bias  $I_{\text{coil}}$  is attributed to the periodicity of the SQUID response, thus we expect for both to follow a periodicity in  $\Phi_0$ . Thus we can use this periodicity to deduce the linear conversion factor between the coil current and the local magnetic field at the respective SQUID loop above follows:

$$\Delta\Phi = \Delta B \cdot A_i = \gamma_I \Delta I A_i \stackrel{!}{=} \Phi_0 \Rightarrow \gamma_I = \frac{\Phi_0}{\Delta I A_i}. \quad (4.12)$$

Thus, for Res2 with a periodicity in  $I_{\text{coil}}$  of  $\Delta I = 300 \mu\text{A}$  and a SQUID loop area  $A_2 = 150 \mu\text{m}^2$ , we obtain a calibration factor of  $\gamma_1 = 44.44$  mT/A was found. Doing the same for Res1 with  $A_1 = 90 \mu\text{m}^2$  and  $\Delta I = 506 \mu\text{A}$  we find  $\gamma_2 = 43.94$  mT/A. These two values are well compatible and slight deviations can be attributed to the different locations of the respective SQUID loops on the chip. In summary, we use the averaged conversion factor  $\gamma_I = 44.19$  mT/A for calibrating the magnetic field axis in panel a).

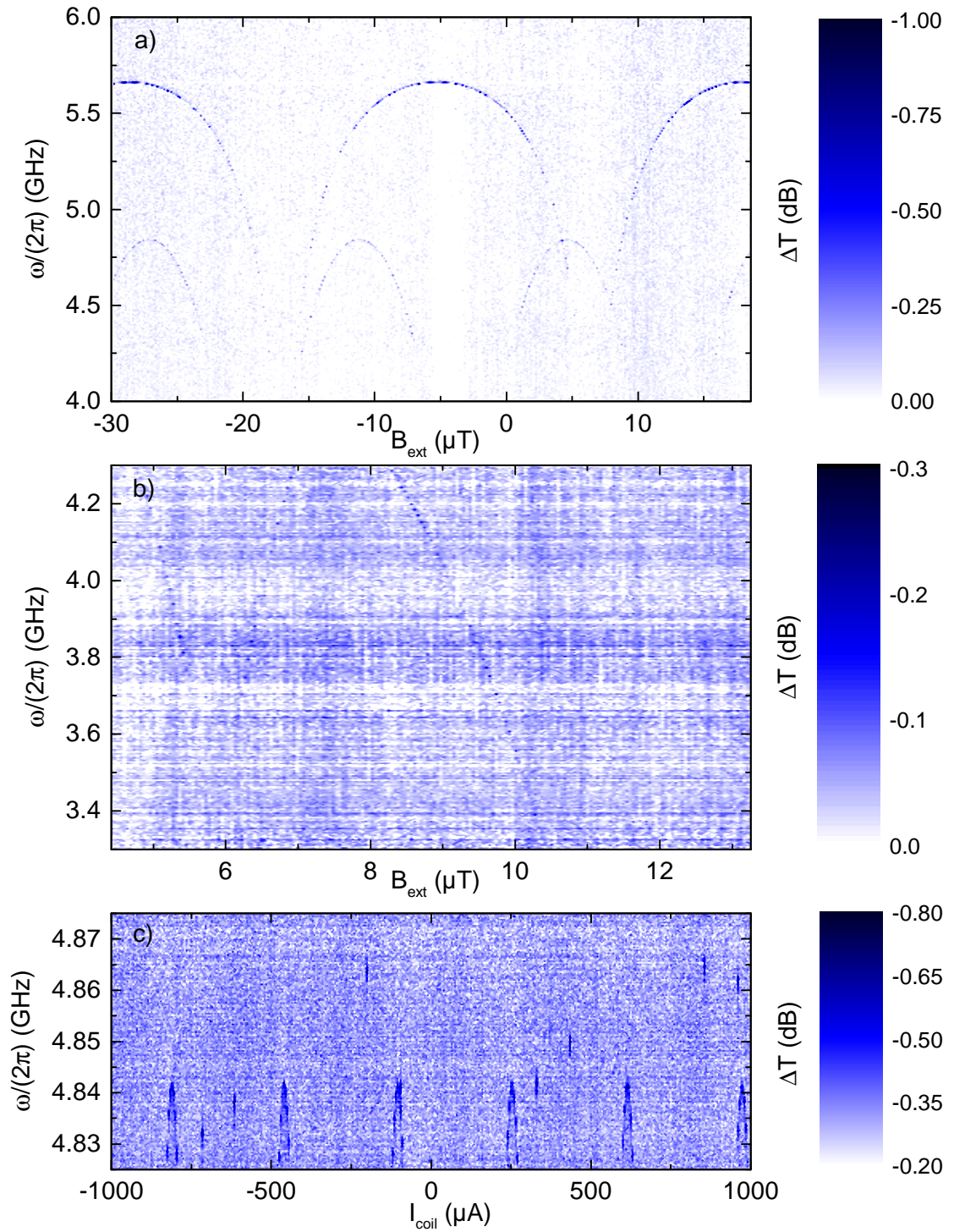


**Figure 4.12:** Magnetic flux sweeps on  $\lambda/4$  resonators with SQUIDs. a) Overview spectra, two resonators were found with maximal frequencies of 5.65 (R1) and 4.85 GHz (R2). b): Detailed zoom for steep slopes. Tunabilities of  $59.5 \text{ GHz}/\Phi_0$  (R1) and  $19.0 \text{ GHz}/\Phi_0$  (R2) were observed at  $\omega_0/(2\pi)$ . c) Coil calibration via SQUID's area sizes. To increase accuracy we took a large number of periods.

To deduce from this data the electromechanical coupling, we investigate in more detail the region with a steep slope in the microwave resonator frequency dependence of Res 1 (shown in Fig. 4.12 b)) around  $B_{\text{ext}} = 9 \mu\text{T}$ . Here  $|\partial\omega_0/(\partial B_{\text{ext}})|$  is large for both resonators. Here on the left at about  $6 \mu\text{T}$  Res 1 tunes down. One can see both sides of the downtuning. In the middle the left branch of Res 2 tunes down with a lower slope than Res 1. Both resonators show a maximum signal depth of 0.3 dB. Note that the resonator with the lower  $\partial\omega(B)/\partial B$  is easier to observe in the dataset shown in Fig. 4.12 b) as a much larger number of points is visible in the shown frequency window, for a better observation we have attached Fig. 4.12 b) and c) with indications where to find the resonators in Appendix B. From the experimental data we extract a slope of the  $\omega_0(\Phi)$  curve of  $59.5 \text{ GHz}/\Phi_0$  (Res 1) and  $19.0 \text{ GHz}/\Phi_0$  (Res 2) at 3.3 GHz.

As indicated in Sec. 2.4 the maximal achievable inductively electromechanical coupling scales with  $\partial\omega_0/\partial B \times B$ . Thus, high applied fields further improve the coupling strength. To this end at the end of the measurement run the critical field or maximal applicable magnetic field is investigated. The limiting factor here are the superconducting properties of aluminum with a critical field of 10.4 mT in bulk [27]. The niobium forming the basis for the microwave resonators, has a much higher critical field of 206 mT thus it is not expected to limit the system [27]. Because of the use of thin films and local field enhancement due to shape factors the critical field we expect is lower than that reported for bulk of Al [37]. To measure the critical field the coil current  $I_{\text{coil}}$  was increased while observing the characteristic properties of the microwave resonator Res1. At 2.2 mT the quality factor of the resonator dropped abruptly and irreversibly by a factor of about 20. A detailed dependency of the resonators linewidth with the magnetic field was not possible due to this abrupt change. So we use 1 mT as upper limit for further calculations since we saw no change of the resonator's state at that level. The detailed influence of the magnetic field will be an important aspect for future experiments as pushing to higher electromechanical couplings is desired. Nevertheless, 1 mT provides already a factor of 100 boost compared to operating the device at the regime displayed in Fig. 4.12 a).

#### 4.4.2 Flux tunable resonators - an analysis of their performance

Up to now we have only coarsely investigated the MW resonators' frequency dependence as function of the applied magnetic field. For a more thorough analysis, in particular for an analysis of the MW resonator q-factor, we require a significant (more than 20) points within resonators resonant response. To keep the hereby tremendous demands on measurement time at balance, we approximated the resonator's frequency evolution using our overview spectra and scanned only in a range of 150 MHz around this center frequency in order not to lose the resonance. Note that even this enormous reduction in measured datapoints still extends the measuring time for each displayed scan to more

than 24 hours because to sweep over a broad magnetic field interval is desirable. Further the dip size was small compared to background noise, so we had to use a low bandwidth also increasing the measuring time.

To fit our frequency dependent transmission data we followed the approach outlined in Sec. 2.3 and Ref. [21] where the transmission of a  $\lambda/4$  resonator is fitted to a Lorentzian lineshape with complex background, see Eq. 4.3. The latter comes from parasitic paths in our resonator geometry, see Sec. 2.1.5, and fits well our observations as shown later more in detail. From these fits we obtain the resonators eigenfrequencies depending on  $B$   $\omega_0(B)$  and the corresponding linewidths  $\Gamma(B)$ . This is depicted in Fig. 4.13 a) for Res 1. Here, in blue the resonance frequency tuning is shown in a range from 4.0 to 5.6 GHz. Qualitatively it follows the predicted behavior from Fig. 2.9 b) and as seen in the overview spectrum in Fig. 4.12 a). The magnetic field range of  $40 \mu\text{T}$  corresponds to about one and a half periods. Some frequency points are missing since there the approximated resonator tuning differed from the reality. This happened since the approximation was done very roughly and the frequency range had to be kept narrow to achieve a sufficient signal to noise ratio.

In red, the linewidth to the respective resonance frequencies are plotted. As one can see from the corresponding red scale on the right on the frequency maximum a linewidth  $\Gamma/(2\pi)$  between 1.5 and 2.5 MHz is found. This is in good agreement with the 2.0 MHz found in Fig. 4.14 a) and b), which most likely comes from noise fluctuations. As one can see in resonance in a) the datapoints are fluctuating around the fit curve, while in b) these deviations from the fit are much smaller leading to a smaller  $\Gamma$ .

We generally observe a trend, where large slopes or  $\partial\omega_0/\partial B$  result in larger measured resonance linewidths. This is attributed to the effect, that the resonator is more sensitive to the applied magnetic field, so even small changes in the magnetic field produce a change in the resonator's eigenfrequency. Then the signal is averaged over some field points resolving in a broader and flatter peak feature. One can say that at this point our magnetic shielding has reached its maximum performance. Additional, we want to note that the current source might also contribute to the fluctuations. For a further decrease in field noise to reach stepper and so larger coupling we have to produce shorter and more narrow SQUIDS or further increase the shielding at the cryostat, so any magnetic field noise produces smaller flux changes in the SQUIDS.

In Fig. 4.14 we later show and discuss in detail three cuts of this scan. They are indicated by vertical lines at the respective B-field with corresponding color in Fig. 4.13 a).

Figure 4.13 b) shows the fitted eigenfrequencies from Res 1 (blue) and Res 2 (red). This allows to apply the resonance frequency model as developed in Sec. 2.3, predicting the

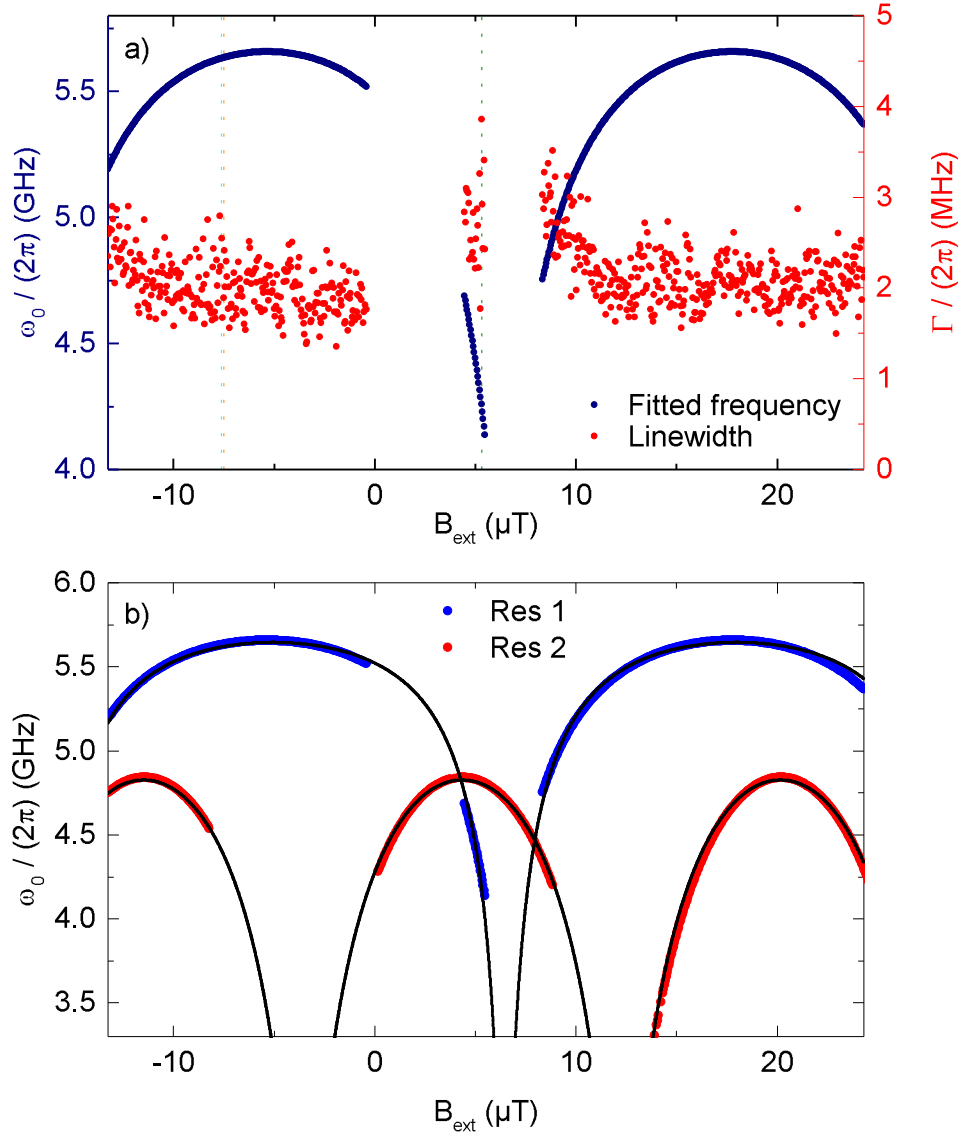


**Figure 4.13:** Detailed measurement of  $\omega_0(B)$  curve of Res 1 and 2. a) scan of Res 1 with low detection bandwidth and a narrow frequency span to analyze the broadening of the resonator caused by magnetic field noise. Resonator's eigenfrequency is shown in blue and the resonator's linewidth (FWHM) is depicted as red dots. The scanning window was set too close so some resonator points are missing, e.g. between 0 and  $5 \mu\text{T}$ . Slices from Fig. 4.14 are indicated by respective colors. b) Fit of flux dependent resonator eigenfrequency with the model from Sec. 2.3 and Eq. 4.13. The model of a non sinusoidal wave introduced in [36] (see Eq. 4.14) leads to similar fit curves being not separable in this representation.

resonator frequency as

$$\omega_0(\Phi) = \frac{\omega_R}{\sqrt{1 + 2\frac{L_J(\Phi)}{L_R}}}. \quad (4.13)$$

This model is plotted as black line in Fig. 4.13 b) with the fit parameters listed in Tab. 4.3. Since the resonance frequency, the impedance and the critical currents were characterized before we expected being able to predict the resonators tuning. Though the model differed from the experimental results, most obviously seen in an offset in the frequency. This indicates that the simple model introduced in Sec. 2.3 is incomplete. The resonator's frequency, hence inductance might be influenced by two more factors:

First the SQUIDs arms are relatively thin and long and thus produce a large inductance. Moreover, the SQUID is placed at the current anti-node so any inductance added at this position gives a large contribution to the total inductance. Second the SQUID might affect the boundary condition at the shunting location of the MW resonator and resulting in a non sinusoidal spatial amplitude distribution. The SQUID acts as a punctual impedance mismatch between the resonator and the grounding as calculated for a  $\lambda/2$  resonator in [36]. Bourassa *et al.* [36] take all this into account and predicts the following flux dependent microwave resonator frequency: Then one has to use discrete methods leading to the Bourassa model:

$$\omega_0(\Phi) = \frac{\omega_R}{1 + \frac{L_J(\Phi)}{L_R}}. \quad (4.14)$$

Both effects change the efficient resonance frequency, hence the resonators inductance  $L_R$ . The Josephson inductance is determined by the critical current in the SQUID. Since in Eqs. (4.13) and (4.14) only the ratio  $L_J/L_R$  is found, no insight in the parameters themselves can be made, only the ratio can be determined by experiment. As explained above we expect the effective resonator's inductance with SQUID to be different than without. So we have assumed the critical current to be  $0.5 \mu\text{A}$  as measured before for pure SQUIDs with similar design (see Sec. 4.2). Since we only saw small fluctuations in it (see table 4.1) this seems a good approximation. With this, the tunability can be predicted sufficiently with the lumped element model from Sec. 2.3, as seen in Fig. 4.13 b).

We have also applied the Bourassa model to our data and summarized the results from both models in table 4.3. From the fit parameter we find that the relative deviations from the designed resonance frequencies agree within 20% for both models. On the other side the deviations in fitted to designed frequency are not small enough to separate the single resonators, which is unsatisfying. For a proper physical understanding we therefore recommend to investigate this with more samples hence more data in the future, e.g. by having a look at the inductance from the mechanical beams, different inductances for the resonators as well as critical currents. So the models can be tested in detail.

Nevertheless, for deducing the electromechanical coupling only the slope of the reso-

nance curve is important. As both fit functions describe the data, despite of the actual obtained parameters, extremely well we can proceed from there on and calculate the electromechanical coupling.

in	$\omega_R/(2\pi)$ GHz	$\omega_{R,L}$ GHz	$\omega_{R,B}$ GHz	$L_{R,L}$ nH	$L_{R,B}$ nH	$\partial_B\omega_0$ GHz/ $\Phi_0$	$\partial_B\omega_{0,1}$ GHz/ $\Phi_0$	$\partial_B\omega_{0,B}$ GHz/ $\Phi_0$
Res 1	<b>7.40</b>	6.12	6.05	3.68	4.44	<b>59.5</b>	48.4	51.2
	<b>6.20</b>	7.32	6.41	0.50	1.00	<b>19.0</b>	11.5	13.1

**Table 4.3:** List of fit parameters used to reproduce the experimental  $\omega_0$  data. Designed and measured parameters are set as bold font. The first model (lumped element approach) is indexed with L, the model from Bourassa *et. al.* with a B. Except for the lower resonators frequency with the Bourassa approach no resonance frequency is sufficiently precise modeled. In contrast the slope which is required for the coupling strength is fitting with the experimental results for both models and resonators.

In Fig. 4.14 we show three cuts of a scan for Res 1. a) and b) are just one field point apart at the maximum frequency of Res 1, while c) was recorded at a steep point of the resonator's tuning.

The change of the linear  $S_{21}$  parameter is shown in a frequency range of about 20 MHz and a Lorentzian peak shape with some asymmetry is found. a) and b) have a different linewidth  $\Gamma$  but c) is even broader. The fits are shown in black.

From fitting the experimental data a linewidth of about 2 MHz is found at the maximum resonance frequency (see also Fig. 4.14 a) and b)). To stay in the resolved sideband regime the resonance frequency of the mechanical oscillator has to be higher than the linewidth of the MW resonators this allows beam lengths of up to 100  $\mu\text{m}$  as it was found out in Sec. 4.1. Having a closer look one finds the linewidth to fluctuate from Fig. 4.14 a) to b) with  $\Gamma_1/\Gamma_2 \approx 1.7$ . The fluctuations have been explained above.

In contrast c) shows an even broader peak but here we were on a steep point of the resonators tuning, proofing former presumptions from Fig. 4.13 a) that magnetic field fluctuations were not enough shielded anymore for such high slopes.

In conclusion, we were able to measure the evolution of the resonator frequency and its corresponding tuning and linewidth as function of the magnetic field. The resonators can be described with a Lorentz and complex background as calculated before in [21]. The linewidth is about 2 MHz, at its maximum frequency and increases for high slopes of the resonator frequency function due to magnetic field noise to a linewidth of 4 MHz. The frequency evolution with the applied magnetic field is well described by the model as developed in Sec. 2.3 or with a discretized wavelength approach developed in Ref. [36]. We applied both models and obtained a good prediction of the frequency function. The de-

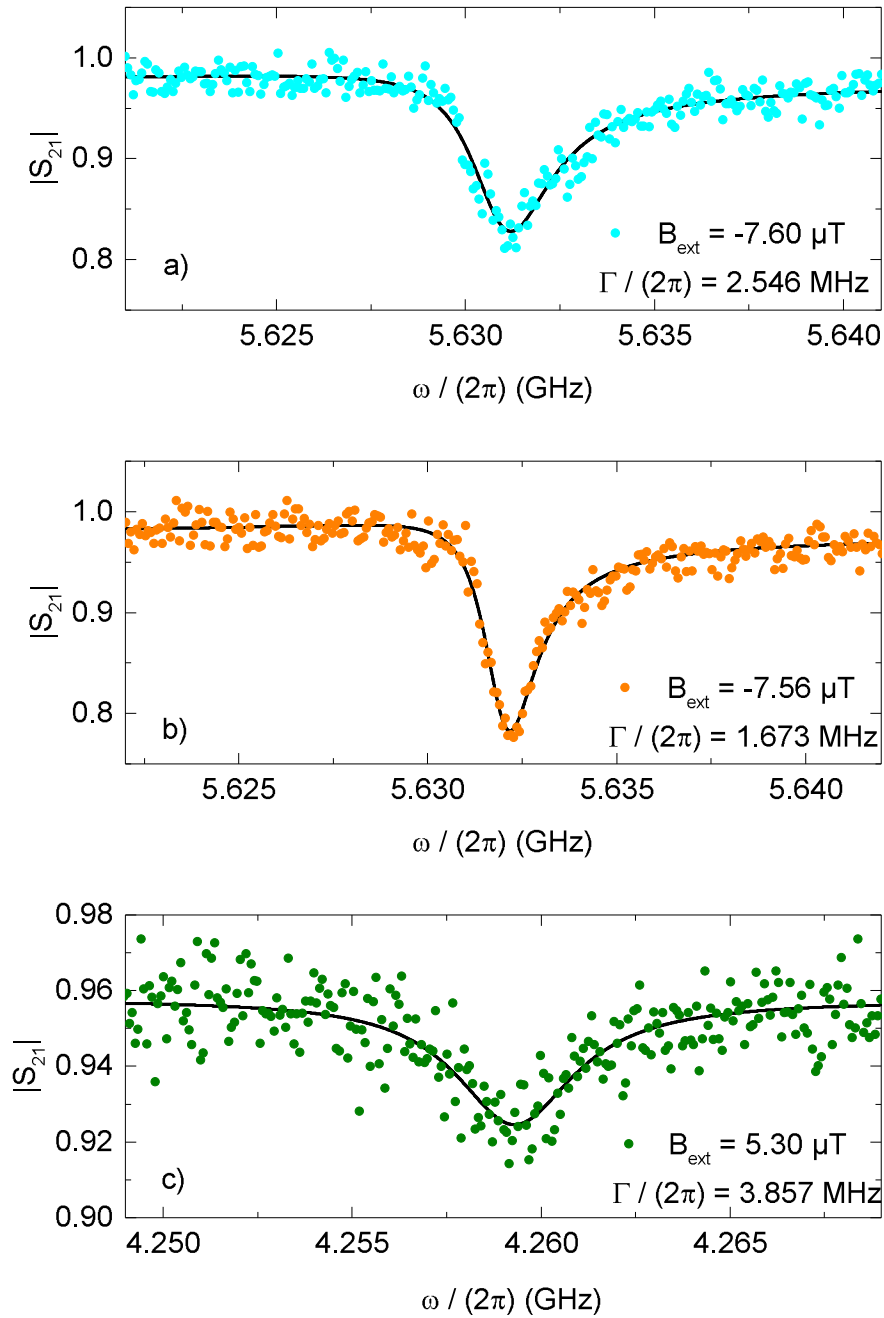


**Figure 4.14:** Linear transmission of Res 1 for selected magnetic field points as indicated by the dashed vertical lines in Fig. 4.13 a). Panel a) and b) are only 40 nT apart from each other and were taken at the maximum of the frequency curve (see Fig. 4.13 a)). The corresponding  $\Gamma_a/\Gamma_b$  from panel a) and b) is about 1.7. c) shows the transmission at a steep slope where  $\Gamma$  rises to higher values since there the resonator is more sensitive to field noise. Deviations in field then lower the signal depth by overlapping field points and so increase  $\Gamma$ .

termination of the maximum slope by experiment was confirmed by the theoretical models.

Up to here we have found a critical field and the maximum observable slopes of the resonators by 59.5 GHz and 19 GHz, which is what is required to estimate possible coupling strengths. The next sections show further experiments on flux tunable resonators which are not directly related to an optomechanical experiment but of interest to get a better understanding of such MW resonators and SQUID systems, i.e. which could be used to calibrate the photon number in the MW resonator.

### 4.4.3 Tunable nonlinearity

As shown in Sec. 2.3 a MW resonator combined with a SQUID is a tunable nonlinear resonator since the SQUID adds a nonlinear inductance  $L_J$ . So as in Sec. 4.1 we expect a Duffing behavior at higher drive powers tunable by the applied flux.

To investigate the non-linear behavior of the resonator, we measure the resonator's transmission spectrum as a function of drive power for several magnetic field points. In analogy to Sec. 4.1 we analyze the critical frequency  $\omega_{\text{eff}}$  and the corresponding dip amplitude  $A_{\text{crit}}$  since  $\alpha$  is proportional to  $A_{\text{crit}}^2/(\omega_{\text{eff}} - \omega_0)$ . Plotting the uncalibrated critical amplitude  $CA_{\text{crit}}$  yields the uncalibrated Duffing parameter  $\alpha' \propto \alpha$  for each field point. In the end we plotted  $\alpha'$  over the slope of the resonators detuning to compare them and conclude possible correlations.

Our results are summarized in Fig. 4.15. In a) and b) the transmission of the resonator at 5.65 and 5.50 GHz is shown for various drive powers. The typical Duffing shark fin behavior with a cut off frequency at  $\omega_{\text{eff}}$  is found. In contrast to our mechanical resonators here the effective resonance frequency shifts to lower frequencies for increasing drive power indicating a negative  $\alpha$ . In a mechanical picture this corresponds to a softening of the spring constant [29], here the higher drive currents increase the Josephson inductance. Further comparing a) and b) one finds a higher nonlinearity at 5.50 GHz, since it starts getting nonlinear at even lower drive powers best observed at  $-115$  dBm drive power (blue curve).

In c) we show the result of an analysis on such measurements at 5.00 GHz directly. Here the uncalibrated critical dip amplitude  $CA_{\text{crit}}^2$  over  $\omega_{\text{eff}}$  is plotted in a frequency range of about 10 MHz. The amplitudes show a linear dependence as expected. One finds the corresponding  $\alpha' = 9 \cdot 10^{-15}$  W/GHz.

The  $\alpha'$  are collected in d) over the frequency slope. Clearly the nonlinearity is tunable in a range of 2 orders of magnitude. Experimental limits explained next kept us from measuring at higher slopes, which would have drastically extended the range of tunability.

To sum up we were able to measure and analyze the nonlinearity of a MW resonator

and SQUID system, which was done analogue to the mechanical one before. In contrast the Duffing parameter is negative and tunable over 2 orders of magnitude.

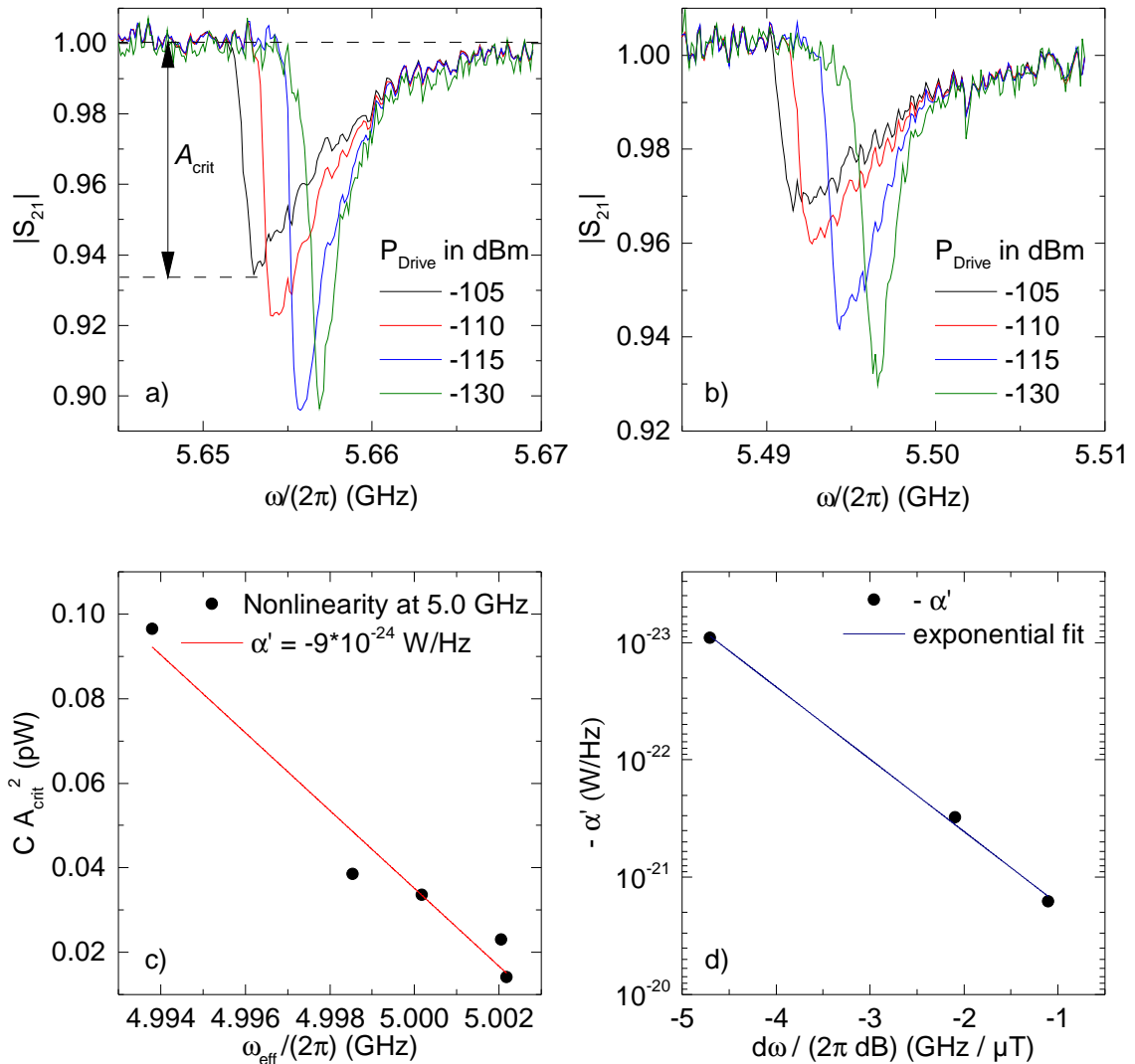


**Figure 4.15:** Resonator response for several drive powers at a) 5.65 GHz ( $B_{\text{ext}} = -5.30 \mu\text{T}$ ) and b) 5.50 GHz ( $0.0 \mu\text{T}$ ). With higher slope of the resonator branch the nonlinearity is increased. From this one can extract the dip size  $A_{\text{crit}}$  at the critical frequency  $\omega_{\text{eff}}$  as indicated in a). As for the mechanical resonators the Duffing parameter  $\alpha$  can be determined by plotting  $A_{\text{crit}}^2$  as a function of  $\omega_{\text{eff}}$ . We plotted this for the nonlinearity at 5.0 GHz ( $3.53 \mu\text{T}$ ) in c). In contrast to a mechanical resonator this microwave resonator has a negative, tunable nonlinearity. We summarized our results for  $\alpha'$  in d) showing a tunability over two orders in magnitude.

#### 4.4.4 Temperature dependence of the SQUID microwave resonator hybrids.

For microwave transmission experiments exceeding timescales of about 20 min. we notice fluctuations in the resonance frequency in the resonator for a magnetic field bias of  $4.42 \mu\text{T}$ . These frequency changes are correlated with temperature instabilities at the sample and mixing chamber from about 50 to 70 mK. Those jumps are most likely caused by a superfluid leak that heats the mixing chamber and cools the exchange coil [59]. Paramagnetic defects in materials that we use in the cryostat then can cause a change in the magnetic background field  $B_0$  and so move the  $\Phi/\Phi_0$  ratio. We found most correlation with the temperature sensor at the exchange coil (EC). In Fig. 4.16 we plotted power sweeps for one a) and six b) hours at a resonator frequency of 4.91 GHz. The change of 10 MHz corresponds here to a induction change of  $\Delta B = 27 \text{ nT}$  which we converted with our fit curve for Resonator 1. To overcome these temperature drifts we started carefully heating the still, enlarging the peak interval from 20 min to 20 hours. In the following

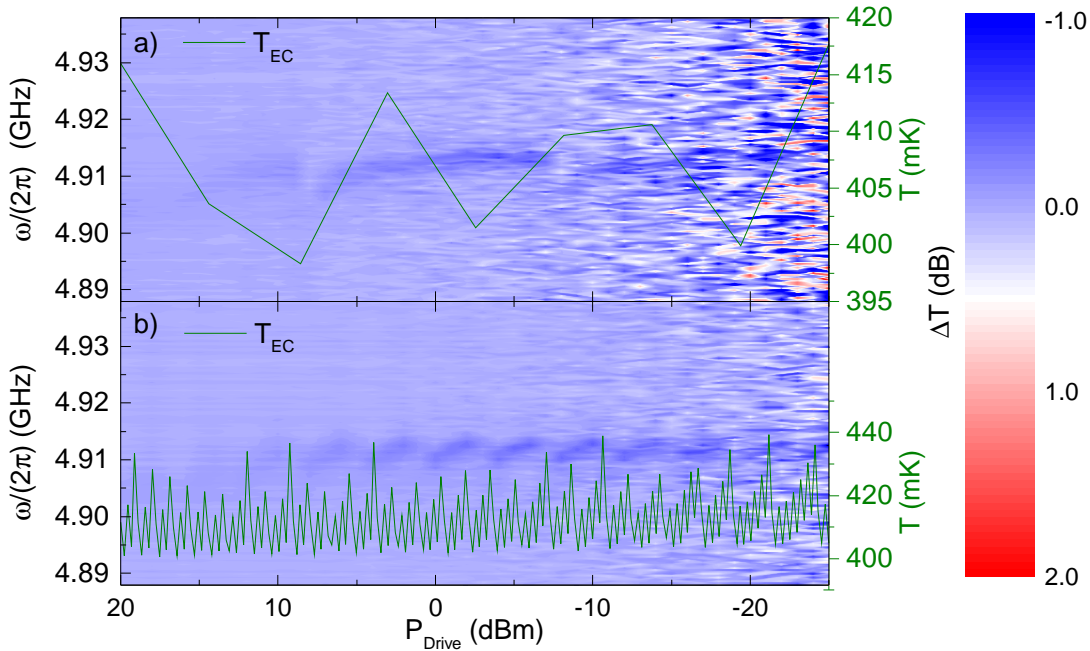


**Figure 4.16:** Resonator transmission over drive power for measurement times of a) 1 hour and b) 6 hours. In green the temperature of the exchange coil is plotted. A superfluid leak leads to the jumps in temperature which changes the temperature of paramagnetic impurities and so influences the resonators eigenfrequency.

we determine the effect of paramagnetic impurities (with  $J = 1/2$  and  $g_J = 2$ ) at low temperatures. Therefore the density of them  $n_e$  is calculated. To simplify we assume the impurities are exposed to the magnetic field at the SQUID hence also having the same

temperature as the sample, which was 50 and 70 mK. Parts that satisfy these assumptions could be the brass screw or the copper plate that fix the magnetic coil. The applied induction  $B_z$  consists in general of magnetic field  $H$  and magnetization  $M$  [60]:

$$B = \mu_0(H + M). \quad (4.15)$$

Assuming the magnetic field to be temperature stable, the induction change is only attributed to the magnetization  $\Delta B = \mu_0 \Delta M$ . The temperature dependence of the magnetization is described with the Brillouin function  $B_J(y)$  [60]

$$M = M_s B_J(y) = n_e \mu_B B_J(y) \quad (4.16)$$

with the temperature dependent Brillouin function:

$$B_J(y) = \frac{2J+1}{2J} \coth\left(\frac{2J+1}{2J}y\right) - \frac{1}{2J} \coth\left(\frac{y}{2J}\right) \stackrel{J=1/2}{=} \tanh(y) \quad (4.17)$$

and the temperature factor  $y = g_J \mu_B B / (2k_B)$  [60]. So we conclude:

$$\Delta B = \mu_0(M_{T=0.05} - M_{T=0.07}) = \mu_0 n_e \mu_B (\tanh(y_{T=0.05}) - \tanh(y_{T=0.07})) \quad (4.18)$$

Solving Eq. (4.18) for the impurity density leads to  $2.72 \cdot 10^{20}$  particles per  $\text{cm}^3$ , corresponding to a defect density of about one thousandth, seeming reasonable.

## 4.5 Swinging SQUIDs

Up to here we fabricated a flux tunable resonator consisting of a MW resonator and a SQUID. To complete the inductively tunable electromechanical hybrid system from here on we have to release one arm of the SQUID. Though the issue in this step is the thin oxide layer of about 2 nm between the two aluminum layers forming the Josephson junctions. Since it acts as an insulator any static charge coming from e.g. EBL or RIE might result in an electrostatic discharge across the junction and thus destroys it. As already observed with qubit structures [61]. For the release of the SQUID arm we need both processes: EBL and RIE.

In former studies we have already seen that we can apply an electron beam to the junctions, since we took images via an SEM and found the SQUIDs to be working still. This comes from the fact that the electrons in our design can spread over comparable large areas to the contact plates or the ground plane. In contrast in qubits there are island structures where the electrons from the beam are trapped between two Josephson junctions hence tend to destroy them. So we suspect that the EBL process is not at the origin of our broken SQUIDs leaving the influence of the RIE as only unknown parameter.

When bonding the sample to the carrier of the cryostat a proper grounding of the sample

and yourself is import. Otherwise it the junctions might break by electrostatic discharge. To gain inside and identify the process resulting in the destruction of the SQUIDs junctions we employed the following protocol:

- Fabricate 4 SQUIDs on  $\text{Si}_3\text{N}_4$  on contact pads for 4-point measurements.
- EBL patterning of the etching windows with PMMA MA 33% resist.
- Characterization measurement of the SQUIDs at the 500 mK cryostat.
- RIE with anisotropic and isotropic etching process as explained in Sec. 3.1.2.
- Measurement of released SQUIDs at the 500 mK cryostat.

As sample we used SiNSquid 11a for this test. We show an SEM image from one of the SQUIDs after applying this proceeding in Fig. 4.17 a). Here we see the SQUID from above as well as the etched area with the released beam in front. Aluminum parts are marked in green. The sample was contaminated in the cryostat since a dirt particle is found on the left side. Nevertheless, this particle should not impact the electrical sample performance as it is not in contact with any parts of the SQUID. In contrast to Fig. 3.9 where a design for practicing was chosen this design is the one installed in the MW resonators and indicates the challenge of fabricating a nanometer sized  $60\mu\text{m}$  long beam next to a similar one just  $2\mu\text{m}$  away and later write an etching window only covering one of them. In Fig. 4.17 c) a clamp of the nanobeam is depicted, where one can see sandwich structure from the two layers from the aluminum shadow evaporation (green) and the silicon nitride (blue) under both of them. The ridge from etching is found under the beam. Figure 4.17 d) shows one of the Josephson junctions (uncolored). At the first cool-down we found one working SQUID. Two other SQUID did not work properly but showed a I-V curve indicating Josephson tunneling. The hysteretic current-voltage curve of the SQUID is depicted in black in Fig. 4.17 b). After the RIE etching the SQUID was destroyed indicated by an ohmic behavior as depicted in the same figure in blue which is indicative for a shorted oxide layer present in the junction. Also the other two broken SQUIDs changed their appearance.

So as expected the EBL process did not destroy the SQUID, since we found a working one after the first cooldown. In contrast the RIE does have an influence on Josephson junctions. Most likely we expect the high voltages that are applied to accelerate the etching atoms (up to 380 V [42]). Especially we suspect the anisotropic etching process to be the reason as why here the highest voltages are applied to the structures. That means that the fabrication has to be changed and we propose either to apply the anisotropic etching first and evaporate the aluminum after or to use conductive resists that protect the junctions by preventing a too large voltage build up across the junction. Also shorting the SQUIDs and open the short in the end by etching or focused ion beam cutting could

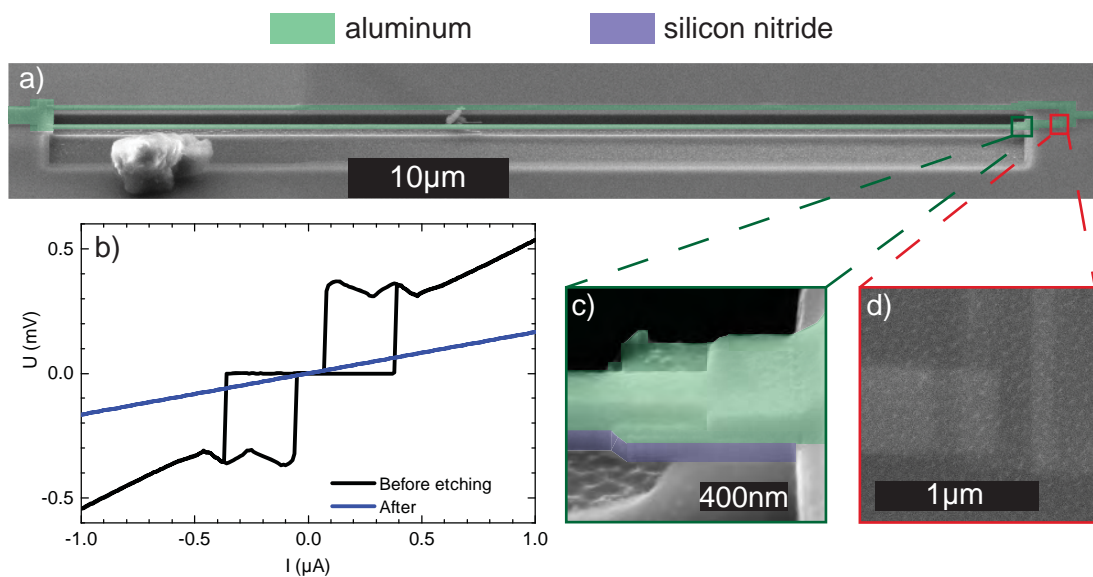


**Figure 4.17:** Influence of reactive ion etching on SQUIDs a) Color coded SEM image of the etched SQUID under an angle of  $60^\circ$ . The released arm is in front. b) SQUID 2 from sample SiNSquid11a: before etching the typical current voltage curve including a hysteresis was observed. After the etching at the RIE only an ohmic behavior was found indicating the SQUID to be ruined by this process. c) clamp of the nanomechanical beam. The two layers from shadow evaporation are visible as well as the silicon nitride layer underneath. d) top view at a Josephson junction without color coding.

be a possibility.

All in all, we identify this last etching process as a critical step in the process flow, which will require further testing and process development.

## 4.6 Coupling strengths in inductively tunable cavity optomechanics

Now we want to briefly summarize the experimental findings and conclusions of this chapter results. In this context, we estimate a possible coupling strength reached with our fabricated SQUID microwave resonator hybrid and compare it with capacitive coupling rates published in the field of cavity optomechanics. In the end we discuss further improvements on the sample design and propose a procedure reaching the strong coupling regime.

In this chapter, we were able to demonstrate that all the individual components required for the inductively coupled nano-electromechanical systems are indeed operational.

Moreover, by analyzing the flux tunability of the microwave resonator SQUID system, we estimated achievable electromechanical coupling rates of the MW resonators. We found highest slopes of  $\partial\omega_1/(\partial\Phi) = 2\pi \cdot 59.47 \text{ GHz}/\Phi_0$  and  $\partial\omega_2/(\partial\Phi) = 2\pi \cdot 18.95 \text{ GHz}/\Phi_0$  also confirmed by our fitted curves. Please note, that this coupling rates will be flux tuneable. This means that in principle even higher coupling rates should be possible by tuning the system to an even more steep region. Nevertheless, technically the coupling will be limited by magnetic flux noise.

The two resonator SQUID hybrids also contained long SQUID arms of a designed mechanical resonator length of  $l_1 = 40 \mu\text{m}$  and  $l_2 = 70 \mu\text{m}$ . From our nano-string experiments, we expect for these designs resonance frequencies of  $\Omega_1/(2\pi) = 5.4 \text{ MHz}$ ,  $\Omega_2/(2\pi) = 2.9 \text{ MHz}$ , respectively. The cooling of this beams down to mK temperatures will lead to an increase in the mechanical resonance frequencies by a factor of 1.3 due to the difference in the thermal expansion coefficients according to Eq. (2.7). Therefore, we expect zero-point fluctuations of  $x_{zpf,1} = 19 \text{ fm}$ ,  $x_{zpf,2} = 11 \text{ fm}$ .

The inductive electromechanical coupling does not only scale with the resonance frequency derivative (with respect to the magnetic flux bias) but also directly with the external bias field  $B_z$ , which will be limited by the critical field of the superconducting materials used for the devices. In particular the aluminium of the SQUID has a critical magnetic field of 2.2 mT as experimentally determined for our particular device geometries. We expect the magnetic field to influence the resonator even before the break down so for our assessment we will use 1 mT as critical magnetic field to estimate the electromechanical coupling strength.

Combining those results with Eq. (2.49) we predict a vacuum coupling strength of

$$\frac{g_{0,1}}{2\pi} = 13.1 \text{ kHz} \quad \text{and} \quad \frac{g_{0,2}}{2\pi} = 12.6 \text{ kHz} \quad (4.19)$$

In comparison to current results with doubly clamped beams in a superconducting CPW resonator by dielectric coupling 11 mHz were measured [28]. Here a  $\text{Si}_3\text{N}_4$  beam was coupled in between two resonators by influencing the dielectric field constant depending on the beam amplitude. The coupling appears low but on the other side since only  $\text{Si}_3\text{N}_4$  is used the linewidth of the mechanical resonator is very small being of interest for further applications.

Further a doubly clamped nanomechanical beam capacitively coupled to a CWP resonator by acting as a second capacitance showed 1.2 Hz [21]. Recently at the WMI the gap size for capacitive coupling between beam and ground plane was tried to decrease to 20 nm using advanced fabrication techniques like focused ion beam cutting (FIB). This could increase the coupling to 200 Hz [42].

On the other side J.D. Teufel *et. al.* reached coupling strengths of 201 Hz but here neither a double clamped beam nor a CPW resonator was used. Instead a 3 dimensional drum-like structure where one side of the drum was released to swing was coupling the

mechanical motion capacitively to a lumped element resonator. So our expected vacuum coupling strength exceeds the current reported values by a factor of roughly 65 for our first generation of samples.

In the following we like to show an approach how to further extend this coupling strength to the MHz regime. We start by the fact that the vacuum coupling strength can be written as a product of the applied magnetic field, the length of the nanobeam, the corresponding zero-point fluctuation and the change of the MW frequency to flux variations. So increasing the coupling strength is achieved by four parameters:

- **Length:** Here we have achieved  $70\ \mu\text{m}$  already. Increasing the beam length will increase the coupling but also decrease the mechanical resonator frequency. Since it has to be higher than the linewidth of the MW resonator to be in the resolved sideband regime it cannot be increased arbitrarily. As maximum we determined  $l_{\text{max}} \approx 100\ \mu\text{m}$  leaving us a total improvement factor of 1.4.
- **Zero-point fluctuation:** From experimental results we expect our beams to have up to 19 fm fluctuation. With optimized fabrication, e.g. using more narrow beams or decreased layer thicknesses, 30 fm were reached for a Nb-Si<sub>3</sub>N<sub>4</sub> system of  $60\ \mu\text{m}$  long beam in capacitive coupled samples [47]. So there is some potential though it has to be questioned whether the gain is worth the risk because the optimized thinner beams are more likely to break of course.
- **Magnetic field:** Here we found a maximum of 2.2 mT, to be sure avoiding negative effects on our MW resonators we estimated the coupling strength with 1 mT. The critical magnetic field parameters are material dependent so for future experiments one should have a closer look to determine the maximum capabilities without influencing the MW resonator.
- **Flux tunability:** As we showed up to  $60\ \text{GHz}/\Phi_0$  could be observed. Limitation here is given on the one side by the cold amplifiers in our setup. Otherwise we could follow the resonator curve to higher values. So shifting the frequency to higher values will allow to reach higher slopes. Moreover second or third harmonics can be studied. In particular shifting the frequency up to 12 GHz and looking at the second harmonic or leaving the frequency at 5 GHz taking the third harmonic will both result in a slope 100 times higher than observed so far.

We saw that our design parameters are already well optimized and except for the slope only minor improvements can be achieved. So we think of a sample with the same parameters we found for our first generation, except increasing the slope by 100. So we can reach we touch the strong coupling limit since then:

$$1.3\ \text{MHz} \approx \frac{g_0}{2\pi} \approx \frac{\Gamma}{2\pi} \approx 2.5\ \text{MHz} \quad (4.20)$$

Those slopes will on the other side be sensitive to noise from external magnetic fields. With our samples on the one hand we were able to observe inclines mentioned above on the other hand indications like the FWHM in figure 4.13 a) show that it already starts influencing the resonator. So the current field noise level is in total controllable for us. Assuming the same magnetic field noise  $\delta B$  as we have observed it, the flux sensitivity becomes  $\delta\Phi = l_{\text{SQUID}}b\delta B$  with  $l_{\text{SQUID}} > l$ . The coupling is proportional to  $l$ , but independent of  $b$  which can in principle be decreased arbitrary ending up in very narrow, long SQUIDs. Currently to achieve a decreased flux sensitivity of 100 the width has to be decreased from  $2\ \mu\text{m}$  to  $20\ \text{nm}$ .

Of course this is extremely challenging in fabrication. A beam with width of about  $200\ \text{nm}$ ,  $70\ \mu\text{m}$  long next to symmetric but fixed one that is only  $20\ \text{nm}$  apart. But previous work in our group has been done on such beams and found evidence it was working in capacitive coupled devices [42]. So we might have the capability to produce such systems combining both: inductive coupling with the fabrication from capacitive coupled samples namely the focused ion beam cutting. Such small gaps then reduce the flux noise sensitivity by a factor of 100 and allow higher slopes of the same factor leading to vacuum coupling strength in the MHz regime. Of course increasing the shielding can support these efforts to achieve a sufficiently small flux sensitivity.

# Chapter 5

## Summary and Outlook

The main priority in this project is the development on an inductively coupled electromechanical system consisting of a superconducting coplanar waveguide resonator and a doubly clamped nanomechanical beam where the coupling is mediated by a SQUID. This approach in cavity electromechanics warrants for a theoretical model which is developed and presented in this thesis. This model is capable to predict the coupling strengths. Moreover this thesis additionally approaches this project from an experimental side. This includes the development of a device fabrication process as well as the initial mechanical and microwave characterization of the device.

We were able to fabricate such a system up to the release of the nanomechanical beam and measure each constituent. From these pre-characterization we obtained all information necessary to estimate the vacuum coupling strength  $g_0/2\pi$  of up to 13.1 kHz for first generation devices. These here envisaged vacuum coupling strengths are extremely superior compared to currently established electromechanical coupling rates for microwave based devices of doubly clamped beams in a superconducting CPW resonator by dielectric coupling 11 mHz were measured [28], while capacitive coupling showed 1.2 Hz [21]. Using a focused ion beam to minimize the gap between the mechanical beam and the ground plane, this coupling could be extended to 200 Hz [42]. With a 3 dimensional structure coupling strengths of 201 Hz have already been reached [16].

We also estimate how far the SQUID based inductively electromechanical coupling can be pushed towards the strong coupling limit. We are confident that by altering the geometry vacuum coupling strength in the MHz regime can be realized which then are in the order of the eigenfrequency of the mechanical system and close to the strong coupling limit.

To characterize the individual components of the hybrid device we started with optical interferometry of the mechanical resonators of the samples. To this end an optical interferometer was developed and built. In contrast to existing fiber based interferometer the new interferometer has a larger working distance (several mm) between optics and sample and provides a live microscope image of the sample and the laser spot. This allows fast and safe measurements and is therefor ideal for sample pre-characterization.

With this device we were able to characterize the nanomechanical attributes, in particular the resonance frequency depending on the beam length  $\Omega_m(l)$ . From this we can calculate the expected zero-point fluctuation. Further this gave insight in the tensile stress of the aluminum layer we evaporated. The observed in plane motion of the beam had a linewidth  $\Gamma_m$  of 277 Hz at room temperature corresponding to a quality factor of 13000. With a similar design but gold instead of aluminum Seitner *et. al.* [46] achieved about 10000, thus our devices can be considered as state of the art. By an upgrade in the electronic spectroscopy tool, i.e. we replaced the employed vector network analyzer with a modern lock-in amplifier, we were able to investigate the bifurcation at high drive powers since the mechanical resonators become nonlinear at high drives. This might allow a calibration independent of the equipartition theorem. Calibration by thermal activation remains challenging.

Moreover, we demonstrate that superconducting quantum interference devices can be fabricated on silicon substrates covered with a silicon nitride layer which is a major requirement for obtaining high quality mechanics. In addition we could not see any significant changes in performance. With and without the SiN layer critical currents of  $1 \mu\text{A}$  per SQUID were reached.

Further superconducting CPW resonators were built and investigated spectroscopically. The designed resonance frequency was confirmed. It was shown that an additional silicon nitride pad at the SQUIDs position has no influence on the resonance frequency, possibly because it is placed at the voltage node.

In addition we fabricated two flux-tuneable MW resonators, consisting of a  $\lambda/4$  Nb superconducting CPW resonators which are shunted via Al SQUIDs on  $\text{Si}_3\text{N}_4$ . We measured the resonators frequency tuning over more than 2 GHz, limited only by the bandwidth of the cold amplifiers. We also tested the maximal applicable magnetic field to the device and found that fields of up to 1 mT are compatible with the operation of the device. This is important, since the vacuum coupling strength scales linear with this field. The linewidth of the resonators was about 2 MHz at milikelvin temperatures. It showed slight to increase at high slopes of the resonance frequency curve attributed to field noise from external magnetic fields. Those slopes reached up to  $2\pi \cdot 60 \text{ GHz}/\Phi_0$ . In analogy to the mechanical oscillators we also found nonlinear behavior with negative  $\alpha$  on our MW resonators that we could tune by two orders of magnitude. This nonlinearity can be used to calibrate the photon number in the cavity. For a proper comparison with theory it is necessary to collect more data including more SQUID designs like critical currents, or beam lengths and widths. But the qualitative behavior can be described sufficiently with the introduced models.

In the future the release of the nanomechanical beam in combination with Josephson junctions has to be solved. Possible solutions were discussed in this thesis.

Once the electromechanical system is operational, sideband noise recording can be per-

formed and so the mechanical oscillator calibrated. Moreover the coupling strength can be extracted. Since we expect a tunability of coupling it is of high interested to measure the coupling strength over a magnetic field sweep to prove this expectation.

Once the thermal activated motion is measured a drive tone can be applied. This leads to so called electromechanically induced absorption (EMIA) and -transmission (EMIT). Here a detuned drive tone is used for a phonon-photon interaction, changing the transmission of the MW resonator. Due to the higher coupling strength in inductively coupled samples we expect a deeper insight in the electromechanic features extending recent studies [47]. Moreover it was shown that also the group velocity can be influenced by a red detuned drive [21]. With a higher vacuum coupling strength the probe tone can be decreased hence the interference increased. So a first approach is to transfer these studies to inductively coupled electromechanics.

Since the coupling is switchable, a new field of interesting effect occurs, when modulating the coupling on a timescale of the mechanical beam. This is possible with the current experimental setup, so the beam can be parametrically driven, like a swing. Of course the revers effect, parametrically deceleration is feasible, arising a new possibility for cooling. Further for an application as quantum storage the switchability is very interesting. When coupling the beam with the resonator excitations can be transferred from the MW to the mechanical resonator. Switching the coupling off enables long phonon coherence times allowing efficient storage of information in the mechanical system.

Thus this new class of electromechanical devices are expected to give access to a variety of entirely new electromechanical issues due to the new functionality of a tunable electromechanical coupling.



# Appendix A

## Standard fabrication procedures

### A.1 Optical lithography

The resist used for both invers and direct process is the same: *AZ 5214 E*, the developer is *AZ 726 MIF*. When fabricating multiple samples rinsing the developer cup with isopropanol helps keeping the samples clean from resist particles. Stop developing by rinsing twice in H<sub>2</sub>O and removing the water by blowing nitrogen on the sample. As spin coater we used *x*, with pre-installed programs #1 with 4000 rpm and #2 with 2000 rpm.

#### Invers-process

- spin coating, prog. #2
- prebake, 70 s at 110°C
- exposure with structure, dose 3 mJ / cm<sup>2</sup>
- bake, 120 s at 130°C
- flood exposure without mask, dose 42 mJ / cm<sup>2</sup>
- develop 2 – 4 min. Check developing via microscope

#### Direct-process

- spin coating, prog. #1
- bake, 70 s at 110°C
- exposure with edge bead (Randwall) structure, dose 100 mJ / cm<sup>2</sup>
- develop 2 min
- exposure with structure, dose 36 mJ / cm<sup>2</sup>
- develop 70 s. Check developing via microscope

## A.2 Reactive ion etching

For a proper and controlled etching the chamber has to be pumped to  $2.7 \cdot 10^{-5}$  mbar first.

For the *anisotropic etching* the following parameters are set:

IC Power = 30 Watt, RF Power = 100 Watt,  $\text{SF}_6$  = 20 sccm and Ar = 10 sccm at a pressure of 15 mTorr. Etching times are mentioned in the fabrication section in the thesis. The measured reflected power should be between 0 and 1 Watt, the BIAS 290 – 300 V.

## A.3 Double layer spin coating

For our samples we used the same spin coater as for the optical resist. Recently a new spin coater was installed, used only for electronic resist. Though most steps are similar.

- cleaning: acetone  $\rightarrow$  acetone  $\rightarrow$  isopropanol, each 2 min at level 2 at the ultrasonic bath
- spin coating *PMMA 33%* at program #3
- clean backside of the chip from resist remains via acetone impregnated Q-tips
- bake, 10 min at 160°C
- spin coating *PMMA 950k* at program #4
- clean backside of the chip from resist remains via acetone impregnated Q-tips
- bake, 10 min at 160°C
- add gold nano-particles with a toothpick

# Appendix B

## Further experimental observations

In the thesis I linked to this appendix for a detailed images of Fig. 4.12 b) and c) since the print version might not have a sufficient resolution. Due to the high amount of data, I was not able to edit it though, so I offer to send the data per mail to interested readers. Please contact Philip.Schmidt'at'wmi.badw-muenchen.de for high resolution images.

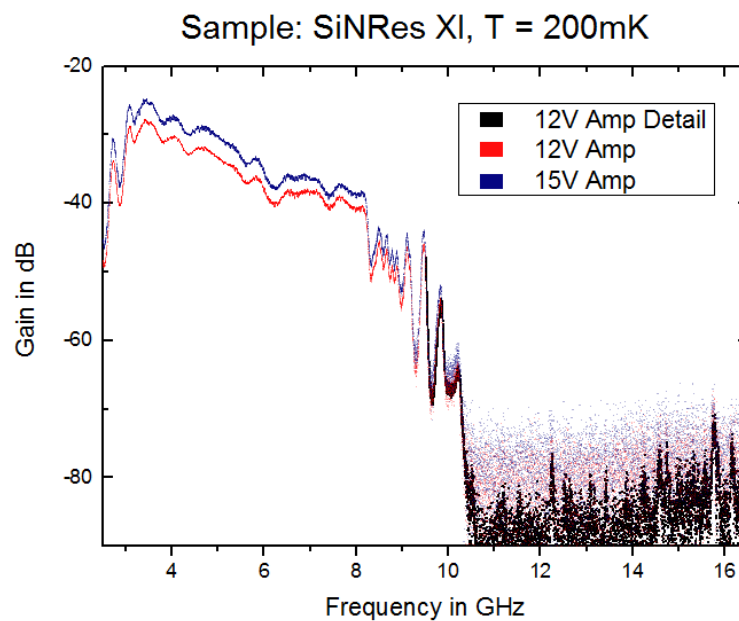


**Figure B.1:** Transmission of the Kermit cryostat at frequencies above the typical scope. At 8 GHz the cold amplifier stops proper working and breaks down at 10 GHz. At higher frequencies an other warm amplifier (red) and averaging (black) is necessary to observe any structure.

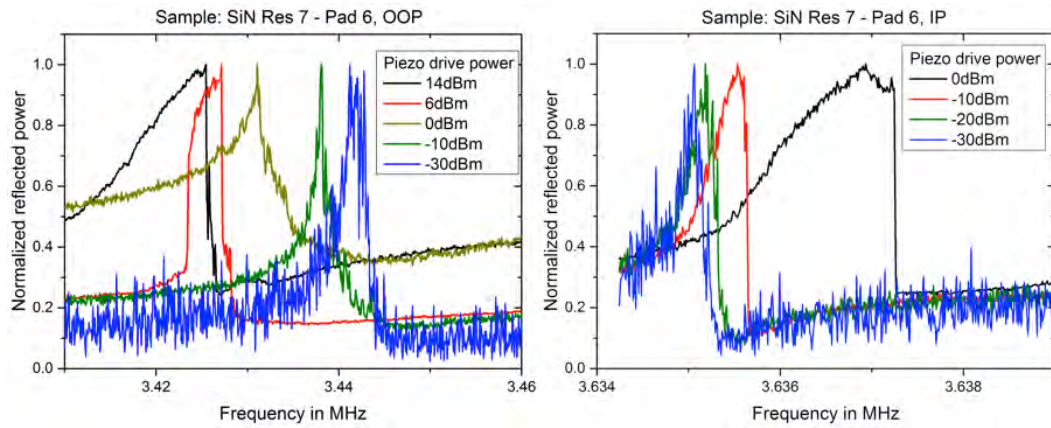


**Figure B.2:** Power reflectance of a selected  $60\ \mu\text{m}$  long mechanical resonator for out of plane (left) and in plane (right) motion. The power peak was normalized to 1. Shown are lower (blue) drive powers where best quality factors are observed. With higher powers (green) the peak broadens and the noise is reduced. At high drive powers in the Duffing regime it becomes non-linear and the typical shark fin peak is observed

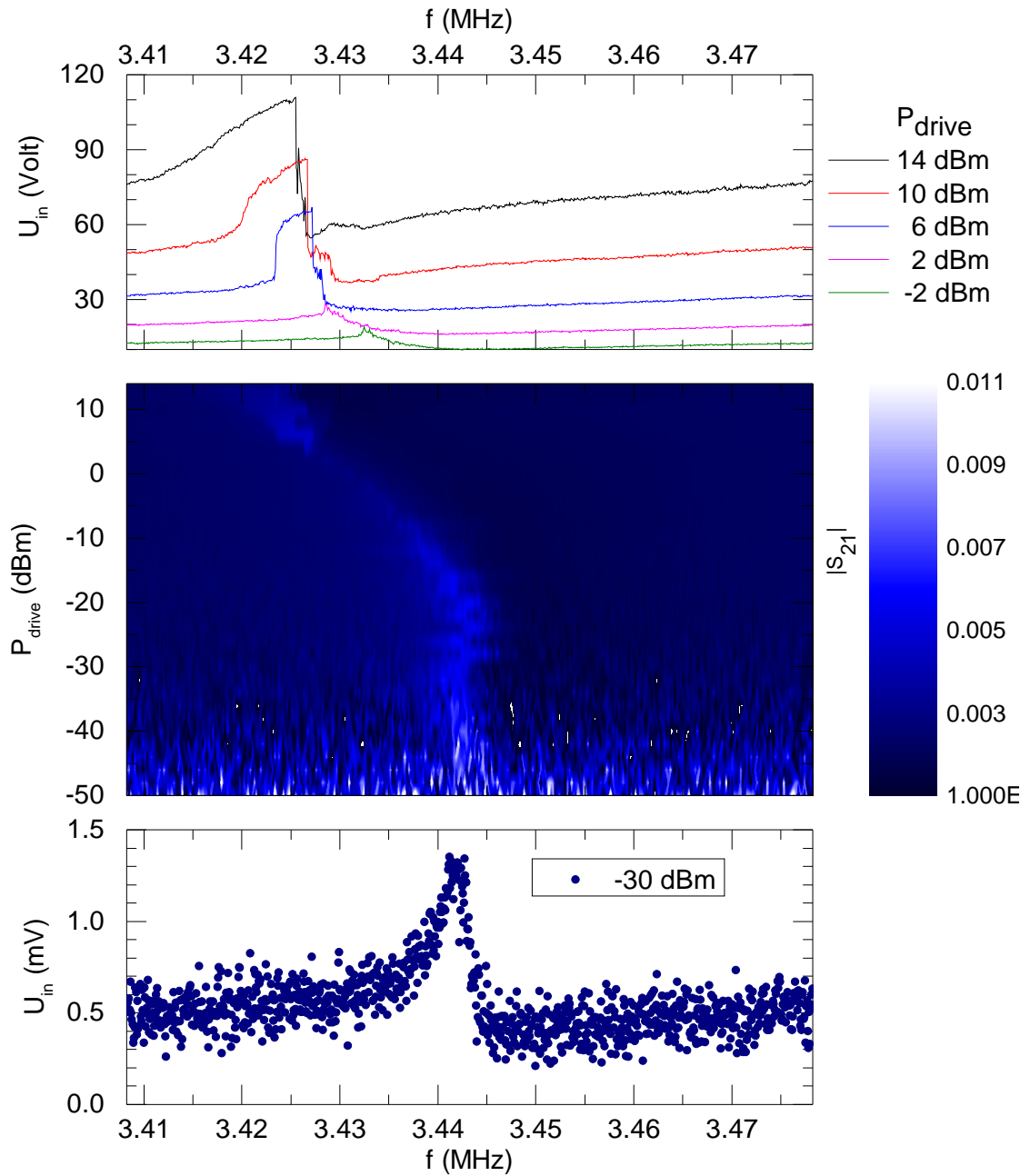


**Figure B.3:** Power reflectance of a  $60 \mu\text{m}$  mechanical resonator in out of plane direction



# Bibliography

- [1] M. Aspelmeyer, S. Gröblacher, K. Hammerer, and N. Kiesel, “Quantum optomechanics - throwing a glance”, [Journal of the Optical Society of America](#) **27**, A189 (2010).
- [2] G. E. Moore, “Cramming more components onto integrated circuits”, *Electronics* **38**, 114 (1965).
- [3] Intel, URL <http://www.intel.com/content/www/us/en/silicon-innovations/moores-law-technology.html>.
- [4] R. Landauer, “Irreversibility and Heat Generation in the Computing Process”, *IBM Journal of Research and Development* **5**, 183 (1961).
- [5] A. Berut, A. Arakelyan, A. Petrosyan, S. Ciliberto, R. Dillenschneider, and E. Lutz, “Experimental verification of Landauer’s principle linking information and thermodynamics”, *Nature* **483**, 187 (2012).
- [6] F. Marquardt, J. P. Chen, A. A. Clerk, and S. M. Girvin, “Quantum Theory of Cavity-Assisted Sideband Cooling of Mechanical Motion”, [Physical Review Letters](#) **99**, 093902 (2007).
- [7] V. B. Braginsky and F. Y. Khalili, *Quantum measurements* (Cambridge university press, Cambridge, 1995).
- [8] M. Aspelmeyer, T. J. Kippenberg, and F. Marquardt, eds., *Cavity optomechanics* (Springer, Berlin, 2014).
- [9] M. Aspelmeyer, T. J. Kippenberg, and F. Marquardt, “Cavity optomechanics”, [Reviews of Modern Physics](#) **86**, 1391 (2014).
- [10] J. Moser, J. Guttinger, A. Eichler, M. J. Esplandiu, D. E. Liu, M. I. Dykman, and A. Bachtold, “Ultrasensitive force detection with a nanotube mechanical resonator”, [Nature Nanotechnology](#) **8**, 493 (2013).
- [11] J. Chaste, A. Eichler, J. Moser, G. Ceballos, R. Rurali, and A. Bachtold, “A nanomechanical mass sensor with yoctogram resolution”, [Nature Nanotechnology](#) **7**, 301 (2012).

- 
- [12] K. Jensen, K. Kwanpyo, and A. Zettl, “An atomic-resolution nanomechanical mass sensor”, *Nature Nanotechnology* **3**, 533 (2008).
- [13] R. Kaltenbaek, G. Hechenblaikner, N. Kiesel, O. Romero-Isart, K. Schwab, U. Johann, and M. Aspelmeyer, “Macroscopic quantum resonators (MAQRO)”, *Experimental Astronomy* **34**, 123 (2012).
- [14] A. K. Naik, M. S. Hanay, W. K. Hiebert, and M. L. Feng, X. L. and Roukes, “Towards single-molecule nanomechanical mass spectrometry”, *Nature Nanotechnology* **4**, 445 (2009).
- [15] A. D. O’Connell, M. Hofheinz, M. and Ansmann, R. C. Bialczak, M. Lenander, E. Lucero, M. Neeley, D. Sank, H. Wang, M. Weides, J. Wenner, J. M. Martinis, and A. N. Cleland, “Quantum ground state and single-phonon control of a mechanical resonator”, *Nature* **464**, 697 (2010).
- [16] J. D. Teufel, T. Donner, D. Li, J. W. Harlow, M. S. Allman, K. Cicak, A. J. Sirois, J. D. Whittaker, K. W. Lehnert, and R. W. Simmonds, “Sideband cooling of micromechanical motion to the quantum ground state”, *Nature* **475**, 359363 (2011).
- [17] E. Verhagen, S. Deleglise, S. Weis, A. Schliesser, and T. J. Kippenberg, “Quantum-coherent coupling of a mechanical oscillator to an optical cavity mode”, *Nature* **482**, 63 (2012).
- [18] J. Kelly, R. Barends, A. G. Fowler, A. Megrant, E. Jeffrey, T. C. White, D. Sank, B. Mutus, J. Y. Campbell, Y. Chen, Z. Chen, B. Chiaro, A. Dunsworth, I.-C. Hoi, C. Neill, P. J. J. O’Malley, C. Quintana, P. Roushan, A. Vainsencher, J. Wenner, A. N. Cleland, and J. M. Martinis, “State preservation by repetitive error detection in a superconducting quantum circuit”, *Nature* **519**, 66 (2015).
- [19] A. D. Corcoles, E. Magesan, S. J. Srinivasan, A. W. Cross, M. Steffen, J. M. Gambetta, and J. M. Chow, “Demonstration of a quantum error detection code using a square lattice of four superconducting qubits”, *Nature Communications* **6** (2015).
- [20] C. A. Regal, J. D. Teufel, and K. W. Lehnert, “Measuring nanomechanical motion with a microwave cavity interferometer”, *Nature Physics* **4**, 555 (2008).
- [21] X. Zhou, F. Hocke, A. Schliesser, A. Marx, H. Huebl, R. Gross, and T. J. Kippenberg, “Slowing, advancing and switching of microwave signals using circuit nanoelectromechanics”, *Nature Physics* **9**, 179 (2013).
- [22] W. Weaver, S. P. Timoshenko, and D. H. Young, *Vibration Problems in Engineering* (John Wiley & Sons, Hoboken, NJ, 1990).
- [23] A. N. Cleland, *Foundations of Nanomechanics* (Springer, Berlin, 2002).

- [24] S. S. Verbridge, J. M. Parpia, R. B. Reichenbach, L. M. Bellan, and H. G. Craighead, “High quality factor resonance at room temperature with nano strings under high tensile stress”, [Journal of Applied Physics](#) **99**, 124304 (2006).
- [25] R. Hollaender, “Magnetostriction in nanomechanical beams”, Master’s thesis, Technische Universität München, Walther-Meißner Institut, Garching (2014).
- [26] F. Hocke, M. Pernpeintner, X. Zhou, A. Schliesser, T. J. Kippenberg, H. Huebl, and R. Gross, “Determination of effective mechanical properties of a double-layer beam by means of a nano-electromechanical transducer”, [Applied Physics Letters](#) **105**, 133102 (2014).
- [27] R. Gross and A. Marx, *Festkörperphysik* (Oldenbourg Wissenschaftsverlag, München, 2012).
- [28] M. Pernpeintner, T. Faust, F. Hocke, J. P. Kotthaus, E. M. Weig, H. Huebl, and R. Gross, “Circuit electromechanics with a non-metallized nanobeam”, [Applied Physics Letters](#) **105**, 123106 (2014).
- [29] A. Nayfeh and D. T. Mook, *Nonlinear Oscillations* (Wiley-VCH, Weinheim, 1995).
- [30] Q. P. Unterreithmeier, S. Manus, and J. P. Kotthaus, “Coherent detection of nonlinear nanomechanical motion using a stroboscopic downconversion technique”, [Applied Physics Letters](#) **94**, 263104 (2009).
- [31] A. Megrant, C. Neill, R. Barends, B. Chiaro, Y. Chen, L. Feigl, J. Kelly, E. Lucero, P. Mariani, M. O’Malley, D. Sank, A. Vainsencher, J. Wenner, and A. Cleland, “Planar superconducting resonators with internal quality factors above one million”, [Applied Physics Letters](#) **100**, 113510 (2012).
- [32] P. Schmidt, “Widerstand zwecklos”, *Junge Wissenschaft* **84**, 38 (2009).
- [33] R. Gross, “Applied superconductivity”, lecture notes, Walter Meißner Institut, Garching, (2013).
- [34] J. Clarke and A. I. Braginski, eds., *The SQUID Handbook* (Wiley-VCH, Weinheim, 2006).
- [35] U. Schaumburger, “Ketten von Resonatoren mit einstellbarer Nichtlinearität”, Master’s thesis, Technische Universität München, Walther-Meißner Institut, Garching (2014).
- [36] J. Bourassa, F. Beaudoin, J. M. Gambetta, and A. Blais, “Josephson-junction-embedded transmission-line resonators: From Kerr medium to in-line transmon”, [Physical Review A](#) **86**, 013814 (2012).

- [37] K. F. Wulschner, M. Pernpeintner, H. Huebl, and R. Gross, proposal: "Inductive coupling between a microwave resonator and a mechanical nanobeam oscillator", unpublished (2014).
- [38] K. F. Wulschner, "*Nb/AlO<sub>x</sub>/Nb* Josephson-Kontakte für supraleitende Quantenschaltkreise", Master's thesis, Technische Universität München, Walther-Meißner Institut, Garching (2011).
- [39] F. Hocke, X. Zhou, A. Schliesser, T. J. Kippenberg, H. Huebl, and R. Gross, "Electromechanically induced absorption in a circuit nano-electromechanical system", *New Journal of Physics* **14**, 123037 (2012).
- [40] F. Sterr, "Optimization of Josephson Junction Nanofabrication for Superconducting Quantum Circuits", Master's thesis, Technische Universität München, Walther-Meißner Institut, Garching (2013).
- [41] E. Xie, "Optimized fabrication process for nanoscale Josephson junctions used in superconducting quantum circuits", Master's thesis, Technische Universität München, Walther-Meißner Institut, Garching (2013).
- [42] A. T. Bohn, "Fabricating a cavity electromechanical system", Master's thesis, Technische Universität München, Walther-Meißner Institut, Garching (2014).
- [43] L. Rosenzweig, "Optische Interferometrie spinmechanischer Nanostrukturen", Master's thesis, Technische Universität München, Walther-Meißner Institut, Garching (2015).
- [44] M. Sebastian, "Loss reduction of superconducting coplanar microwave resonators on sapphire substrates", Master's thesis, Technische Universität München, Walther-Meißner Institut, Garching (2014).
- [45] R. Gross, "Low temperature physics 2", lecture notes, Walther Meißner Institut, Garching, (2013).
- [46] M. J. Seitner, K. Gajo, and E. M. Weig, "Damping of metallized bilayer nanomechanical resonators at room temperature", *Applied Physics Letters* **105**, 213101 (2014).
- [47] F. Hocke, "Microwave circuit-electromechanics in a nanomechanical hybrid system", Ph.D. thesis, Technische Universität München, Walther-Meißner Institut, Garching (2013).
- [48] "Material: Silicon Nitride (Si<sub>3</sub>N<sub>4</sub>)", (2015), URL <https://www.memsnet.org/material/siliconnitridesi3n4/>.

- [49] M. Winter, “Aluminium: the essentials”, (2015), URL <http://www.webelements.com/aluminium/>.
- [50] Q. P. Unterreithmeier, T. Faust, and J. P. Kotthaus, “Damping of Nanomechanical Resonators”, *Physical Review Letters* **105**, 027205 (2010).
- [51] P. Becker, P. Scyfried, and H. Siegert, “The lattice parameter of highly pure silicon single crystals”, *Zeitschrift für Physik B* **48**, 17 (1982).
- [52] “Silicon Nitride, Si<sub>3</sub>N<sub>4</sub> Ceramic Properties”, (2015), URL <http://accuratus.com/silinit.html>.
- [53] D. Lide, *CRC Handbook of Chemistry and Physics, 84th Edition* (CRC Press, Boca Raton, FL, 2003).
- [54] V. Ambegaokar and A. Baratoff, “Tunneling Between Superconductors”, *Physical Review Letters* **11**, 104 (1963).
- [55] T. Yamamoto, quality factors in reflection-type resonators, NEC Nano Electronics Research Laboratories, Tsukuba (2009).
- [56] M. Göppl, A. Fragner, M. Baur, R. Bianchetti, S. Filipp, J. M. Fink, P. J. Leek, G. Puebla, L. Steffen, and A. Wallraff, “Coplanar waveguide resonators for circuit quantum electrodynamics”, *Journal of Applied Physics* **104**, 113904 (2008).
- [57] V. Semiconductors, Tech. Rep., Virginia Semiconductors, <http://www.virginiasemi.com/pdf/generalpropertiesSi62002.pdf> (2002).
- [58] D. M. Pozar, *Microwave engineering* (John Wiley & Sons, NJ, Hoboken, NJ, 2011).
- [59] K. Neumeier, private communications, (2014).
- [60] H. Huebl, “Magnetism”, lecture notes, Walter Meißner Institut, Garching, (2015).
- [61] M. Haeberlein, private communications, (2014).



# Appendix C

## Acknowledgment

Financial and mental support by family Ernst u. Luise Schmidt was gratefully acknowledged. Thanks for everything. Further I would like to thank all the people who contributed to this project and supported me during my thesis:

- Prof. R. Gross for giving me the opportunity to write my thesis at the Walther-Meißner-Institut and his support in the SQUID designs based on his excellent knowledge.
- Hans Hübl for being the continuous, passionate drive shaping this thesis. It has been a real pleasure to work in such a productive and open minded atmosphere. I am very positive about future studies.
- Matthias Pernpeintner, who has shown me that there is always the most elegant way, and it is worth going it. This is a discovery I will use in the future for sure. Thanks for supervising me through this thesis!
- Friedrich Wulschner, whose constant and huge support has never been a self-evidence for me. Thanks for simply all your support, this has really pushed me forwards.
- Max Häberlein, Jan Götz and Edwar Xie supporting this project with their large experience in fabricating Josephson junctions as well as Lujun Wang optimizing the ghost patterning process.
- Anh Tu Bohn for is great work on etching parameters of nanomechanical beams, which has definitely accelerated this project.
- Daniel Schwienbacher, who has quickly fit into nanomechanics driving new ideas. I hope you have a great time with it.
- Helmut Thies in representation of the work shop for supporting this project by precision engineering. Without this support we would not have been able to build the new interferometer in such a short time.
- Thomas Brenning and Sebastian Kammerer for maintaining the experimental and fabrication facilities at the WMI.

- Akashdeep Kamra for enlightening discussions on the coupling between theory and experiments.
- Kai Müller and Franz Kramer for accompanying me on the study trips to Großglockner and Berlin.
- The qubit and magnetism groups at the WMI for all these great impression. It has been a big joy to be part of this.
- Prof. W. Heickl and D. Einzel for the consultations concerning non physical questions.
- Simply everyone else at the WMI, who keep this such a warm, open and productive atmosphere.

Thanks a lot guys!